Politecnico di Torino 1859

ScuDo
Scuola di Dottorato ~ Doctoral School
WHAT YOU ARE, TAKES YOU FAR

Doctoral Dissertation
Doctoral Program in Metrology (35th cycle)

A Small-Radius Rotating-Coil Measurement System for Field Characterization of Small-Bore-Diameter Magnets

By

Anna Lauria

******

Supervisor(s):
Prof. Marco Parvis, Supervisor
Prof. Pasquale Arpaia, Co-Supervisor
Dr. Marco Buzio, Co-Supervisor

Doctoral Examination Committee:
Prof.ssa Anna Maria Lucia Lanzolla, Referee, Polytechnic University of Bari
Dr. Carlo Petrone, Referee, CERN
Prof. Simone Corbellini, Polytechnic University of Turin
Prof.ssa Loredana Cristaldi, Polytechnic University of Milan
Prof. Egidio De Benedetto, University of Naples Federico II

Politecnico di Torino
2023

Declaration

I hereby declare that, the contents and organization of this dissertation constitute my own original work and does not compromise in any way the rights of third parties, including those relating to the security of personal data.

Anna Lauria
2023

* This dissertation is presented in partial fulfillment of the requirements for **Ph.D. degree** in the Graduate School of Politecnico di Torino (ScuDo).

To everyone who gifted me with their expertise, time, love and support.

Acknowledgements

I would like to thank my supervisors, Professor Pasquale Arpaia and Professor Marco Parvis w,ho enriched my research activities with precious ideas and suggestions in the metrology field, being always available to support me during the whole process.

I could not have undertaken this journey without the support of my supervisor, Dr. Marco Buzio, who guided my activities, with his immense knowledge of the field, and encouraged me during all the phases of my academic research.

Additionally, the success of my activities would not have been possible without Dr. Lucia Sabbatini e Dr. Alessandro Vannozzi, from INFN-LFN of Frascati, in Italy. Their advice, continuous cultural exchange, and belief in me have kept my spirits and motivation high during this journey. I also thank my defense committee, who generously provided knowledge and expertise.

Special thanks to everyone from the Test and Measurement section at CERN in Geneva, who gave me precociously advice and immeasurable technical support, not only to make it possible to realize my project but also to grow both professionally and personally.

I want to acknowledge everyone I met during the last years and everyone who has always supported me and never made me feel the weight of the distance.

Words cannot express my gratitude to my parents and my lovely family, for always being by my side, even from miles away, and Stefano for supporting my decisions and showing me how far love can travel.

Finally, I would like to share a message, from my experience luggage, with anyone who could read these lines. Over the last few years, I have learned that life challenges us every day, and doubting being in the right place is absolutely normal. Following a dream is challenging, and success is emotionally and physically taxing, especially if it requires leaving everything you love for something unknown. Now I know it's always possible to find inside us the strength and the motivation to go beyond our limits and become every day the better version of ourselves. So, in conclusion, we should keep in mind to stay positive, try our best, recognize our value, and always thank ourselves for never giving up.

Abstract

This thesis introduces a novel version of a rotating-coil measurement system based on PCB technology, specifically designed for the field characterization of small-bore diamater (less than 30 mm) quadrupole magnets. The proposed magnetic measurement system development was carried out in the context of the EuPRAXIA [1] project, which aims to produce high-energy electron beams using a compact plasma-based particle accelerator. Quadrupole magnets play a crucial role in any accelerator complex, and small-bore quadrupole magnets are particularly important in plasma-based accelerators, where high acceleration gradients must be achieved over short acceleration lengths. Accurate magnetic measurements are essential to limit orbit distortions and resonances in the particle beam and ensure that quadrupole magnets meet the required specifications for controlling beam trajectory and generating homogeneous magnetic fields.

The proposed measurement system is designed to address the challenges posed by the accurate characterization of EuPRAXIA quadrupole magnets, particularly with regard to geometric constraints, such as a bore diameter up to 30 mm. The design proposal aims to simplify the design as much as possible by using low-cost, off-the-shelf components, including the shaft housing the PCB magnetometer, and open-source software packages, thereby increasing the accessibility of this technology.

The thesis presents a detailed description of the proposed small-radius rotating-coil measurement system, characterized by an external diameter of 26 mm, including the layout, fabrication, and calibration of the PCB-based magnetic field sensor, as well as the shaft motion unit, acquisition chain, harmonic analysis, and post-processing software structure. Notably, the presented rotating coil system relies on a novel mechanical asset, based on a commercial carbon fiber tube, in which the PCB magnetometer is directly inserted.

The thesis also presents the numerical validation and metrological characterization of the system, including sensitivity and stability assessments. Experimental measurement results demonstrate the feasibility and effectiveness of the proposed PCB-based rotating coil system in achieving the target accuracy in the field characterization of permanent and resistive quadrupoles with a bore diameter of 45 mm. The proposed system can achieve the absolute accuracy of the main integrated gradient of 50 ppm, with a repeatability of 10 ppm, while the accuracy of high-order compensated harmonics is 100 ppm with a repeatability of 10 ppm. This performance meets the requirements for the measurement of the EuPRAXIA magnets.

Overall, this thesis contributes to the development of advanced measurement techniques based on rotating coil systems for particle accelerator magnets, providing a valuable tool for designing, testing, and optimizing quadrupole magnets for various scientific and engineering applications.

Contents

List of Figures

List of Tables

Nomenclature

Acronyms

ADC	Analog to Digital Converter
BNL	Brookhaven National Laboratory
CERN	Conseil européen pour la recherche nucléaire
COSY	Cooler Synchrtron
DSP	Digital Signal Processing
ENOB	Effective Number of Bits
ERL	Energy Recovery Linac
EuPRAXIA	European Plasma Research Accelerator with eXcellence In Applications
FACET	Facility for Advanced Accelerator Experimental Tests
FCC	Future Circular Collider
ILC	International Linear Collider
JLab	Jefferson Lab Accelerator
LCLS	Linac Coherent Light Source
LHC	Large Hadron Collider
LWFA	Laser-driven Plasma WakeField Acceleration
PAL	Pohang Accelerator Laboratory

PCB	Printed Circuit Board
PGA	Programmable Gain Amplifier
PMQs	Permanent-Magnet Quadrupoles
PWFA	Particle-driven Plasma Wakefield Acceleration
RF	Radio Frequency
RHIC	Relativistic Heavy Ion Collider
SAR	Successive Approximation Register
SLAC	Stanford Linear Accelerator Center
SPARC_LAB	Sources for Plasma Accelerators and Radiation Compton with Laser And Beam
SPS	Super Proton Synchrotron
SQNR	Signal to Quantization Noise
SSW	Single-Streched Wire
TTL	Transistor-Transistor Logic
XFEL	European X-Ray Free-Electron Laser Facility

Introduction

For more than half a century, particle accelerators played a fundamental role in different research fields, such as high-energy physics, radiotherapy for cancer treatments, production of short-lived medical isotopes, synchrotron light sources, free-electron lasers, beam lithography for microcircuits.

Currently, tens of thousands of particle accelerators are in use worldwide. However, the widespread use of accelerators is limited by cost and size constraints, especially in environments such as hospitals and universities. In order to overcome these limitations, the development of more compact and cost-efficient accelerator technologies is under investigation.

Over the past two decades, plasma-based accelerators emerged as one of the most promising candidates. The EuPRAXIA project is an example of a research project aiming to develop the next-generation plasma-based accelerator for a wide range of scientific applications [2]. One of the advantages of plasma-based accelerators is the possibility to achieve much higher acceleration gradients than RF-based accelerators, leading to much shorter acceleration distances and potentially smaller accelerator facilities. In fact, plasma waves can sustain much higher electric fields than the RF fields used in traditional accelerators [3].

The proposed accelerator design utilizes high-powered lasers to ionize a gas, resulting in the creation of a plasma capable of energizing charged particles to high levels. To achieve this objective, the use of magnetic components, such as solenoids or quadrupoles, is crucial for shaping and directing the plasma and regulating its properties. In particular, quadrupole magnets are essential magnetic elements for beam focusing and, in combination with plasma lenses, for precise control over the beam trajectory [4, 5]. In addition, the introduction of small-bore quadrupole magnets within plasma accelerators beamline enables the attainment of high acceleration gradients over short acceleration lengths, which are essential for the creation of

compact plasma accelerators.
In order to generate homogeneous magnetic fields, limiting orbit distortions and resonances in the particle beam, the production of high-precision beam-optics devices requires extremely tight tolerances. In this regard, precise magnetic measurements play a critical role by providing essential information for the installation and operation of magnets. Magnetic field characterization includes determining the field direction, field strength, field harmonic content, and magnet transfer function [6–8]. Accurate magnetic measurements enable the identification of the need for corrector magnets to control higher-order beam behavior [9]. Furthermore, these measurements facilitate the assessment of compliance with construction requirements during magnet production and the early detection of manufacturing errors. This early detection allows for easier rectification of any potential issues and ensures adherence to construction specifications.

In this Thesis, a new small-radius rotating-coil measurement system for filed characterization of small-bore diameter quadrupole magnets is presented.

In the Background part, **Chapter 1** introduces the history and overview of particle accelerators and covers the fundamentals of RF-based and plasma-based accelerators. **Chapter 2** focuses on EuPRAXIA project objectives and describes the EuPRAXIA@SPARC_LAB concept and the high-gradient quadrupoles developed for the foreseen accelerator facility. **Chapter 3** is dedicated to the introduction of different magnetic measurement techniques for accelerator magnets, such as NMR probes, Hall probes, wire measurement systems, fixed coil magnetometers, and rotating-coil magnetometers. The section ends with a discussion of the research context and motivations for the proposed rotating coil system.

In the Proposal part, **Chapter 4** focuses on the harmonic coil method, covering the mathematical basis and describing how induction coil magnetometers are used to implement it. **Chapter 5** describes the design of the proposed rotating coil system, including the design of the PCB-based magnetometer and the rotating coil transducer. **Chapter 6** details the design of the rotating coil test bench for small bore quadrupole magnets characterization, including the data acquisition system, the rotating-coil motion system, and the software for signal acquisition and harmonic analysis.

In the Experimental Results part, **Chapter 7** focuses on the metrological analysis of the system, including the calibration of the coil surface and rotation radius, as well as an analysis of acquisition chain performances and electro-mechanical characterization of the system. Finally, **Chapter 8** focuses on the experimental results obtained with the designed and implemented PCB-based rotating coil system, demonstrating the effectiveness and accuracy in magnetic field characterization.

Part I

Background

Chapter 1

Introduction to particle accelerators

The chapter provides an overview of the history, development, and current state of RF-based and plasma-based particle accelerators. The different types of accelerators and the principles behind their operation are introduced, as well as their ongoing advancements and future applications.

1.1 History and overview

One of the earliest pioneers in the field of particle accelerators was Ernest Lawrence [10], who developed in the late 1920s the first cyclotron as a tool for physics research and isotope production. In its simplest form, the cyclotron structure includes two conducting electrodes, typically in the shape of D-shaped half-cylinders, placed perpendicular to the magnetic field, between the poles of a DC magnet. The electrodes were separated by a gap and connected to a high-frequency alternating voltage source. The charged particles, by crossing the gap, experience an electric field, that causes them to accelerate toward one of the electrodes, and a magnetic field, forcing them to follow a circular path. The frequency of the alternating voltage could be adjusted so particles complete one circle in the same amount of time it takes to switch the polarity of the electric field. This ensures that the particle continues to gain energy passing through the electrodes, resulting in a spiral path of increasing radius.

During the early 1930s, scientists first began exploring the use of high-energy beams to probe the inner working of atoms and subatomic particles. Ernest Rutherford discovered in 1919 a reaction between a nitrogen nucleus and an alpha particle. All research activities in nuclear physics until 1932 were performed with alpha particles, released by the decay of naturally radioactive elements. Natural alpha particles have kinetic energies as high as 8 MeV, but, according to Rutherford, it was necessary to accelerate alpha particle ions, artificially, to even higher energies, in order to observe the disintegration of heavier nuclei.

Over the next decades after the 1930s, accelerator technology continued to evolve and improve, leading to the development of linear accelerators, or linacs, which use electric fields to accelerate particles in a straight line. The first linac was built in the late 1940s, and since then, linear accelerators have become a fundamental tool for particle physics research, enabling scientists to probe the properties of particles with ever-greater precision and accuracy.

In the 1960s and 1970s, the discovery of new subatomic particles and the development of new accelerator technologies paved the way for the construction of large, high-energy colliders, such as the SPS at CERN, in Switzerland, and Tevatron in the USA. Scientists started to explore the energy range up to several hundred GeV and established the validity of the Standard Model in this range of energies.

One of the most significant developments in the history of particle accelerators came along with the construction of the LHC [11], at CERN, to accelerate protons to multi-TeV energies in a 27 km long high-vacuum ring. The LHC allowed groundbreaking discoveries in particle physics, including the discovery of the Higgs boson in 2012, which helped to complete the Standard Model.

Nowadays, accelerator technology continues to advance and the design of the next generation of particle accelerators, such as the FCC [12] at CERN and the ILC [13] in Japan, is under investigation through ambitious global R&D programs.

Different types of particle accelerators exist at the state of the art, classified into several categories based on their design and operating principles. Some common ways to classify particle accelerators include:

- Accelerator type: linacs and circular accelerators (such as synchrotrons and cyclotrons).
- Accelerated particle: electrons, protons, ions, and positrons.

- Energy Range: low-energy accelerators, few hundred keV, or high-energy accelerators, such as the LHC, capable of accelerating particles to energies on the order of TeV.
- Application: medical accelerators used in radiation therapy, industrial accelerators used for material analysis, and research accelerators used for studies in high-energy physics-
- Acceleration mechanism: RF cavities and plasma wakefield acceleration.

Focusing on the classification based on the accelerator typology:

- Linacs employ RF cavities to accelerate particles in a straight line. Some of the most notable linear accelerators include the Varian TrueBeam linac [14], used in radiation therapy for cancer treatment and able to deliver high-energy X-rays and electrons to a patient's tumor with high precision and accuracy; the Elekta Synergy linac [15], allowing for precise targeting of tumors, reducing the risk of damage to healthy tissue; LCLS X-ray laser at SLAC in USA, able to produce 120 X-ray pulses per second at energies from about 200 eV to about 11 keV [16]; the European XFEL in Hamburg, Germany, generates extremely intense X-ray flashes [17]; ERL linacs [18, 19] designed to recover a large portion of the energy used to accelerate the electron beam, making them more efficient than traditional linacs, in use at the JLab in USA, at the MAX IV Laboratory in Sweden, at the SPARC_LAB laboratory in Italy and PAL in South Korea.
- Circular accelerators use a combination of magnetic and electric fields to accelerate particles in a circular path. Examples of circular accelerators include synchrotrons and storage rings such as the LHC at CERN, the RHIC [20] at Brookhaven National Laboratory, the Tevatron at Fermilab in USA and the COSY [21] accelerator at the Institute for Nuclear Physics in Jülich, Germany.

A particle accelerator usually includes a source of charged particles, an accelerating structure, different focusing elements (magnetic and/or electric fields to guide and focus the particle beam), beam diagnostics monitors to measure and monitor the properties of the particle beam (position, intensity, and energy spread), a target and experimental areas where the accelerated particles are used for a specific application, such as scientific research, medical treatments, or industrial processes.

Protons and ions are generally produced using glow discharge columns [22], then accelerated first in electrostatic accelerators and then in linear accelerators. To increase the energy of heavy ion beams, single-charged ions are guided through a thin metal foil after some acceleration, in order to strip off additional electrons. Maximum ionization can be achieved by using more than one stripping stage at different energies.

The production of antiprotons requires much more elaborate procedures. In general, a high-energy protons beam is directed at a heavy metal target, where antiprotons are produced as a result of hadronic interactions with the target material. Antiprotons are then collected by strong focusing devices and further accelerated.

Electrons can be emitted at practical temperatures by a heated cathode, also known as a thermionic gun. A strong laser pulse may also be used to create a large number of electrons within a short pulse of energy. In RF guns, the cathode is directly inserted into an accelerating radio frequency field.

As with antiprotons, positrons are created by directing high-energy electrons on a heavy metal target which, through an electromagnetic shower and pair production, produces positrons, then collected and accelerated by a strong magnetic field.

1.2 Fundamentals of RF-based accelerators

In the last 70 years, the optimization and development of RF technology have been crucial in the development of high-energy colliders, allowing for particle physics discoveries, with increasing luminosities and center-of-mass energies.

Different types of RF cavities can be used in particle accelerators, depending on the specific application and requirements of the accelerator. Some examples include:

- Drift-tube cavities: typically used in linacs, consisting of a series of cylindrical metal tubes with alternating positive and negative charges. The produced electric field accelerates the particles as they pass through the cavities.

- Standing-wave cavities: used in circular accelerators, such as synchrotrons or cyclotrons. A resonant cavity generates a standing wave of an electric field, which accelerates the particles as they pass through the cavity.

- Superconducting cavities: particularly suitable for high-energy accelerators. They are made of superconducting materials and can carry much higher currents without losing energy to resistance.

- Coupled-cavities: a series of interconnected cavities, each one tuned to a specific resonant frequency are used to continuously accelerate particles, leading to higher energy gains over a shorter distance.

In Figure 1.1, a schematic representation of a typical superconducting elliptical RF cavities chain and the corresponding electromagnetic field profile are shown. The charged particles gain energy passing through the cavity, oscillating at a specific frequency, and lose energy when leaving the cavity. This process is repeated as the particles travel through the series of RF cavities, each one adding additional energy to the beam. Traveling along the axis of the RF structure, particles gain kinetic energy as a result of the stored electromagnetic energy, producing accelerating fields of up to 120 MV/m at X-band frequency [23].

To reduce the required RF peak power, structures operating at higher RF frequency can be adopted, as they require lower pulse energy for the same electric field in the structure. Combining short RF pulses, cryogenic temperature, and high-frequency operation, may result in significant advancements for high-gradient RF metallic structures in the coming decade.

However, it is unlikely to achieve gradients in the GV/m range using high-frequency metallic structures due to limitations in fabrication tolerances and beam instability caused by wake-field effects in corrugated structures. Wakefields are electromagnetic disturbances caused by discontinuities in the accelerating structure boundaries, causing energy spread, off-axis deflection, and beam loss. The transverse wake-field

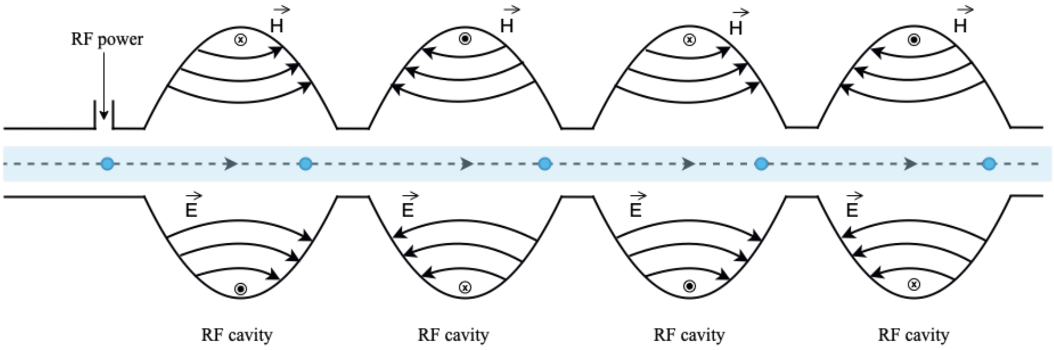

Fig. 1.1 Electric and magnetic field profiles in elliptical shaped superconducting RF cavities.

intensity decreases with increasing structure aperture and increases with beam offset from the structure symmetry axis. Therefore, the use of high-frequency structures to achieve higher gradients is limited by potential beam quality degradation from wake-field effects.

Promising results have been achieved at the SLAC FACET facility with a 140 GHz RF structure [24]. The highest gradient achieved was 300 MV/m, with a peak surface electric field of 1.5 GV/m and a pulse length of 2.4 ns.

Electric fields in copper cavities can be enhanced by cooling the cavities below 77 K [25], leading to a decrease in RF surface resistance, coefficient of thermal expansion, and crystal mobility, and an increase in thermal conductivity and hardness, hence lowering the breakdown rate. Studies have shown that an X-band structure can reach an accelerating gradient of 250 MV/m at 45 K with a breakdown rate of 2×10^{-4}/pulse/m, which is the largest reported gradient for this breakdown rate.

The LHC is a prime example of an RF-based particle accelerator, based on a sophisticated system of superconducting magnets to propel and steer beams of protons along a circular path. The protons are subjected to several acceleration stages, gradually reaching high energies, before being directed towards collision points around the ring. As a result of these collisions, a diverse array of subatomic particles are generated and subsequently detected and analyzed through a series of experiments.

The LHC employs 16 RF superconductive cavities, housed in four cryomodules. The cavities are powered by high-power klystrons, i.e. electron-beam-containing tubes that modulate their intensity to 400 million oscillations per second. A waveguide made of conductive metal directs energy to each cavity, specifically designed to resonate and amplify the electromagnetic waves. Each cavity is capable of reaching a maximum voltage of 2 MV, reaching a total potential of 16 MV. In a time window of 20 minutes, bunches of particles pass through the RF cavities over 10 million times, increasing their energy from 450 GeV to 6.5 TeV, i.e. 14 times the particles' initial injection energy.

The LHC represents a significant breakthrough in particle accelerator technology, but to achieve even higher energy levels, the next generation of RF-driven colliders such as the FCC [26], ILC [27] and CLIC [28], have been proposed. The FCC study, hosted by CERN, aims to design and construct a 100 TeV hadron collider in a 100 Km long tunnel, representing a significant step up from the capabilities of the LHC. The idea is to generate acceleration gradients of 30 MV/m for ILC and 150 MV/m for CLIC, with a 30 GHz frequency operation mode. To meet these specifications, accelerators that are several tens of kilometers long are required. Therefore, despite the potential for significant advancements, the proposed next-generation RF-driven colliders face significant challenges. Technical limitations such as maximum fields in super-conducting magnets for hadron machines, synchrotron power losses in Lepton machines, and breakdown effects at metallic walls of RF cavities, along with practical issues such as their large size and cost, pose significant obstacles to their development.

The research community is constantly pushing the boundaries of particle accelerator technology, developing new technologies and techniques to improve their performance. The ongoing innovation process aims to create more compact, efficient, and powerful particle accelerators, opening up new possibilities for their use in a broad range of applications.

1.3 Fundamentals of plasma-based accelerators

Over the recent decades, it has become clear that RF technology is reaching its limits in terms of achievable accelerating gradients. Currently, the maximum achievable electromagnetic field is limited to approximately 150 MV/m, due to surface breakdown effect [29, 30]. Plasma-based acceleration method has shown promising results in the last years, introducing the possibility for the generation of larger electric field gradients, with respect to RF-based accelerators, in centimeter scale structures [31–33].

As mentioned in Sec. 1.2, in a traditional RF-based accelerator, charged particles are accelerated through a series of RF cavities, typically made of copper and shaped like a hollow tube. The cavities are powered by RF generators, which produce a high-frequency electromagnetic field. Plasma-based accelerators, on the other hand, use plasma, an ionized gas, to accelerate charged particles to high energies.

The basic working principle of plasma-based accelerators involves the creation of wakefields, introduced in Sec. 1.2, i.e. a plasma wave, in which charged particles can be accelerated. The process involves a driver pulse, such as a high-power laser or a high-energy electron beam, to ionize a neutral gas, creating the plasma. The driver pulse creates a strong electric field in the plasma in which charged particles, such as electrons or positrons, are then injected. The plasma ions have a much greater mass compared to the electrons and, as a result, they move slowly compared to the electrons. Therefore, ions do not follow the fast-moving electrons and remain relatively stationary, creating a region of positive charge along the path of the drive pulse. After the driver passage, the plasma electrons rush back into the ion channel, attracted by the transverse restoring force of the positive charge. In this way, a space charge-driven oscillation is excited, generating alternating regions of negative and positive charge, thus inducing a strong longitudinal electric field behind the driver, the so-called plasma wakefield. Therefore, if a witness-charged particle bunch is injected behind the driver at the correct distance and phase, it is accelerated with high gradients, in some cases exceeding 100 GV/m.

The concept of plasma-based acceleration is illustrated in Fig. 1.2, where a drive pulse enters the plasma and expels the electrons of the plasma outward. In Fig. 1.2a the driver is a laser, while in Fig. 1.2b the driver is a particle beam. The first case is referred to as laser wakefield acceleration or LWFA, and the second one is referred to as plasma wakefield acceleration or PWFA.

By means of high-energy and high-density driver bunches, PWFA-based strctures can reach extremely high accelerating fields for very long distances [34], if compared to a laser-driven scheme. The latter is limited by non-negligible effects like diffraction, dephasing, and depletion of the laser pulse while propagating through the plasma.

Plasma-based accelerators are still in the research stage and not yet as developed as RF-based accelerators, but scientists believe that they could potentially be more compact and energy-efficient than RF-based accelerators.

Some examples of plasma-based accelerators currently in use include:

- The FACET-II facility at SLAC National Accelerator Laboratory.
- The AWAKE experiment at CERN AWAKE is a proof-of-principle experiment that uses a proton-driven plasma wake-field accelerator to accelerate electrons.
- The LUXE experiment at DESY uses a laser-plasma acceleration to generate high-energy photons.
- The HiLASE facility in the Czech Republic is a high-power laser facility based on laser-plasma acceleration to generate high-energy protons, electrons, and ions.
- The PEARL facility at Imperial College London in the United Kingdom.

Both RF-based and plasma-based accelerators have advantages and disadvantages, and the choice between them depends on the specific application and the required characteristics of the accelerated particles. RF-based accelerators are a well-established technology with a proven track record, widely used and providing high beam quality and stability. However, they can be large, complex, and expensive to construct and maintain, and they may not be as energy-efficient as other types of accelerators. Plasma-based accelerators have several potential advantages over traditional RF-based accelerators such as high energy density over shorter distances, compactness, cost-effectiveness, and high efficiency. However, one of the main drawbacks of plasma accelerators is the production of relatively poorer beam quality, due to higher energy spread and transverse size, with respect to conventional RF techniques. In order to tackle this problem and produce a reliable and competitive plasma-based accelerator technology, a big research consortium, EuPRAXIA, was recently established [2]. The main objectives of the EuPRAXIA design studies are introduced in the next Chapter.

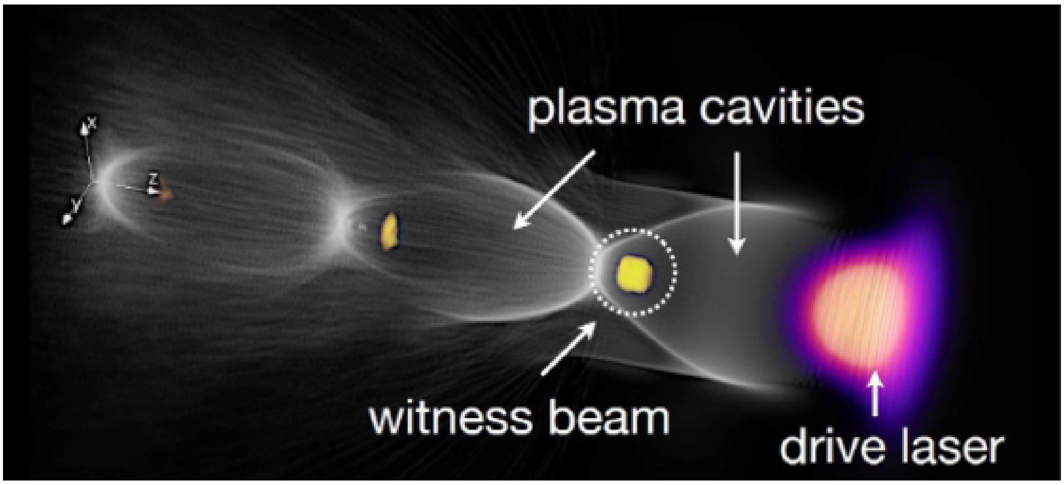

(a) PWFA

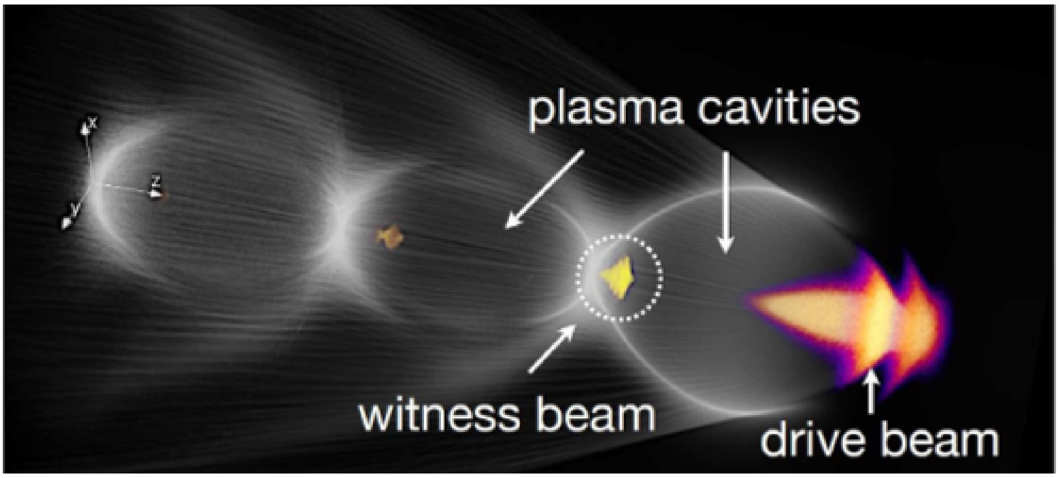

(b) LWFA

Fig. 1.2 Wakefield generation and electron beam acceleration in a plasma accelerator. (a) Behavior in a laser-driven plasma accelerator (LWFA); (b) Behaviour of a beam-driven plasma accelerator (PWFA) (Image credits: A. Martinez de la Ossa [2])

Chapter 2

The EuPRAXIA Design Study

2.1 The EuPRAXIA@SPARC_LAB concept

The EuPRAXIA project aims at exploring the potential of plasma-based acceleration for high-energy physics. The study is the result of a collaboration between numerous research institutes and universities from across Europe and is supported by the European Commission through its Horizon 2020 research and innovation program. The EuPRAXIA Desing Study goal is to establish the technical feasibility of plasma accelerators as a tool for particle physics research and to explore their potential for applications in a wide range of fields, including medicine, biology, and materials science. In particular, the European project EuPRAXIA will allow users to access high-brightness beams with energies in the range from 1 to 5 GeV. In order to achieve this goal, the EuPRAXIA consortium developed a comprehensive design for a plasma accelerator based on the PWFA concept.

The initial objective of the EuPRAXIA design study is the development of a site-independent blueprint for a plasma accelerator facility in Europe. During the EuPRAXIA design process, it became clear that facilities in Europe, suitable to host portions of EuPRAXIA, were already available. As a result, efforts have been made to adapt the EuPRAXIA concept to European infrastructures and capabilities. In its first implementation phase, the EuPRAXIA consortium objective has been the construction of a PWFA facility, named EuPRAXIA@SPARC_LAB at the LNF-INFN of Frascati in Italy.

The EuPRAXIA@SPARC_LAB accelerator facility is designed to generate electron

beams using an innovative hybrid compact RF injector. The injector includes an S-band photo-injector and an X-band linac booster, coupled with a plasma accelerator module. The accelerated electrons are not internally caught from the plasma, but, adopting an external-injection configuration, are obtained from an external pre-accelerated witness bunch. In particular, to obtain ultra-short (less than 10×10^{-15} s) and high-quality (low energy spread and emittance) electron beams, the SPARC-like S-band photo-injector produces and pre-accelerates bunches up to 170 MeV. The X-band RF linac increases the electron energy to 1 GeV. A plasma acceleration structure will follow, adding a final boost of 2 GeV to the beam. The total length of the EuPRAXIA@SPARC_LAB accelerator will be approximately 50 meters. The adopted configuration was guided by the expertise acquired at SPARC_LAB, where high-brightness electron beams have been reproducibly and stably generated and manipulated, fulfilling the requirements of plasma-based experiments and advanced radiation source generation.
The most challenging aspects in the facility realization relate to (i) improving and controlling beam energy spread and transverse emittance, (ii) increasing shot-to-shot stability, (iii) improving machine operability and maintainability, and (iv) increasing achievable repetition rates. In more detail, the EuPRAXIA scientific and technical goals include the following:

- Single and multi-stage acceleration of electron beams to final energies between 1 and 5 GeV, with a pulse duration of a few femtoseconds, with a transverse emittance of about 1 mm mrad, and with relative energy spread reaching from a few percent down to a few 10^{-3} total and a few 10^{-4} in a 1 μm slice of the beam. The EuPRAXIA specifications approach the regime of modern FELs and open various application paths.

- Highly compact machine layout, initially realizing at least a factor 3 gain in required floor space for the facility with accelerator and user areas, implementing a realistic stepwise strategy for the miniaturization of the particle accelerator itself by a factor of 10 and beyond in its most compact version.

- Development and construction of new generations of petawatt-scale pulsed lasers as drivers for plasma wakefields, together with industry and laser institutes, able to operate with high stability at 20 to 100 Hz, therefore enabling laser-based and beam-based fast feedback.

- Development and construction of a compact beam driver based on X-band RF technology from CERN.
- Development and construction of distributed and adaptable user areas that can take advantage of the capability of numerous parallel user lines for laser-driven accelerators. These areas could be used to produce ultra-fast electron and photon pulses with inherently short pulse durations, and for generating quasi-point-like X-ray emissions within plasmas. Furthermore, unique pump-probe configurations can be achieved through the synchronization of EuPRAXIA particles and laser beams.

In summary, the accelerator design for the EuPRAXIA project is based on the use of laser and plasma wake-field acceleration to accelerate particles to very high energies in a much shorter distance than traditional RF-based accelerators. The project is based on advanced plasma sources, magnetic elements and beam diagnostics to optimize the accelerator design and achieve the desired energy gains.

2.2 High-gradient quadrupoles for EuPRAXIA accelerator facility

The SPARC_LAB experimental facility located in Italy is primarily dedicated to conducting experiments related to plasma-based acceleration techniques. The primary objective is to produce accelerating fields that can reach values of the order of GV/m, while simultaneously ensuring that the electron bunch being accelerated maintains high quality in terms of both energy spread and emittance. The goal is to host the EuPRAXIA European Facility, which will include a soft X-ray FEL, driven by a 1 GeV high brightness linac based on plasma accelerator modules, as mentioned in Sec 2.1.

The achievement of dense beams is crucial for the successful implementation of PWFA applications. In [35–37] is shown that a driver bunch with density n_b induces an accelerating field proportional to the ratio n_b/n_p, where n_p is the plasma density. Considering the witness bunch, it must be shorter than the plasma wavelength λ_p [38]. Moreover, for optimal acceleration, it must be transversally matched to the plasma in terms of the β function. In the blowout regime, the equilibrium is given by Eq. 2.1, where r_e is the electron radius and γ is the relativistic Lorentz factor.

$$\beta_{eq} = \sqrt{\frac{\gamma}{2\pi r_e n_p}} \tag{2.1}$$

The condition expressed in Eq. 2.1 is quite hard to be reached for low-energy beams. In particular, to achieve the required beam transverse dimensions for PWFA applications, a focusing system with a short focal length and a very high gradient of several hundred T/m is necessary. The system must also be tunable, to adjust to different beam energies and future linac upgrades. Due to the ultra-high vacuum chamber that houses the focusing system, compactness is critical. Therefore, the key characteristics requested by the design of the magnetic elements can be summarized as follow:

- High gradient: quadrupole magnets are needed to provide a strong magnetic field gradient to focus the electron beam. The use of advanced materials, such as high-temperature superconductors, is necessary to achieve the necessary magnetic field strength.
- Compact design: EuPRAXIA aims to develop a compact accelerator, so the quadrupole magnets need to be designed to take up as little space as possible. The use of innovative magnet designs, such as permanent magnet quadrupoles or high-gradient, iron-dominated electromagnets, was investigated.
- High precision: The electron beam in EuPRAXIA must be focused to very high precision to achieve the desired beam quality. The quadrupole magnets must therefore be designed to have very tight manufacturing tolerances and to maintain their magnetic field strength and homogeneity over time.
- High reliability: The EuPRAXIA accelerator will be used for a wide range of applications, requiring the use of materials and designs that can withstand high levels of stress and thermal cycling.

Adopting already existing solutions such as tunable PQMs or hybrid high gradient quadrupoles was not possible. PMQs are currently considered the state of the art [39, 40] in focusing systems and are widely used in modern particle accelerators. They can provide strong field gradients of up to 520 T/m when using standard materials [41], and up to 560 T/m when employing neodymium-iron-boride materials [42]. Recently, alternative solutions such as plasma lenses [43, 4, 44] have been proposed and tested in experiments, but PMQ-based systems still provide superior performance. PMQs are relatively simple to design and manufacture, and their performance can be optimized through a careful selection of materials and geometries. Permanent quadrupoles offer several advantages over conventional electromagnets for use in PWFA systems. They are more compact and cost-effective, and they do not require the cooling and power systems needed for electromagnets. They are also more reliable and have a longer lifespan. The location of the PWFA module in the SPARC LAB linac and detail of the PMQs triplets are shown in Fig. 2.1.

The EuPRAXIA PWFA experimental setup includes a capillary tube, beam diagnostics, plasma diagnostics, and two symmetric PMQs triplets [38] based on Halbach Structure [45]. The quadrupole magnets create a strong magnetic field that varies along the beam axis, which focuses or defocuses the electrons depending on their position in the beam. The focusing action allows the electrons to stay on a precise trajectory as they travel through the accelerator, which is essential for achieving the desired beam properties.

The features of the foreseen quadrupole magnet prototypes for the SPARC_Lab facility, which have to be tested at CERN and at INFN-LFN with the proposed rotating-coil system, are summarized in Table 2.1.

Table 2.1 Specifications of the foreseen EuPRAXIA quadrupole prototypes [46].

Parameter	Value
Aperture diameter	⌀30 mm
Reference radius r_0	10 mm
Maximum magnetic field gradient	50 T/m
Minimum magnetic field gradient	10 T/m
Effective length	390-440 mm

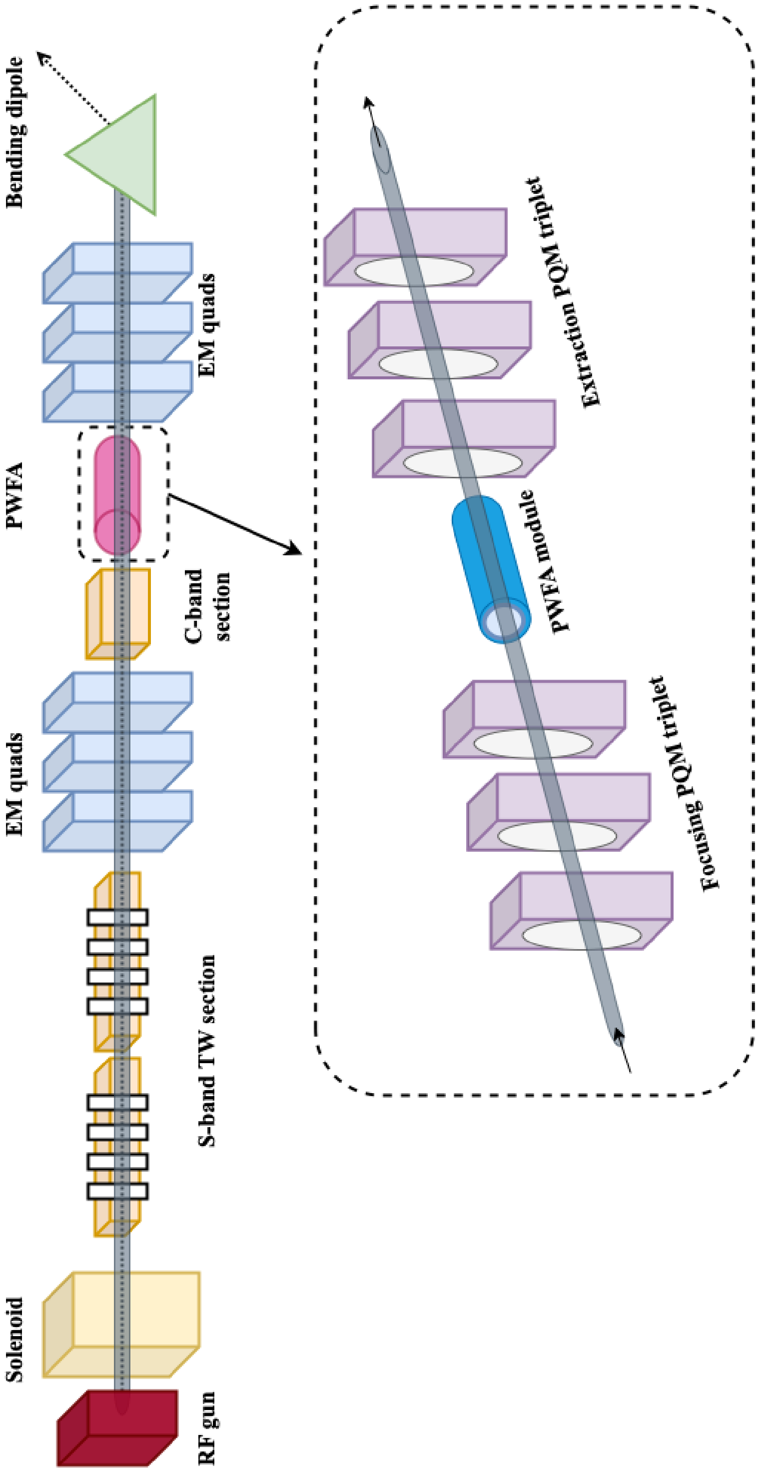

Fig. 2.1 Schematic reproduction of EuPRAXIA beam-line final layout with a focus on the main elements and a detail of the PMQs triplets.

Chapter 3

Magnetic measurements for accelerator magnets

Several non-destructive and reliable methods exist for measuring magnetic fields in accelerator magnets, each with its own advantages and limitations. Some of the most commonly used methods include Wire Measurement Systems, Hall Probes, NMR Probes, and Rotating Coil magnetometers. In this chapter, the different approaches to magnetic field measurement in accelerator magnets are introduced, including the underlying principles, capabilities and limitations.

3.1 NMR probes and Hall probes

NMR probes are field sensors used for measuring the magnetic field strength and distribution. NMR probes detect the magnetic field-induced precession of the nuclei of certain atoms, such as hydrogen or proton, in a material. The precession frequency is proportional to the magnetic field strength and can be used to determine the magnetic field distribution. NMR probes can be classified into two types: inductive NMR probes and resonant NMR probes. Inductive NMR probes are based on the voltage induced in a coil, while resonant NMR probes are based on the detection of the resonant frequency shift of a sample in a magnetic field.

The NMR method's accuracy in measuring the absolute magnetic field strength in accelerator magnets is 0.1 ppm, making it a useful tool for calibration or as an absolute reference. The defined accuracy assumes a homogeneous field, with variation

less than 100 ppm/mm, often found inside dipole and solenoid magnets.
As an example, Metrolab PT2025 NMR transducers can provide absolute and relative accuracy of 0.1 ppm and 5 ppm, respectively, for the main field measurement [47]. NMR probes offer several advantages, such as high spatial resolution and high accuracy. However, NMR probes are not suitable for gradient measurements (for example fringe fields), and exhibit a limited lower range of operation, e.g 0.033 T for the Metrolab PT2025 probe. Different probe materials can be used to measure fields ranging from 0.05 mT to 14 T. Further field parameters must be determined by using other techniques, especially in fringe field regions and in higher-order magnets.

Hall probes are based on the Hall Effect [48], which states that a magnetic field will cause a separation of charges in a conductor, producing a voltage proportional to the strength of the magnetic field. Hall probes are often integrated on NMR transducers support and widely used for local mapping of straight and curved magnets [49–51]. The main advantages are high spatial resolution, due to the size of the sensing element on the order of tens of mm^2, a wide input range and the possibility to be adopted for the characterization of non-homogeneous fields, both in static and dynamic conditions.
The main disadvantages are the relatively low accuracy (0.1%) and the strong temperature dependence of the metrological performance. However, errors frequently arise due to elements of the sensor not being perfectly aligned and sensitive to in-plane field components (planar effect), as well as non-linear response. In the case of the Hall probes, the evolution from the traditional Hall device materials to graphene was investigated [52] and partially tested, with the aim to clear the issue of planar effects and make possible for precise detections, including at liquid-helium temperatures.
Hall probes have achieved several important advancements in recent years. Some of the key achievements include miniaturization and integration with other types of sensors, such as capacitive sensors, allowing for more compact and efficient magnetic field measurements, the development of high-temperature Hall probes, enabling magnetic field measurements to be performed in high-temperature environments, such as those encountered in superconducting materials and improved noise immunity and enhanced linearity [53].

3.2 Wire measurement systems

Wire measurement systems for magnetic field measurement are based on the motion of a straight, conductive wire within a magnetic field [54, 55]. The current in the wire is closed using a fixed wire, typically located inside of the magnet to reduce coil surface and noise. The main approaches within this principle are the Single Stretched Wire and Single Vibrating and Oscillating Wire methods.

The SSW method is a common technique for measuring magnetic fields and can be considered as reference equipment to measure main field strength and direction in static field dipole and quadrupole with high accuracy [56]. A conducting wire of Copper-Beryllium (Cu-Be) is guided by two precision displacement stages, at which the two end-points of the wire are fixed by ceramic ball bearings and kept electrically on a floating potential. The wire is displaced within the magnet aperture and pulled taut by means of a servo motor. The relative position of the wire is known with an accuracy of 1 μm. Finally, the return wire is routed through a field-free region. When the wire is moving inside the magnetic field, a voltage drop across the connection terminals. The voltage is measured and directly integrated by FDI [57] to obtain the flux linked with the surface that is traced out by the wire displacement. The SSW method is a highly precise technique for measuring magnetic field strength, with an accuracy of 100 ppm [58], field orientation with an accuracy of 0.1 mrad, and magnetic axis with an accuracy of about 0.1 mm.
However, the single stretched wire method has some limitations. As an example, The wire inside the magnet bore is connected to a voltage integrator, creating a loop sensitive to electromagnetic interference. Being the displacement range of the wire limited for small-diameter bore magnets, the resulting signal to noise ratio of the induced voltage is reduced. Consequently, the uncertainty on the magnetic center measurement position and field harmonics is increased.

The working principle for the vibrating wire and oscillating wire methods is quite similar: a conductive wire is set in vibration in a magnetic field. By measuring the change in frequency of the wire's vibration it is possible to determine the strength of the magnetic field.
The vibrating wire method uses an AC voltage to vibrate the wire at a specific frequency. The amplitude of the vibration, and thus the sensitivity of the method, is maximized at the natural resonance frequencies of the wire. By aligning the wire with

the magnetic axis , the vibration amplitude can be minimized, allowing for precise measurement of the magnetic field. This process involves iterative measurements with a micrometer precision, ultimately limited by the precision of the geometrical survey to approximately 0.05 to 0.1 mm [7]. This method is particularly well-suited for measuring fields with weak transverse components, such as solenoids, where other methods, like the single-stretched wire approach, may not provide sufficient sensitivity.

The oscillating wire method sets the wire in motion at a lower frequency than resonance, reducing the sensitivity of the measurement but also the sensitivity of wire's vibrations amplitude to changes in damp conditions. By taking measurements at N points along a circular trajectory within the magnet aperture, it is possible to use the wire system to measure field harmonics with an accuracy of 0.05% [59].

3.3 Fixed coil magnetometers

The working principle of fixed coil magnetometers for magnet characterization [60] is based on the Faraday's law of electromagnetic induction, where a change in magnetic field induces a current in the fixed coil proportional to the field strength.

Differently from the wire based techniques, this method utilizes stationary coils with even hundreds of turns instead of moving conductors, spanning the entire length of the magnetic field or the region of interest. The voltage is induced by varying the magnetic field over time through alternating, ramping, or pulsing excitation current in the magnet. The accuracy is determined by the mechanical positioning of the wire. The achieved high accuracy is due to the precise mechanical control of the coil position, which allows for precise measurement of the magnetic field. Moreover fixed coil magnetometers can measure magnetic fields over a wide frequency range, from DC to high frequencies, and achieve high spatial resolution.

The AC-mole approach [61] represents a particular method for measuring magnetic fields, aimed at improving the accuracy of field harmonics measurement while retaining the benefits of stationary coils. In this method, measurement coils are fixed during the measurement and the magnet is powered in an alternating current mode . Once the measurement is complete, the coils are rotated to the next angular position to repeat the measurement procedure. The approach is particularly useful for determining the magnetic axis location in high-order correctors, with reported accuracy of 0.1 mm.

3.4 Rotating-coil magnetometers

The rotating coil magnetometer consists in a certain number of induction coils, i.e., field-sensing transducers based on Faraday's law of induction, rotated around the longitudinal axis of the magnet, according to the harmonic or rotating-coil method described in Sec 4.1. A voltage is induced as a result of the movement of the conductor, making this method particularly suitable for measuring the magnetic field multipoles. The method generally provides field error measurements with repeatability up to 1 ppm [62, 8, 63].

Rotating coil magnetometers offer several advantages over other magnetic measurement systems. They can achieve high sensitivity due to the large voltage signals generated by the rotating coils, proportional to the rotation speed.

Usually, induction coils can be realized either through conventional winding methods on composite support or printed on a PCB [60]. The coils can cover the entire length of the magnetic field or just the area of interest. Multiple coils can be placed in different transverse positions to evaluate the homogeneity of the magnetic field.

3.5 Research context and motivations

As part of an ongoing partnership between CERN and INFN-LFN of Frascati in Italy, a proposal has been made for the design and development of a small-radius rotating coil measurement system. The system is required to test the field quality of small-diameter (30 mm or higher) quadrupole magnets for the EuPRAXIA project. Precisely determining the characteristics of small-bore magnets used in particle accelerators is a difficult task for several reasons. One of the primary challenges is the potential for the sag of a cylindrical tube, such as the shaft housing the magnetometer and allowing its rotation inside the magnet bore. The sag can cause undesired flexural oscillations during rotation and affect the accuracy of the measured harmonics. In the case of an empty round bar, such as the magnetometer shaft, having diameter D

and length L, the sag can be estimated using the following expression [64]:

$$d = \frac{5}{\alpha} \rho g \frac{L^4}{ED^2} \tag{3.1}$$

where ρ is its average volume mass density, E its effective Young's modulus. The coefficient α has a value of 24 for a round bar and 48 for a thin cylindrical tube regardless of its thickness, with an error of less than 10 % when the thickness to diameter ratio is less than 5 %. However, increasing the aspect ratio $\lambda = \frac{L^4}{D^2}$ can result in greater sag and unwanted flexural oscillations during rotation, leading to decreased accuracy in the measured harmonics [65].

To address this issue, the coil bucking technique [58] can be used, as detailed in Sec. 5.3. This technique requires precise coil geometry to minimize the impact of mechanical imperfections. In addition, the smaller diameter of the rotating shaft reduces the rotation radius for the magnetometer, and the constraints on the coil turn density (typically ranging from 100 turns/mm^2 for multi-layer PCBs to 400 turns/mm^2 for multi-wire flat cables) limit the sensitivity of the magnetometer, particularly on the higher-order harmonics.

An example of a small-radius rotating-coil magnetometer is presented in [66], which describes a ⌀19 mm and 500 mm long rotating-coil probe ($\lambda = 173\ m^2$) built to test permanent magnet quadrupoles for CERN's Linac4. The proposed design, based on a machined stack of 80 PCB layers, proved ineffective in rejecting spurious harmonics due to mechanical imperfections.

In [67], a ⌀8 mm rotating-coil system to test CLIC prototype magnets with an aperture of less than ⌀10 mm, necessary to obtain the very high gradient of 200 T/m, is discussed. This extremely small size was achieved thanks to the choice of synthetic sapphire as the support material, and the short required length of only 150 mm ($\lambda = 8\ m^2$). Synthetic sapphire (Al_2O_3) has an exceptionally high $\frac{E}{\rho}$ ratio of around $110 \times 10^{12} \mathrm{m}^2 s^{-2}$, i.e., almost ten times as high as fiberglass. Synthetic sapphire has the advantage of being able to be sintered and polished with tolerances as small as a few micrometers, making it an excellent choice for high-precision coil supports. However, its high cost and limited production capabilities prevent it from being used in larger sizes.

To avoid significant sag in simply supported shafts, coils that are considerably shorter than the magnet are often used to measure magnets with a length of over one or two meters. For example, a rotating-coil system was developed at CERN for measuring the local magnetic flux density of quadrupoles for the HL-LHC Insertion Region (IR) [68], characterized by large bore diameter (around 90 mm). Short coils were also designed to reject pseudo-multipole components in short magnets dominated by the fringe field [69].

The geometric requirements imposed by the EuPRAXIA quadrupole magnets, reported in Tab. 2.1, exceed the performance of all these systems. The smallest foreseen bore diameter is 30 mm, which applies to the final focus quadrupoles and drives the dimensional requirement for the proposed rotating-coil shaft diameter.

In this context, the design, calibration, and validation of $\varnothing$26 mm diameter rotating-coil system. to be used for the measurement of the EuPRAXIA quadrupole magnets, is presented. The magnetometer design, based on PCB technology, represents a unique challenge due to its higher aspect ratio, which is 30 % higher than the current state-of-the-art, and the need to cover the full effective length of the magnet (500 mm or more), which is challenging and requires a substantial improvement over the previous $\varnothing$19 mm design.

The measurement system design proposal has been made to develop a rotating coil system for quadrupole characterization based on COTS components. COTS components are readily available on the market, cost-effective, and can be quickly and easily integrated into a measurement system. In particular, the proposed system features a novel mechanical asset and the introduction of a commercially available carbon fiber tube to house the PCB magnetometer. Another fundamental goal was to simplify the design as much as possible, taking advantage of open-source software packages, and widening the accessibility of this technology. This approach significantly reduced the cost and time required to construct the rotating coil system, making it more accessible to a wider range of users. The measurement requirements for the proposed $\varnothing$26 mm rotating-coil system are summarized in Table 3.1 [46].

Table 3.1 Measurement accuracy specifications for characterization of EuPRAXIA quadrupole magnets.

Parameter	Accuracy
Integrated gradient	100 ppm
Field harmonics @ r_0	100 ppm
Magnetic axis	150 μm

Part II

Proposal

Chapter 4

The harmonic-coil method

The *harmonic-coil* method [70–74] is one of the most relevant techniques to test accelerator magnets. To create an effective framework for developing and characterizing the proposed rotating coil measurement system, this chapter offers mathematical formulations related to magnetic fields generated by accelerator magnets.

4.1 Two dimensional multipole fields expansion

Large-scale particle accelerators, such as the 27 km long LHC, often rely on saddle-shaped coils for magnets manufacturing, wound, and cured individually before being assembled together. The current-carrying conductors run parallel to the beam orbit, except for the relatively short coil heads, where they are guided across and turn around.

For the purpose of field computation or field quality analysis, in the center of the magnet and far from the magnet ends, the conductors can be considered rectilinear and parallel. Within the conductors, the current density is uniform and flows parallel to the magnet longitudinal axis direction.

Considering a specific region free of charges and current sources, such as the interior of an accelerator's vacuum chamber under ideal conditions, without the beam, and assuming the absence of propagating electromagnetic waves, any magnetic field produced by constant currents outside the vacuum chamber satisfies Eqs. 4.1 and 4.2.

$$\nabla \cdot \vec{B} = 0 \tag{4.1}$$

$$\nabla \times \vec{B} = 0 \tag{4.2}$$

The Eq. 4.1 is one of Maxwell's equations, and Eq. 4.2 follows from Maxwell's equation considering that $\vec{J} = 0$, $\vec{B} = \mu_0 \vec{H}$, and in the magneto-static regime, the derivatives with respect to time vanish.
It is possible to demonstrate that a magnetic field $\vec{B} = (B_x, B_y, B_z)$, with B_z constant, and B_x, B_y given by Eq. 4.3, where C_n is a complex constant, satisfies Eqs. 4.1 and 4.2.

$$B_y + iB_x = C_n (x + iy)^{n-1} \tag{4.3}$$

The demonstration is conducted by applying the differential operator $\frac{\partial}{\partial x} + i\frac{\partial}{\partial y}$ to both sides of Eq. 4.3. Applying the operator on the right side, the condition in Eq. 4.4 is obtained, while considering the left side, the condition in Eq. 4.5 is obtained.

$$(\frac{\partial}{\partial x} + i\frac{\partial}{\partial y})C_n(x+iy)^{n-1} = C_n(n-1)(x+iy)^{n-2} + i^2 C_n(n-1)(x+iy)^{n-2} = 0 \tag{4.4}$$

$$(\frac{\partial}{\partial x} + i\frac{\partial}{\partial y})(B_y(x,y) + iB_x(x,y)) = (\frac{\partial B_y(x.y)}{\partial x} - \frac{\partial B_x(x,y)}{\partial y}) + i(\frac{\partial B_x(x,y)}{\partial x} + \frac{\partial B_y(x,y)}{\partial y}) \tag{4.5}$$

As a result, the combination of Eqs. 4.3,4.4 and 4.5 leads to conditions reported in Eq. 4.6.

$$\begin{aligned} (\frac{\partial B_x(x,y)}{\partial x} + \frac{\partial B_y(x,y)}{\partial y}) &= 0, \\ (\frac{\partial B_y(x,y)}{\partial x} - \frac{\partial B_(x,y)y}{\partial x}) &= 0 \end{aligned} \tag{4.6}$$

Finally, considering that B_z is constant, so any derivatives vanishes, and that B_x and B_y are z-independent, it is possible to conclude that the magnetic field in the form reported in Eq. 4.3 satisfies the conditions in Eqs. 4.1 and 4.2.

Fields in the form of Eq. 4.3 are known as *multipole* fields. The principle of superposition can be applied to deduce that a more general magnetic field can be constructed by adding together a set of multipole fields, as shown in Eq. 4.7:

$$B_y + iB_x = \sum_{n=1}^{\infty} C_n (x+iy)^{n-1} \tag{4.7}$$

The B_y and B_x represent the vertical and horizontal field components as a function of the position, $C_n = B_n + iA_n$ is the n-th complex harmonic coefficient, and B_n and A_n are the normal and skew harmonic coefficients, respectively.
A pure multipole field of order M has only the harmonic complex coefficient $C_M \neq 0$. The higher-order harmonic components represent deviations from the ideal magnetic field, and their magnitudes can be used to quantify the field quality or homogeneity of the magnet. Higher-order error harmonics refer to the magnetic field components that are not desired in the design of the magnet and are caused by imperfections in the magnet's manufacturing process. The allowed higher-order error harmonics are those that do not significantly affect the performance of the accelerator and can be corrected by using correction magnets or other means. Conversely, the not allowed higher-order error harmonics are those that can cause beam instabilities or other performance issues that cannot be easily corrected.

The units of C_n depend on the order of the considered harmonic coefficient, as an example, for a dipole magnet, the units of C_1 are T, for a quadrupole, the units of C_2 are Tm^{-1}, for a sextupole, the units of C_3 are Tm^{-2}, and so on.
It is convenient to specify harmonic coefficients C_n in dimensionless units, introducing a reference radius, r_0 [58]. The reference radius, which is typically set at $2/3$ of the magnet aperture radius, determines the boundary of the desired good field region where the particle beam is located. It is also the limit at which the field errors remain within acceptable tolerance values.
In most practical cases, being interested in the shape of the field rather than its absolute magnitude, the harmonic coefficients are normalized with respect to the main field component B_M (B_2 for a quadrupole magnet), as shown in Eq. 4.8, and expressed in units of 10^{-4}. This choice arises from the typical tolerance values of accelerator magnets, where the harmonics are in the order of 0.01% of the main field component. There are different applications and experiments for which having

a precise magnetic characterization is crucial [75–78].

$$c_n(r_0) = 10^4 \frac{C_n(r_0)}{B_M(r_0)} = 10^4 (\frac{B_n(r_0)}{B_M(r_0)} + i\frac{A_n(r_0)}{B_M(r_0)}) = b_n + ia_n. \tag{4.8}$$

It is convenient to explain the correspondence of the value assigned to the integer index n in Eq. 4.3 to a specific flux distribution, generated by a perfect magnet with 2n-poles: n = 1 is a dipole field, n = 2 is a quadrupole field, n = 3 is a sextupole field, and so on. In Fig. 4.1 the magnetic flux density corresponding to the field generated by an ideal dipole, quadrupole, and sextupole, are shown, each one for normal and skew magnet configuration. The cross-sections of iron-dominated multipole magnets of orders n=1, n=2, and n=3 are shown in Fig. 4.2.
For an ideal quadrupole magnet (n = 2), the main field components are expressed in Eq. 4.9. The amplitude of the two components varies linearly with the distance from the origin. The coefficients B_n and A_n of the series expansion determine the shape of the magnetic field lines.

$$\begin{aligned} B_x(x,y) &= \frac{1}{r_0}(B_2(r_0)y + A_2(r_0)x) \\ B_y(x,y) &= \frac{1}{r_0}(B_2(r_0)x - A_2(r_0)y). \end{aligned} \tag{4.9}$$

A quadrupole magnet in which only the coefficient B_2 is non-zero and the skew coefficient is $A_2 = 0$ is called a normal magnet and the field components can be expressed as in Eq 4.10, where $G = B_2/r_0$ is the field gradient, expressed in Tm^{-1}.

$$\begin{aligned} B_x(x,y) &= Gy \\ B_y(x,y) &= Gx \end{aligned} \tag{4.10}$$

The origin of the reference system is referred to as the magnetic center, and it represents the point where multipolar field components of order n<M are zero. The expansion coefficients B_n and A_n are a function of the excitation current level.

To conclude, the harmonic decomposition can be used to describe the field quality or field homogeneity of accelerator magnets. In this context, the harmonic decomposition is used to quantify the deviations of the actual magnetic field from the ideal magnetic field. The ideal magnetic field is the magnetic field that would be produced by a perfectly symmetric magnet with no manufacturing imperfections or misalignments. In reality, however, the magnetic field of a magnet will deviate from the ideal magnetic field due to various factors such as manufacturing tolerances, alignment errors, and eddy currents. By controlling the strengths and distribution of these multipole components, the field quality of the magnet can be improved. This is crucial for ensuring precise and stable beam trajectories in particle accelerators.

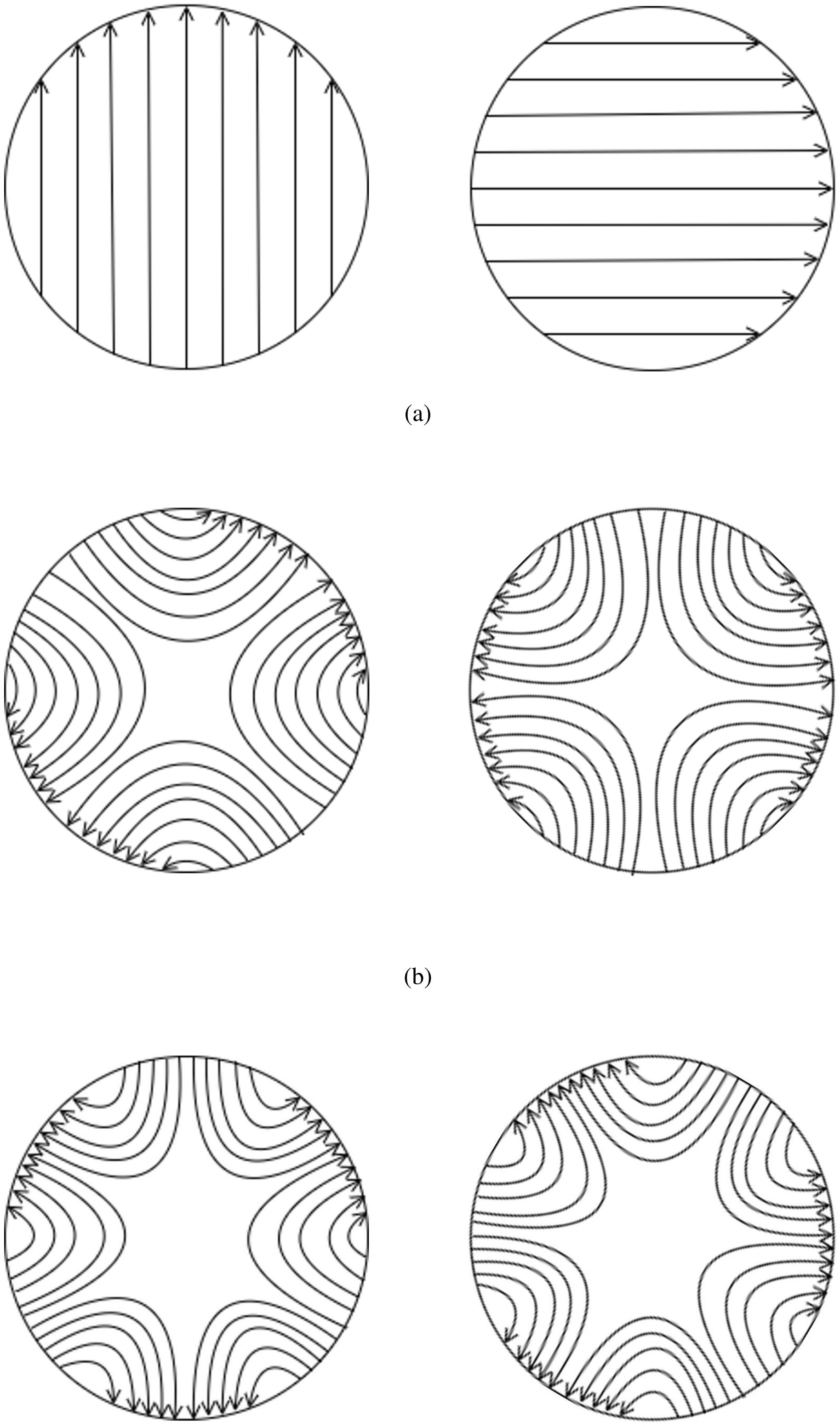

(a)

(b)

(c)

Fig. 4.1 Pure multipole field profiles.(**a**) Dipole (n=1), (**b**) Quadrupole (n=2) and (**c**) Sextupole (n=3). Field profiles on the left refer to normal magnets, and on the right refer to skew magnets.

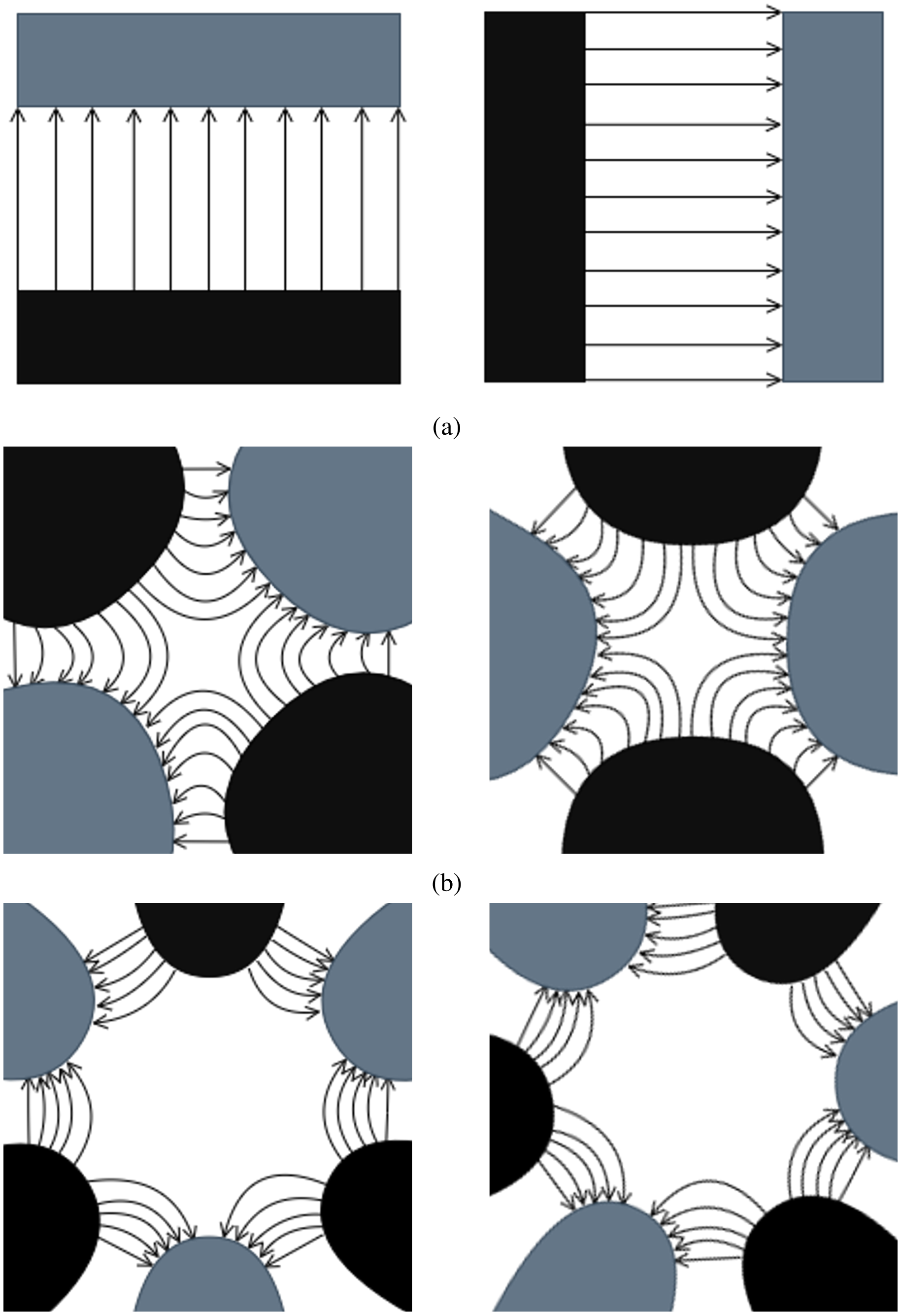
(a)
(b)
(c)

Fig. 4.2 Pole shapes for generating pure multipole fields.(**a**) Dipole magnet (n=1), (**b**) Quadrupole magnet (n=2) and (**c**) Sextupole magnet (n=3). Field profiles on the left refer to normal magnets, and on the right refer to skew magnets.

4.2 Induction coil magnetometers

Rotating-coil magnetometers measure magnetic fields by detecting the changes in flux induced in a sensing coil (also known as a pick-up or induction coil). This technique is based on Faraday's law of induction, which states that the voltage at the terminal of a sensing coil is directly proportional to the rate of change of the magnetic flux, as shown in Eq. 4.11, where Φ is the total magnetic flux linked with the coil.

$$U(t) = -\frac{\mathrm{d}\Phi(t)}{\mathrm{d}t}, \tag{4.11}$$

The measurement is generally performed by rotating the induction coil magnetometer in a static field. In the case of a point-like winding structure, i.e. assuming the induction coil is wound in a very compact pattern, resembling a point in the cross-section, the geometry of an ideal induction coil can be described by the complex points $\underline{z}_1$ and $\underline{z}_2$ shown in Figure 4.3, which represent the location of the conductor turns in the transverse plane of the magnet.

The reference system's origin does not need to coincide with the magnetic axis of the magnet being tested. The assumption remains valid also when analyzing the cross-section of a multi-turn and multi-layer coil. All of the winding turns can be assumed to be perfectly packed together on the central positions $\underline{z}_1$ and $\underline{z}_2$, in the analysis, with negligible uncertainty [79].

The cross-section representation of the induction coil magnetometer positioning in the bore of a magnet and the schematic top view of a rectangular-shaped multi-turn induction coil, of length L and width d, are shown in Fig 4.4.

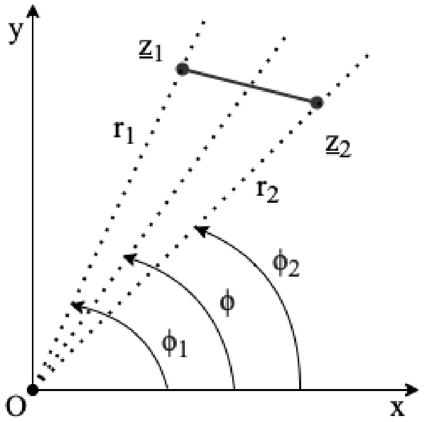

Fig. 4.3 Naming convention for angles and radii in the ideal case of a point-link coil winding pack [46].

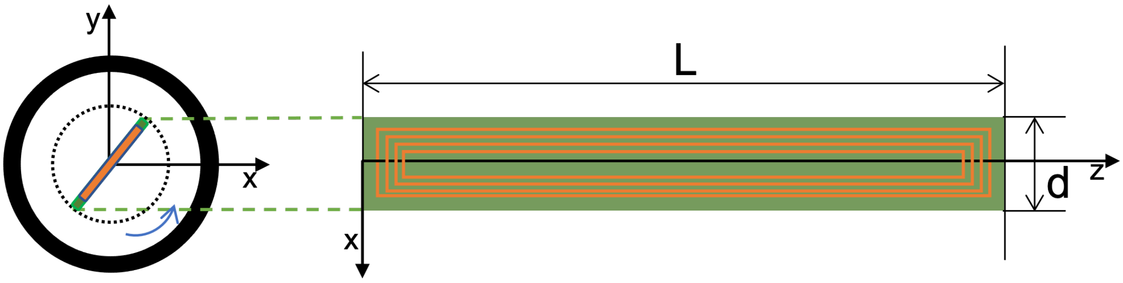

Fig. 4.4 Working principle schematic of the rotating coil method.

Given an induction coil with N turns, a total area A_c, and length L, the linked magnetic flux can be calculated as in Eq. 4.12, where $\underline{z}_1 = r_1 e^{i\phi_1}$ and $\underline{z}_2 = r_2 e^{i\phi_2}$. Considering Eq. 4.13, the total flux intercepted by the rectangular coil can be obtained from the real part of the $B(\underline{z})$ integral, as shown in Eq. 4.14.

$$\begin{aligned}\Phi &= N \int_0^L \int_{\underline{z}_1}^{\underline{z}_2} (B_y(x,y)dx - B_x(x,y)dy)\, d\underline{z} \\ &= NL \int_{\underline{z}_1}^{\underline{z}_2} (B_y(x,y)dx - B_x(x,y)dy)\end{aligned} \tag{4.12}$$

$$\int_{\underline{z}_1}^{\underline{z}_2} \underline{B}(\underline{z})d\underline{z} = \int_{\underline{z}_1}^{\underline{z}_2} (B_y(x,y)dx - B_x(x,y)dy) + i \int_{\underline{z}_1}^{\underline{z}_2} (B_y(x,y)dy + B_x(x,y)dx) \tag{4.13}$$

Equation (4.12) becomes

$$\begin{aligned}\Phi(\phi) &= NL\mathrm{Re}\int_{\underline{z}_1}^{\underline{z}_2}\underline{B}(\underline{z})d\underline{z} = NL\mathrm{Re}\int_{\underline{z}_1}^{\underline{z}_2}\sum_{n=1}^{\infty}\underline{C}_n(r_0)(\frac{\underline{z}}{r_0})^{n-1}d\underline{z} \\ &= \mathrm{Re}\sum_{n=1}^{\infty}\frac{NL}{nr_0{}^{(n-1)}}\underline{C}_n(r_0)(\underline{z}_2^n-\underline{z}_1^n) = \mathrm{Re}\sum_{n=1}^{\infty}\underline{C}_n\underline{S}_n e^{in\phi}\end{aligned} \tag{4.14}$$

The $\underline{S}_n$ are complex sensitivity coefficients, representing geometric factors and related to the position of the turns in the reference frame. The reference frame's origin is established to be coincident with the axis of rotation of the shaft. The sensitivity coefficients have units of $m^{(n+1)}$, where n is a non-negative integer, and their magnitude scales exponentially with n. These coefficients are usually normalized to $r_0^{(n-1)}$, as reported in Eq. 4.15, to express them in m^2 and have numbers numerically comparable. The complex field harmonic coefficients $C_n(r_0)$ are calculated from the measured flux as in Eq. 4.16. The $\underline{\Psi}_n$ are the complex coefficients of the Discrete Fourier Transform (DFT) of the measured flux, expressed in Eq. 4.17.

$$\underline{S}_n(r_0) = \frac{NL}{nr_0^{(n-1)}}(\underline{z}_2^n-\underline{z}_1^n) = \frac{NL}{nr_0^{(n-1)}}(r_2^n e^{in(\phi_2-\phi)}-r_1^n e^{in(\phi_1-\phi)}). \tag{4.15}$$

$$\underline{C}_n(r_0) = B_n(r_0)+iA_n(r_0) = \frac{\underline{\Psi}_n}{\underline{S}_n}r_0^{n-1} \tag{4.16}$$

$$\underline{\Psi}_n = \frac{2}{N}\sum_{k=1}^{N}\Phi_k e^{-2\pi i\frac{k}{N}}. \tag{4.17}$$

Chapter 5

Standard functionality rotating coil system design

In this chapter the proposed rotating coil system is introduced. The description includes the PCB-based magnetometer and the rotating-coil transducer. The adopted harmonic compensation technique, to enhance the sensitivity and accuracy of the system, is also discussed.

5.1 PCB based magnetometer design

Different techniques could be adopted for induction coil magnetometers manufacturing, including thick film, rigid printed circuit board or flex circuit board. The technology chosen for the proposed induction coil magnetometer was determined by factors such as geometrical precision, pre-existing PCB design rules, and geometrical design constraints based on EuPRAXIA magnets characteristics, outlined in Table 2.1.

The adopted technology for sensing coils manufacturing is the PCB technology, which is a widely recognized alternative to traditional wound coils [66–68]. While the manufacturing process for rigid PCBs can be particularly complex [80], they are currently the most widely available and reliable option for small-scale induction coil magnetometer design.

The PCB-based magnetometer design was characterized by precise positioning of copper tracks (within ± 2 μm) and accuracy up to 0.1% in gradient measurement,

which was achieved through meticulous calibration [63]. Furthermore, the PCB compact and flat structure allows for easy integration into rotating systems within limited space, such as the bore of the quadrupoles to be tested.
When designing a PCB-based magnetometer for rotating coil measurement systems, several parameters need to be considered to ensure optimal performance, including:

- Coil dimensions: length, width, and height, should be chosen based on the specific requirements of the application and considering their effect on coil's inductance, resistance, and current-carrying capacity.
- Wire and substrate material: copper is a common choice for wires due to its low resistance and high conductivity. However, other materials such as silver, gold, or aluminum may be used depending on specific needs. Usually FR4 epoxy resign is used for the substrate, but an alternative based on Kapton was considered.
- Number of turns: the number of turns affects coil inductance and current-carrying capacity, but also influences coil sensitivity.
- Coil shape: typically, the rectangular spiral pattern adopted for the design of PCB-based induction coils simplify the attempt at maximizing the number of turns in a given area, which increases the sensitivity of the coil, as shown in Eq. 4.15.
- PCB layout: the layout of the PCB should be designed to optimize the performance of the coil, including traces placement and routing, size and shape of the pads, and number of induction coils hosted by the PCB magnetometer.

The definition of design parameters involved balancing the desired performance of the PCB coil magnetometer with the manufacturing limitations, posed by the size and complexity of the PCB.
The EuPRAXIA project application presents a challenging scenario for the proposed magnetometer typology. As the application requires installation of the PCB-based magnetometer in the bore of a quadrupole magnet with a $\varnothing 30$ mm diameter, the total PCB width was limited to 25 mm and its length was extended to 640 mm, to cover the entire magnet length and its fringe field region. Moreover, the design of a small-radius rotating-coil system significantly impacts the size of the PCB, particularly the geometric width and area of each coil on the PCB magnetometer,

resulting in reduced sensitivity to field harmonic components. To counterbalance this effect, the coil turn density and area have been maximized to achieve the required accuracy in measuring field harmonics. In particular, the PCB coils design intent was to ensure coil output voltage peak at 500 mV, for a quadrupole flux density of around 4 T at the maximum measurement radius of 10 mm and a rotational frequency of approximately 1 rev/s.

The proposed PCB-based magnetometer consists of an array of five identical rectangular and planar coils, arranged radially. Figure 5.1 displays the schematic layout of a single layer of the proposed PCB array magnetometer. In a radial configuration, the PCB coil is oriented such that the axis of the coil is perpendicular to the direction of the magnetic field being measured. The PCB array production was conducted at CERN, in collaboration with the EP-DT-EF section. The coils were realized by starting on a layer and winding a certain number of turns inwards before proceeding to wind outwards on the subsequent layer. The adopted design uses plated VIAs, i.e. metallic holes drilled in the compressed stack of layers, to connect the PCB layers into series. The PCB layers have the same nominal surface area, and the pads are placed in close proximity to minimize the spurious surface of wires between them. Figure 5.2 displays a picture of the PCB coil array that was produced, as well as the radial arrangement schematic for the five coils on the PCB array, inside the bore of a quadrupole magnet.

The design parameters for the PCB array are listed in Table 5.1, achieved through aggressive optimization of the production process. The PCB array magnetometer design characteristics are listed in Table 5.2. In particular, the trace-to-trace separation and trace width were set to 50 μm, which is more aggressive than the usual conservative value of 100 μm, to maximize the number of turns per layer. To further increase the maximum achievable coil area, the proposed design 32 layers (single layer technology), with 8 turn on each.

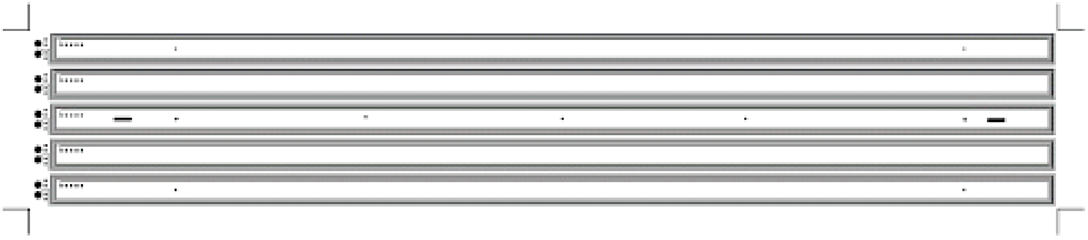

Fig. 5.1 The PCB array magnetometer single layer schematic, with five identical coils in radial configuration; each layer has eight turns [46]. The drawing is not to scale.

Table 5.1 Design parameters of the PCB magnetometer [46].

PCB design parameters	**Value**
PCB width	25.5 mm
PCB total length	620 mm
PCB thickness	3.2 mm
Array design parameters	**Value**
Array width	25 mm
Array length	601.45 mm
Total number of coils	5
Coil design parameters	**Value**
Coil inner length	600.25 mm
Coil inner width	3.5 mm
Coil design area	0.5757 m^2
Number of laywith	32
Turns per layer	8
Total number of turns	256

Table 5.2 PCB manufacturing parameters [46].

Copper track thickness	12 μm
Copper track width	50 μm
Copper track distance	50 μm
Via diameter	25 μm
Internal pad width	25 μm
External pad width	50 μm
FR-4 sheet thickness	50 μm
Pre-preg sheet thickness	50 μm

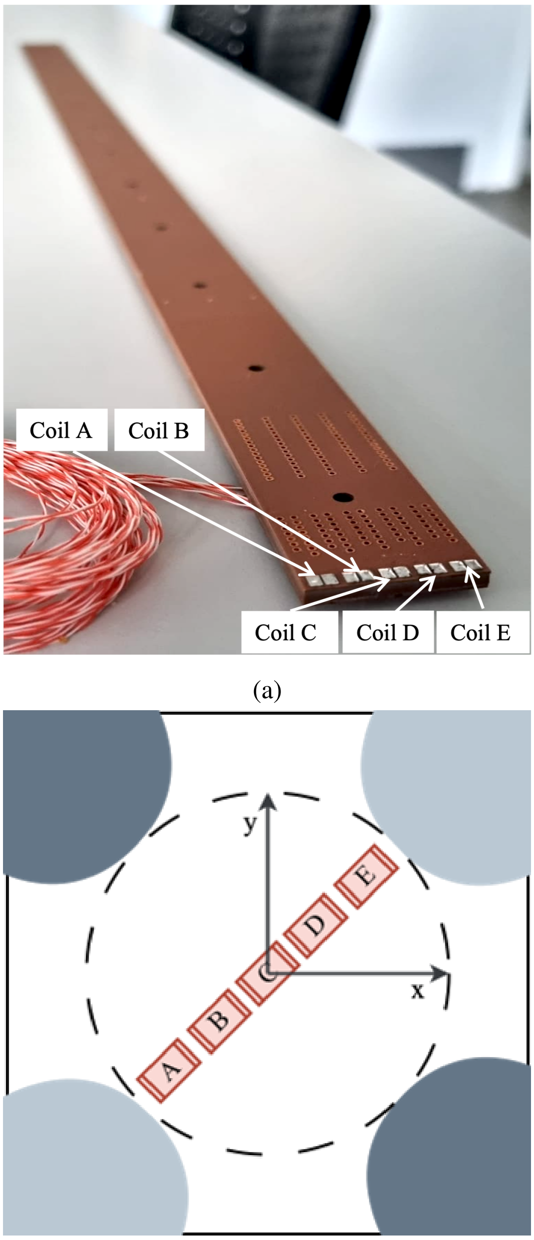

(a)

(b)

Fig. 5.2 The produced PCB magnetometer details. (**a**) The PCB array magnetometer with five identical coils in radial configuration [46] and (**b**) schematic representation of the arrangement of the radial coils in a quadrupole magnet bore.

5.2 Rotating-coil transducer design

The PCB coil magnetometer has to be inserted inside a rotating shaft, in order to allow the rotation along the longitudinal axis of the magnet. During the design phase of the rotating shaft, several factors have been considered, such as the magnet bore diameter and length, the magnetometer dimensions, rotation stiffness, and strength requirements. The proposed rotating shaft has an aspect ratio, defined as $\frac{L^4}{D^2}$, of approximately $\lambda = 268\ m^2$, which is higher than the $\lambda = 173\ m^2$ aspect ratio for the ⌀19 mm probe and $\lambda = 8\ m^2$ for the ⌀8 mm probe, discussed in Section 3.5.

Given the presence of mechanical imperfections in even smaller aspect ratios rotating shaft, the design of the proposed ⌀26 mm rotating-coil system required a novel mechanical asset to be developed. The proposed innovative shaft design involves inserting the PCB-based magnetometer array directly inside a commercial carbon fiber tube, as opposed to using more typical designs that rely on custom tubes or tubular shells based on synthetic sapphire, fabricated on-demand to very tight tolerances, but correspondingly expensive. Carbon fiber is characterized by a high strength-to-weight ratio and resistance to fatigue, it is lightweight, durable, and has excellent mechanical properties, which make the material ideal for use in high-performance applications. Carbon fiber shafts can be manufactured using different methods, such as filament winding or compression molding.

This typology of round tubes is readily available on the market, at a meager cost and in a wide range of lengths and thicknesses. In addition to being non-magnetic, carbon fiber composite has an attractive $\frac{E}{\rho}$ ratio of about $25 \times 10^{12}\mathrm{m}^2\mathrm{s}^{-2}$, which is approximately twice as high as traditionally used fiberglass. Although it is not a perfect insulator, having a resistivity of around 10 $\mu\Omega$m, extensive tests conducted at CERN with tubes diameters up to 100 mm and rotational speeds up to 10 rev/s, have shown no impact of eddy currents on the accuracy of the measured harmonics [68]. The observed dimensional consistency of the units chosen is ⌀26 ± 0.05 mm over a batch of 5 units. The use of carbon fiber shafts in rotating coil systems improves the performance and efficiency of the system while reducing its weight, cost, and maintenance needs.

In the first prototype version of the rotating coil measurement system, all connection and positioning pieces were 3D-printed using Accura 25® plastic. Accura 25® is a resin-based plastic, commonly used in 3D printing for applications that require good dimensional stability, making it a good choice for applications such as prototyping, tooling, and small-scale production. With the 3D technology, connection heads and spacer dimensions were easily modified to adapt perfectly to the final thickness of the PCB magnetometer. This ensured a snug and secure fit for the PCB array within the cylindrical shaft, preventing any unwanted movement or vibration during rotation. The 3D printing flexibility allowed for fast and cost-effective design modifications and reproducibility, quickly iterating the process to improve system design as needed. Semi-cylindrical 3D printed spacers were used to install the PCB at the center of the tube, as shown in the 3D view in Fig. 5.3a, and two connection heads were installed at the extremities of the tube, as shown in Fig. 5.3b. The PCB coil array, equipped with connection heads and spacers, and the final assembled $\varnothing$26 mm shaft are shown in Fig. 5.4

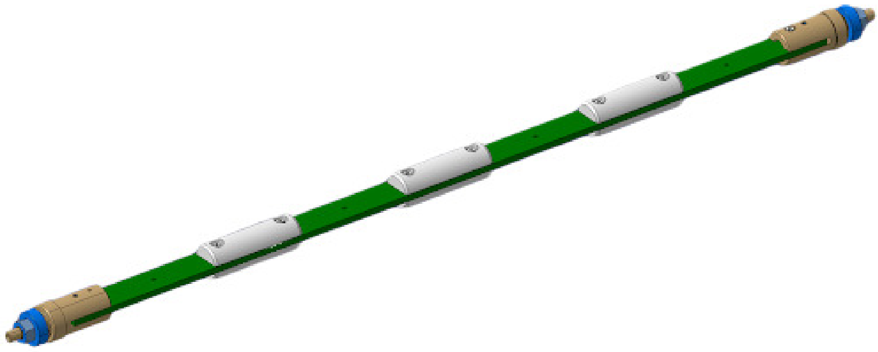

(a)

(b)

Fig. 5.3 The mechanical design for PCB array magnetometer assembly inside the rotating shaft. (**a**) PCB array connection head and spacer design for shaft mounting and (**b**) Carbon fiber external shaft housing the PCB array [46].

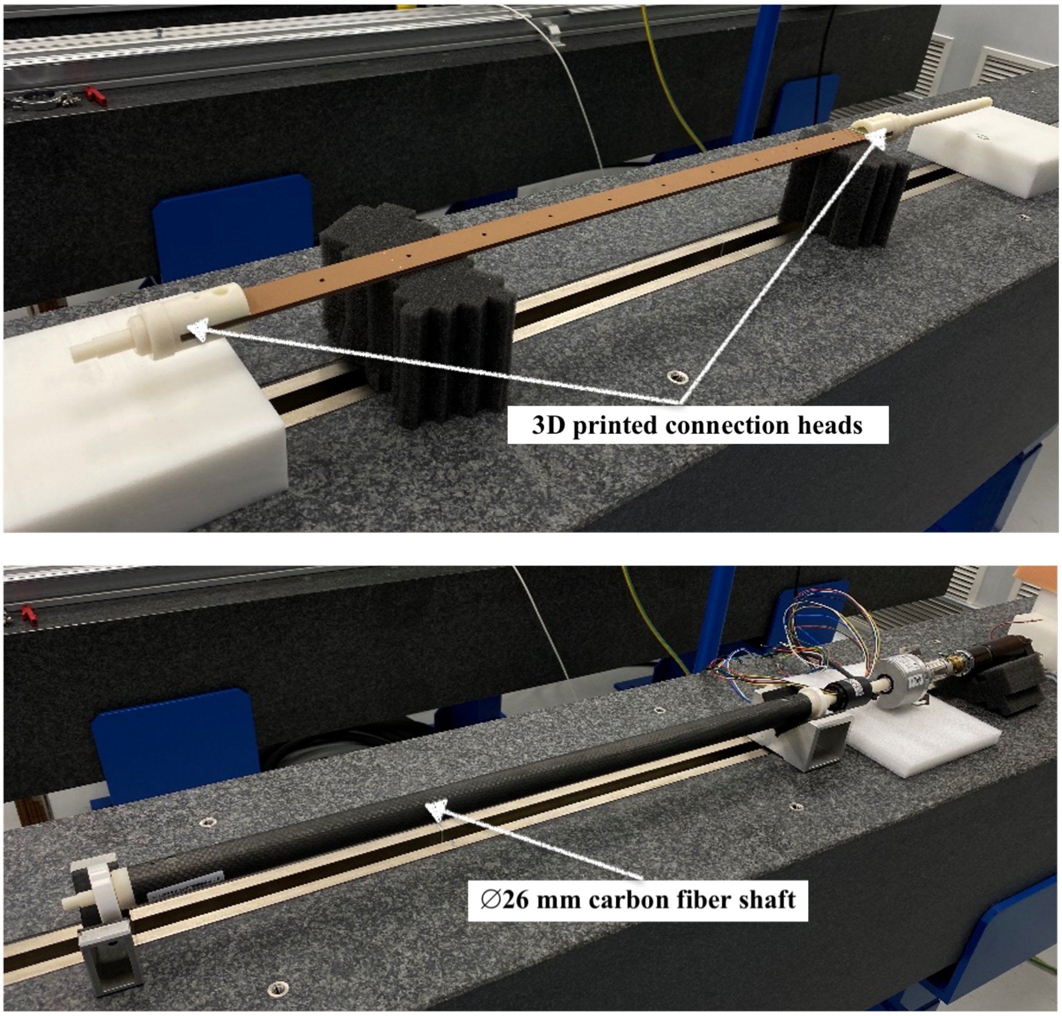

Fig. 5.4 PCB array magnetometer equipped with 3D printed connections heads to be mounted in the ⌀26 mm carbon fiber shaft.

An attentive inspection of the Accura 25® printed pieces has shown slow deterioration of the plastic. Some stress tests, performed on the assembled system simulating the presence of friction presence and eccentricity, have confirmed the high probability of fractures in the material and an alternative was studied for the second version of the Rotating coil system.
Bluestone® is another type of resin-based plastic that is commonly used in 3D printing. It has similar properties to Accura 25®, but with some key differences. Bluestone® is generally harder and more rigid than Accura 25®, which makes it a good choice for applications that require high strength and durability.
If high accuracy and dimensional stability are requested, Accura 25® may be the better choice. If high strength and durability are, Bluestone® may be the better choice. The material choice depends on several factors, including the specific application, the desired properties of the final product, and the available 3D printing technology. Overall, the use of 3D printing technology has played a significant role in the design and production of the rotating coil system, enabling fast and cost-effective design modifications and ensuring accurate positioning of the PCB coil within the cylindrical shaft.

5.3 Harmonic compensation technique

The number of coils in the PCB array depends on the compensation scheme necessary for the magnet to be tested, and it was chosen during the design phase.
Mechanical imperfections in the assembly of a rotating coil system can introduce unwanted harmonic components into the measured signal. These imperfections can include misalignments, deviations from ideal geometry, and variations in coil sensitivity. Similarly, rotation errors such as vibrations and torsion can also introduce additional harmonic components into the coil output signal [74]. These errors are particularly problematic in high-precision applications, where even small deviations from ideal rotation can have significant effects on the measured signal. To address this issue, the compensation or *bucking* [58], technique was employed.
Compensation of the first two components of a quadrupolar magnetic field, namely the dipole and quadrupole terms, is crucial in achieving accurate measurements of the harmonic content. Two typologies of compensation technique can be employed: (i) analog compensation, if the coils are physically connected in series or series

opposition using hard-wired connections; (ii) digital compensation, if all coil signals from the PCB array are acquired individually and then compensated numerically.
For the analog compensation technique, the effectiveness of compensation depends critically on the manufacturing quality of the coils. In particular, for arrays with coils of equal nominal surface, tolerance should not exceed a few tens of ppm. Common mode perturbations are rejected by analog compensation, thus providing a higher signal-to-noise ratio.
In the digital bucking technique, the simultaneous availability of all coils for parallel acquisition provides the additional possibility of carrying out the compensation numerically, at the post-processing stage. In this case, a very high degree of flexibility in the correction of minor systematic geometrical was achieved. In the digital bucking configuration, adopted in the proposed PCB-based magnetometer shown in Figure 5.2a, signals from multiple coils were acquired individually by a DAQ system and then digitally combined in a linear combination that cancels out sensitivity to certain field components.

The nominal coil sensitivity factors are expressed in Eq. 4.15. Assuming that all coils are uniformly radially spaced, have identical geometry, including width d, length l, number of turns N, and coil area $A = Nld$, the ideal sensitivity factors can be practically assessed from coil geometrical parameters, i.e. the coil length L, width d, and average radius w, using the formulae in Table 5.3, where k_n sensitivity factors are reported for each coil in the PCB array, for harmonic order from 1 to 6. Real individual coil sensitivity coefficients k_n are calculated as a first approximation, using the formulae given in Table 5.3 and the calibrated values of the effective areas and widths.
For quadrupoles field characterization applications, compensation for the dipole and quadrupole components of the magnetic field is achieved by ensuring that the sensitivity to the first and second-order harmonic components are zeroed out through a proper linear combination of each coil sensitivity factor of the same order. By varying the weights, different linear combinations can be formed from the same set of sensitivity coefficients.
The expression for a general linear combination H_l is shown in Eq. 5.1. The linear combination coefficient $k_{n,c}$ corresponds to the sensitivity coefficient of order $n = 1...6$ related to coil $c = A,B,C,D,E$. The liner combinations weights, $w_{l,A}.....w_{l,E}$, with $l = 1..7$ identifying a particular weight set, are reported in Ta-

Table 5.3 Sensitivity coefficients from coil geometric parameters

Sensitivity factor	$Coil_A$	$Coil_B$	$Coil_C$	$Coil_D$	$Coil_E$
k_1	A	A	A	A	A
k_2	$-2Aw$	$-Aw$	0	Aw	$2Aw$
k_3	$\frac{49}{12}Aw^2$	$\frac{13}{12}Aw^2$	$\frac{1}{12}Aw^2$	$\frac{13}{12}Aw^2$	$\frac{49}{12}Aw^2$
k_4	$-\frac{17}{2}Aw^3$	$-\frac{5}{4}Aw^3$	0	$\frac{5}{4}Aw^3$	$-\frac{17}{2}Aw^3$
k_5	$\frac{1441}{80}Aw^4$	$\frac{121}{80}Aw^4$	$\frac{1}{80}Aw^4$	$\frac{121}{80}Aw^4$	$\frac{1441}{80}Aw^4$
k_6	$-\frac{931}{24}Aw^5$	$-\frac{91}{48}Aw^5$	0	$\frac{91}{48}Aw^5$	$\frac{931}{24}Aw^5$

ble 5.3 and the assessment of coil sensitivity factors k_n^* as the outcome of reported linear combinations is shown in Table 5.5.

$$H_l : w_{l,A}k_{n,A} + w_{l,B}k_{n,B} + w_{l,C}k_{n,C} + w_{l,D}k_{n,D} + w_{l,E}k_{n,E} \tag{5.1}$$

Table 5.4 Liner combinations weights.

Linear combination	w_A	w_B	w_C	w_D	w_E
H_1	0	-1	1	1	-1
H_2	1	-1	-1	1	0
H_3	4	-6	1	0	1
H_4	5	-7	0	1	1
H_5	3	-5	1	1	0
H_6	$\frac{5}{48}$	$-\frac{17}{24}$	0	$\frac{17}{24}$	$-\frac{5}{48}$
H_7	$\frac{3}{640}$	$-\frac{29}{480}$	$\frac{1067}{960}$	$-\frac{29}{480}$	$\frac{3}{640}$

Table 5.5 Sensitivity coefficients obtained from compensation.

	H_1	H_2	H_3	H_4	H_5	H_6	H_7
k_1^*	0	0	0	0	0	0	A
k_2^*	0	0	0	0	0	Aw	0
k_3^*	$-4Aw^2$	$4Aw^2$	$14Aw^2$	$18Aw^2$	$8Aw^2$	0	0
k_4^*	$-6Aw^2$	$-6Aw^2$	$-18Aw^2$	$-24Aw^2$	$-18Aw^2$	0	0
k_5^*	$-18Aw^2$	$18Aw^2$	$81Aw^2$	$99Aw^2$	$48Aw^2$	0	0
k_6^*	$-35Aw^2$	$-35Aw^2$	$-105Aw^2$	$-140Aw^2$	$-105Aw^2$	0	0

As can be observed from the first two rows in Table 5.5, the first five bucking combinations, H_1 to H_5, effectively eliminate sensitivity to dipole and quadrupole components. Each linear combination excludes one coil to improve immunity to mechanical imperfections, as notable in Tab 5.3. Additionally, each coil is excluded in turn, facilitating the identification of faulty coils that can be replaced with spares. It is important to note that the ordering of the weights in the linear combinations can be reversed due to the symmetry of the array.

The first two linear combinations, H_1 to H_2, can be implemented using a simple series connection and provide some degree of electrical immunity against common mode perturbations. Linear combinations H_3 to H_5 can only be practically implemented numerically in the post-processing phase. They represent an example of a three degrees-of-freedom solution space, obtained by imposing unit weights on two of the coils. The last two combinations, H_6 and H_7, only retain the dipole and quadrupole components and can replace the traditional method of deriving these harmonics from the absolute coil. They should be respectively used for calculating the main field strength and magnetic axis offset. The proposed linear combinations demonstrate the benefits of digital compensation, such as the ability to exclude a faulty coil or use it as a spare. Furthermore, the symmetry of the PCB array magnetometer design allows for the reversal of the weights' ordering.

Chapter 6

Rotating Coil Test Bench for Magnet Characterization

This chapter describes all the hardware and software components of the proposed rotating coil measurement system.

6.1 Rotating coil data acquisition system

Rotating coil systems for magnetic measurement are usually equipped with one or more FDIs[57]. As an example, in [81] a single FDI is used for absolute single coil signals, another for quadrupole and dipole compensated signals, and one for gradient coil signals. The FDIs acquire the coil voltages using an 18 bit SAR ADC. The input voltage is numerically integrated by a DSP, using the trapezoidal integration algorithm. The integrator has a built-in PGA that allows amplification or attenuation of the signal to fit into the ADC input range and the gain can be adjusted between 0.1 and 100.

FDI's main advantage includes the reduction of the output data size by adopting a hardware approach for voltage integration, performed in real-time, and recording only integrated values. The need for frequent calibration is reduced, increasing immunity to drift and noise, and gain can be easily adjusted being beneficial for signals with varying amplitudes. However, there are also some limitations related to FDI usage. One major limitation is the possibility of introducing noise and errors due to sampling rate limitations and quantization effects. Additionally, the integration can be affected by non-linearities and time-variant effects, which can introduce errors in the measurements. The implementation of digital integrators can be complex, requiring advanced knowledge of signal processing and programming. Moreover, FDIs may require higher sampling rates and processing power, which can limit the scalability of the system and increase the hardware and computational costs.

The proposed rotating coil measurement design introduces a data acquisition device, designed to be compact and portable, to replace FDI functionalities. During the selection process of a commercially available DAQ device, a range of parameters and specifications were taken into consideration, for both analog and digital acquisition and output generation. The analog acquisition required simultaneous acquisition and conversion of analog inputs, high input impedance to minimize loading effects on the signal source, and sufficient resolution and sampling frequency. For digital acquisition, the requirements were a sufficient number of digital input and output channels to acquire encoder signals and control the motion unit. The input/output impedance needed to match the signal source or load, and the sampling rate needed to resolve the frequency range of the acquired TTL signals. These specifications were crucial to ensure accurate and reliable acquisition and control of digital signals. Usually commercial DAQ systems include SAR or $\Sigma\Delta$ ADCs. To characterize the quality of both typology of ADC, a simulation can be conducted varying the ADC number of bits and sampling frequency and evaluating the effect on SQNR performance metric. The simulation process model used is based on a digital representation of an ideal harmonic signal, which is described by Eq. 6.1. Specifically, the equation represents the ideal harmonic signal as a function of time, where $A(f)$ is the amplitude of the signal at frequency f and t is time. The signal is a sine wave with frequency of $2\pi f$ and amplitude of $A(f)/2$. The function $n(f)$ in Eq. 6.1 represents the number of harmonic components present in the signal at frequency f. As the frequency of the harmonic components increases, their amplitude decreases as $1/n^3(f)$, as shown in Eq. 6.2. This means that the higher the frequency of the harmonic component, the less it contributes to the overall signal.

$$y(t) = \frac{A(f)}{2}\sin(2\pi f t) \tag{6.1}$$

$$A(f) = \frac{1}{n^3(f)} \tag{6.2}$$

Considering the sampling frequency F_s and the number of acquired samples N_s, the sampling step is given by $\Delta t_s = \frac{1}{F_s}$, and the result of signal sampling is a set of discrete signal values $y_k = y_n(k\Delta t_s)$, for k= 0,1,...N_s. The analog signal is then quantized into a digital representation by assigning a binary code to each sample. The number of bits used for quantization determines the resolution of the digital representation. In the simpler case of a SAR ADC, the result of successive approximations of the discrete values during the quantization process is given in Eq. 6.3.

$$y_{q,k} = \frac{\lfloor y_k + 1 \rfloor 2^{m-1}}{2^{m-1}} - \frac{2^{m-1}}{2^m} \tag{6.3}$$

The quantization noise appears as an additive term, with zero mean and a variance of σ_N^2, uniformly distributed in the frequency range of interest, as reported in Eq. 6.4. The resulting signal affected by noise is given by Eq 6.5. White noise affects all frequencies equally, and its impact on the signal power density spectrum can be observed in Fig. 6.1. The spectrum displays a noise floor that reduces the energy in the main frequency bin of the sinusoidal wave.

$$\varepsilon = \mathscr{U}(0, \sigma_N^2) \tag{6.4}$$

$$y_n(t) = y(t) + \varepsilon \tag{6.5}$$

The magnitude of the quantization noise depends on the number of bits used for quantization, i.e. smaller quantization intervals resulting in lower quantization noise. The quantization intervals represent the accuracy of the ADC's conversion process and are used to determine some performance metrics, in particular, a higher number of bits and smaller quantization intervals can lead to a higher SQNR. To simulate ADC conversion performance, the SQNR has been computed varying the sampling frequency, in the absence of oversampling, according to Eq. 6.6, and in case of oversampling, according to Eq. 6.7. For both equations, m is the ADC number of bits and F_s is the maximum signal frequency.

$$SQNR = 6.02\text{m} + 1.76\text{dB} \tag{6.6}$$

$$SQNR = 10\log_{10}\frac{F_s}{2F_{max}} + 6.02\text{m} + 1.76\text{dB} \tag{6.7}$$

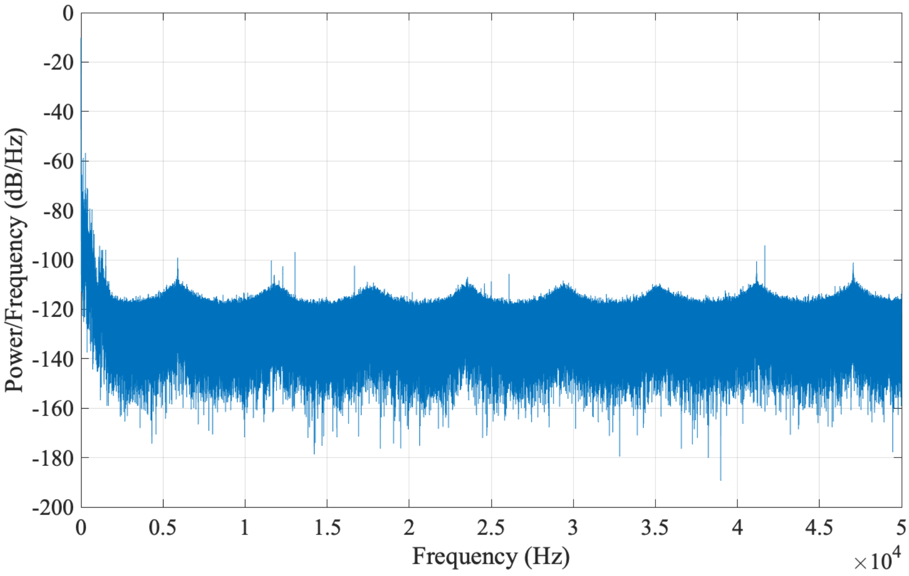

Fig. 6.1 Power spectrum density of the absolute coil output voltage.

Figure 6.2a demonstrates the simulation of a SAR ADC behavior while varying both the number of bits and sampling frequencies. According to Eq 6.6, the SQNR increases linearly with the ADC number of bits, while remaining invariant with respect to the sampling frequency. For a ΣΔ ADC, assuming a maximum signal frequency of 24 Hz and sampling frequency of 48 Hz, no oversampling is taking place, according to the SQNR expression shown in Eq. 6.7. In Fig 6.2b, in case of oversampling, by fixing the number of bits, the SQNR enhances with the increase of the sampling frequency. With a sampling frequency of 200k Hz, the oversampling ratio is nearly 4000, and the SQNR improvement is about 36 dB if compared to the SQNR at the Nyquist frequency. The increment in SQNR corresponds to additional 6 bits of resolution. Moreover, increasing the number of bits to 24, the SQNR exhibits an increment of 85 dB, which is equivalent to adding 14 bits of resolution at 200k Hz of sampling frequency.

Increasing the ADC number of bits can provide better resolution and a higher SQNR, which can result in more accurate measurements. However, this also requires a larger dynamic range and can increase the cost and complexity of the system. On the other hand, increasing the sampling frequency can allow for better capture of high-frequency signals and can improve the accuracy of time-domain measurements. However, this can also increase the amount of data that needs to be processed and stored and can result in higher power consumption and heat dissipation. A trade-off between these factors and other considerations, such as cost and power consumption, has been reached in order to select an appropriate ADC for the given application.

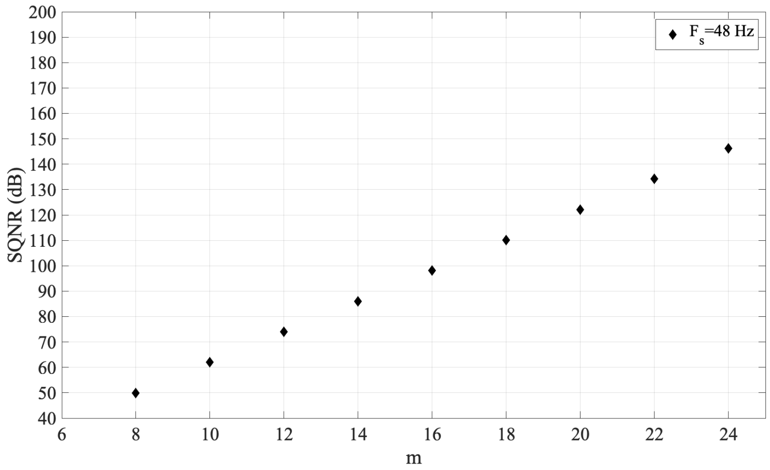

(a)

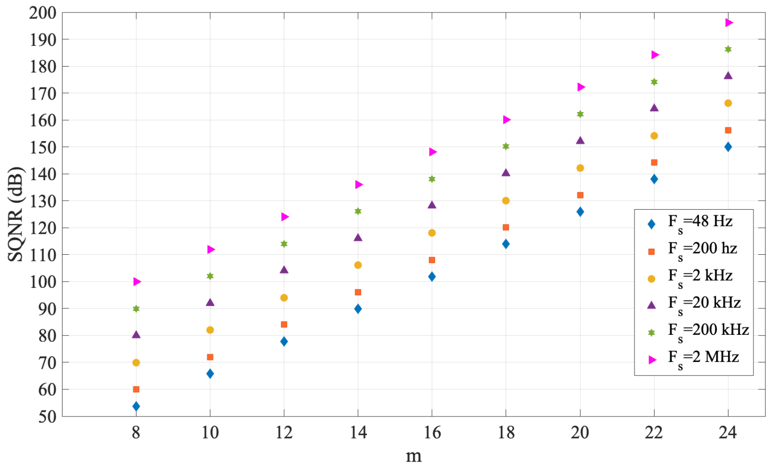

(b)

Fig. 6.2 ADC performances simulation(**a**) The SQNR estimated at Nyquist frequency and (**b**) the SQNR is estimated when oversampling is applied, as a function of sampling frequency and number of bits..

For the proposed rotating coil measurement system, the selection of the acquisition system was determined by good accuracy requirements for field reconstruction and input signal characteristics, as well as the primary objective of designing a simplified and compact system, avoiding FDIs use and limiting costs. The acquisition card had to satisfy the following minimum specifications:

- At least six analog input channels, operating simultaneously.
- The ADC sampling frequency should be at least 200 kS/s.
- At least 6 digital channels for the encoder reading, with a sample clock frequency of at least 1M Hz, to enable accurate identification of each line transition of state.
- An ADC converter with a minimum resolution of 12 bits.
- An internal time-base of 20 MHz to ensure a time resolution of 50 ns.

The data acquisition system chosen for the proposed ⌀26 mm rotating coil system is the USB-6366 [82] DAQ from NI, equipped with a 16-bit SAR ADC, eight differential analog inputs, 24 digital I/O ports, and a maximum sample rate of 2 MS/s per channel. The ADC has a programmable input voltage range and the input impedance is 1 $M\Omega$. The DAQ noise floor is around 50 $\frac{nV}{\sqrt{Hz}}$, the ideal SQNR is 98.09 dB and ENOB is 15 bits. Based on these specifications, we can expect the device to provide high-resolution measurements with low quantization noise, especially at low frequencies. However, the quantization error may increase at higher frequencies, especially if the input signal exceeds the Nyquist frequency of the ADC. For this application, as the quadrupole magnet's field harmonics of interest typically do not go above $n = 6$ (dodecapole), the useful signal bandwidth is limited to 24 Hz at the maximum rotation speed of 2 rev/s. Therefore, to avoid aliasing, a sampling frequency of 200 kS/s has been selected.

6.2 Rotating-coil motion system design

The assembled rotating shaft uses a commercial sensor-less DC brush-less motor, Maxon EC 45 Flat [83]. It offers high torque and speed capabilities while maintaining low vibration and noise levels. The motor's flat design allows for easy integration into space-constrained applications, such as the rotating shaft in the magnetic measurement system. Control over the speed and position of the motor is achieved through the use of electronic commutation, which eliminates the need for mechanical brushes and allows for smoother operation at high speeds.

In the proposed rotating coil measurement system, the motor is used to rotate the shaft in both directions, which helps to reduce systematic errors in measurements by averaging the results obtained in each direction. This is a common technique used in precision measurements to eliminate the effects of asymmetric factors, such as bearing friction and non-uniform magnetic fields. In order to regulate the speed and direction of the motor, the programmable power supply and the DAQ digital outputs are used.

During rotation, a programmable optical high-resolution incremental encoder, Baumer EIL580P-T [84], provides information on the angular shaft position. The EIL580P-T features a programmable resolution of up to 10,000 pulses per revolution and supports both TTL and RS422 signal outputs. The encoder has a maximum of 65,536 optical pulses per revolution, providing a resolution of 48 μrad, and is built to withstand harsh industrial environments with its IP67-rated housing. Its compact design and easy mounting make it a popular choice for applications with limited space. The optical encoder converts the rotational movement of the shaft into an electrical signal. It consists of a light source, a patterned disc, and a photodetector. The patterned disc has alternating opaque and transparent segments that pass between the light source and the photodetector as the disc rotates. As each segment passes between the light source and the photodetector, the light intensity changes, causing the photodetector to produce a series of pulses in response to the pattern on the disc. In particular, an optical encoder with a TTL output produces a square wave signal that is compatible with the selected DAQ system. The TTL output of the encoder produces square-wave signals with a specific voltage range of 0 to 5 volts.

The Baumer EIL580P-T encoder has three output channels: A, B, and Z. Channels A and B produce quadrature signals, which are 90 degrees out of phase with each other and are used to determine the shaft position and direction of rotation. Channel Z produces a single pulse per rotation, which is used as a reference or index signal to synchronize the position measurements. The frequency of the square wave is proportional to the rotational speed of the shaft, while the number of pulses per revolution determines the resolution of the encoder and is set by the user through a dedicated stand-alone programmer.

To transmit coil voltage signals to the acquisition system during the continuous rotation of the shaft, a through-hole slip-ring is used. A slip-ring, also known as a rotary electrical interface or electrical rotary joint, is an electro-mechanical device used to transmit power, signals, or data between a stationary and a rotating part of a system. The stationary part consists of a set of brushes making contact with a rotating metal ring on the rotating section. The metal rings are made of a conductive material such as copper and are insulated from each other to prevent short circuits. As the shaft rotates, the metal rings make contact with the stationary brushes or contacts, allowing the voltage signals from the coils to be transmitted to the acquisition system without interruption. The described hardware components are visible in Fig. 6.3a, a focus on the miniaturized connector between the PCB Array magnetometer and the slip ring is shown in Fig. 6.3b, and the control diagram of the proposed rotating coil measurement system is schematized in Figure 6.4. The motion unit and rotating shaft are supported by platforms and stages realized from aluminum plates, allowing for precise and customized adjustments to be made to the system as needed. A 3D view of the proposed vertical support and base is shown in Fig. 6.5, where adjustable support platforms and vertical V-shaped stages were designed to suspend the entire rotating system in the magnet aperture. This is critical for ensuring that the shaft rotation axis is in the mechanical center of the quadrupole magnet.

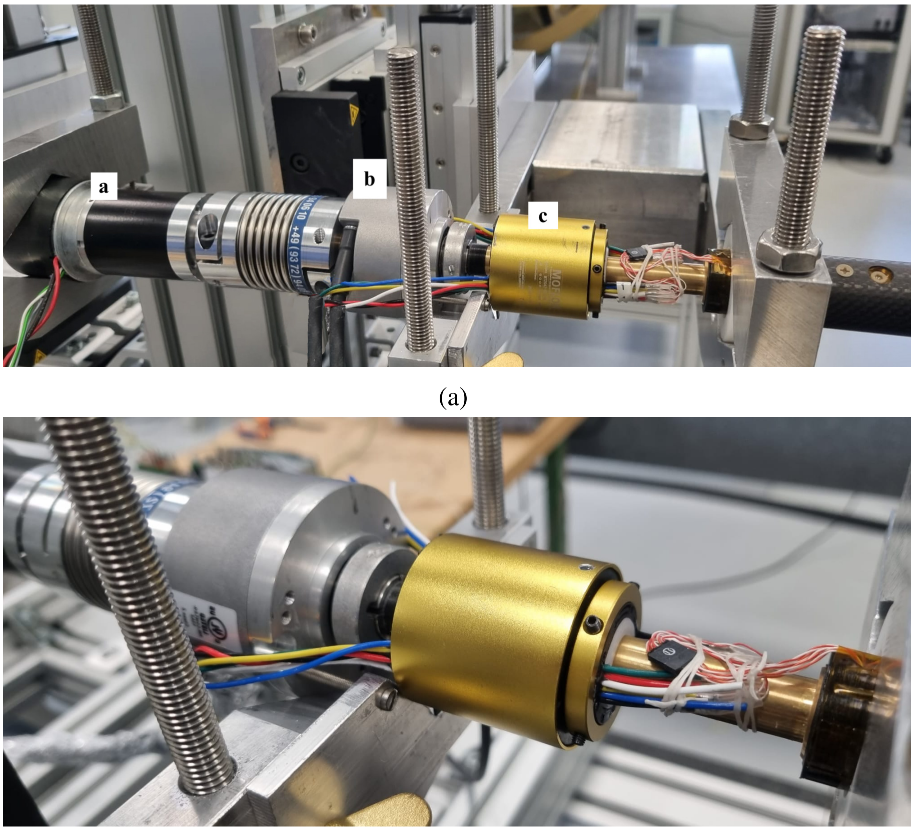

(a)

(b)

Fig. 6.3 Motion unit components for the proposed $\varnothing$26 mm rotating coil system. (**a**) Maxon EC 45 flat DC motor[a], Baumer optical Encoder and controller[b], Moflon 12 signals slip-ring[c] and (**b**) Miniaturized connector details between the slip-ring and the PCB magnetometer housed by the shaft.

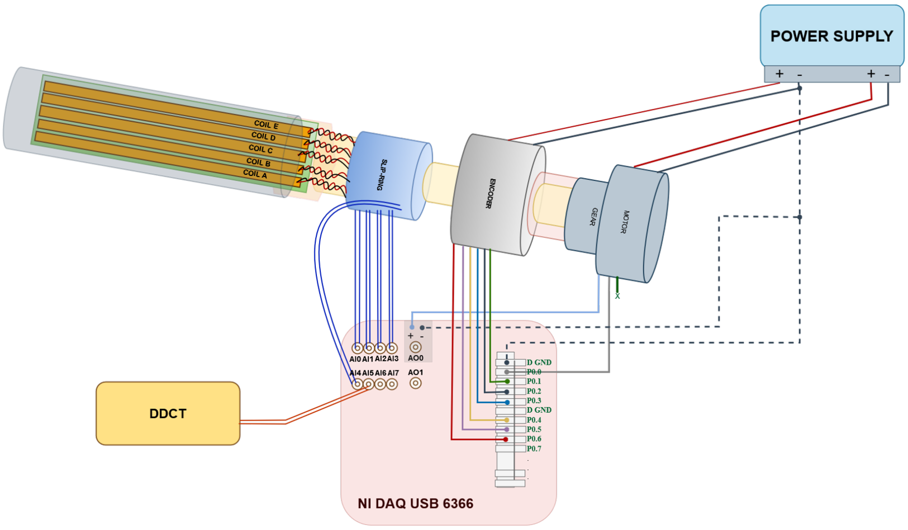

Fig. 6.4 Control diagram for the proposed ⌀26 mm rotating-coil measurement system. A software application allows the user to configure the rotation parameters, start the acquisition of encoder and slip-ring signals, and perform the harmonic analysis.

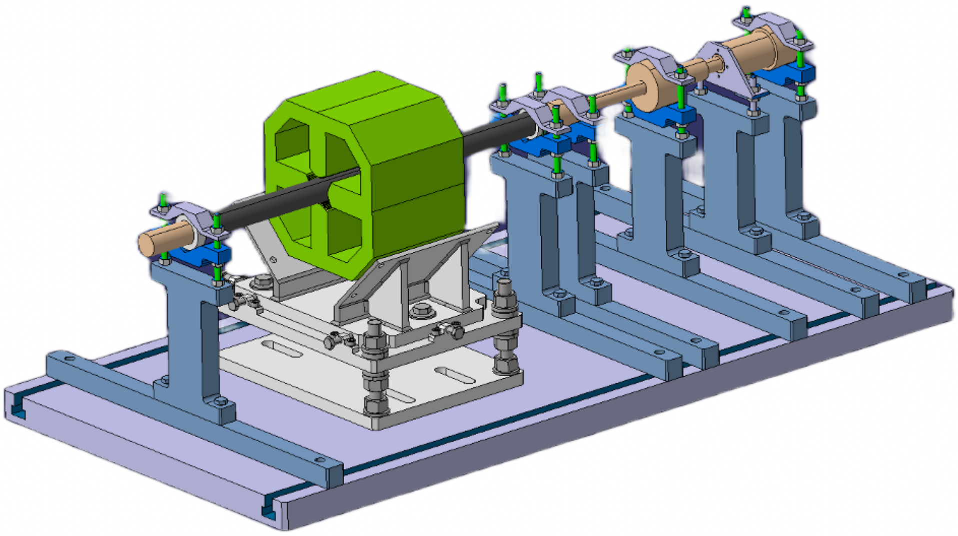

Fig. 6.5 A 3D view of the design measurement bench for rotating coil system alignment in the magnet bore.

6.3 Software design for rotating-coil signal acquisition

The DAQ USB 6366 high-performance acquisition systems, developed by NI, can be easily programmable using the LabVIEW tool. LabVIEW is a development environment for graphical programming based on data-flow programming, extensively used in data acquisition applications, instrument monitoring, and automation. LabVIEW's capability of parallel execution, multiprocessing, and multi-threading makes it a powerful tool, considering also its extensive support for accessing instrumentation hardware. In order to design a LabVIEW acquisition software easy to read, maintain, and document, an event-driven producer-consumer state machine was developed for the acquisition of signals from the rotating coil system. The state machine is designed to efficiently handle the acquisition of signals from multiple analog and digital channels, as well as the control of the rotating coil motion unit.
Running the software, the interface front panel visualized by the user is shown in Fig. 6.6. Most of the cases held by the main VI state machine are dedicated to the measurement configuration in terms of data acquisition channels and properties, device ports, and information necessary for the output log file production. The user is requested to perform the following actions:

- DAQ device selection and ADC input range configuration;
- Analog Input channels selection and configuration;
- Digitl Input port selection and configuration;
- Rotation speed, direction, and number of rotation configuration;
- Calibration option selection to eventually calibrate the coil rotation radius *in-situ*.
- Output file location selection;

The producer-consumer architecture was implemented for signal acquisition and data manipulation to be performed simultaneously, improving the overall efficiency and accuracy of the system. In the producer loop, a hardware-triggered data acquisition has been implemented with the main goal of starting analog and digital tasks simultaneously. In particular, three DAQmx tasks were created: (i) analog channels read task, to acquire the coil signals, (ii) digital channels read task, to acquire the

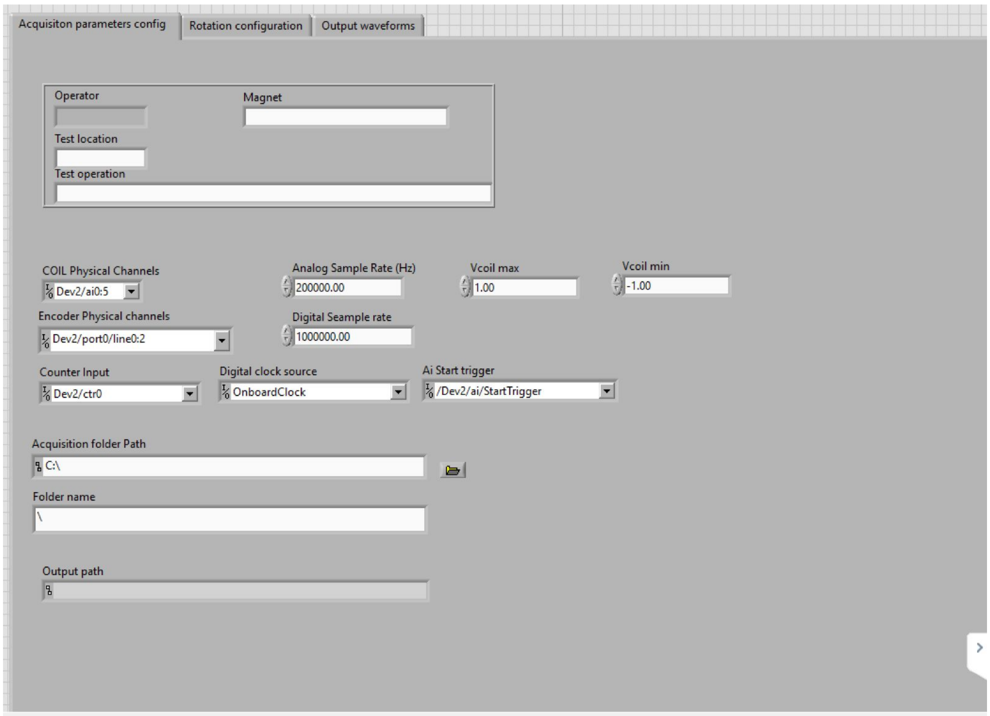

COIL Physical Channels
Dev2/ai0:5

Analog Sample Rate (Hz)
200000.00

Vcoil max
1.00

Vcoil min
-1.00

Encoder Physical channels
Dev2/port0/line0:2

Digital Seample rate
1000000.00

Counter Input
Dev2/ctr0

Digital clock source
OnboardClock

Ai Start trigger
/Dev2/ai/StartTrigger

Acquisition folder Path
C:\

Folder name
\

Output path

Fig. 6.6 LabVIEW user interface.

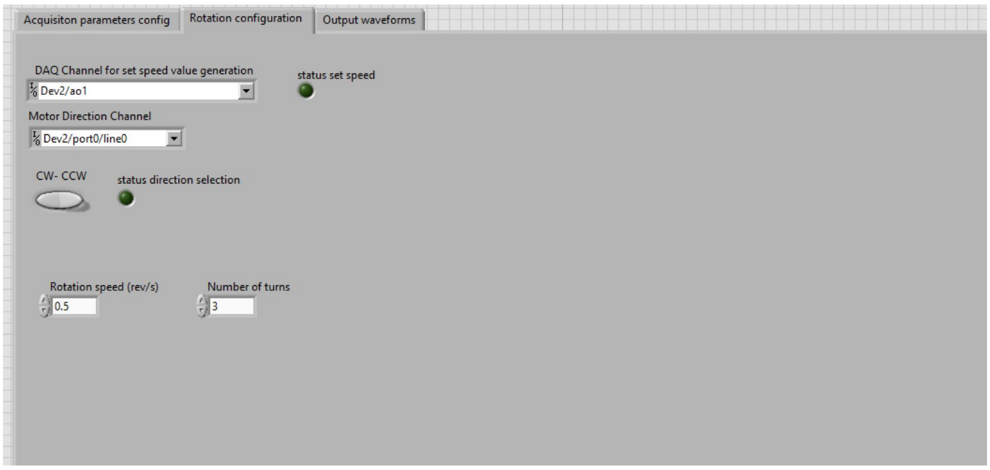

DAQ Channel for set speed value generation
Dev2/ao1

Motor Direction Channel
Dev2/port0/line0

Rotation speed (rev/s)
0.5

Number of turns
3

Fig. 6.7 LabVIEW user interface focus on motor control parameter setting.

encoder digital lines, and (iii) counter output task to generate the clock source for the digital task.

The reference time-base for the analog signal acquisition is the onboard clock. When the DAQmx Start Analog Input task is executed, the card generates a digital pulse, which triggers the counter output and, consequently, the digital acquisition. Using a flat sequence, the counter, and digital tasks are started in sequence. By starting the digital task without starting the counter, the digital task is put on hold until it receives its clock, represented by the counter output. Once it starts, all the tasks are executed together.

The event-driven producer-consumer state machine has been successfully tested on the proposed rotating coil system. The system is able to efficiently acquire signals from multiple channels and perform data manipulation in real-time. The user-friendly graphical user interface guides the user through the measurement process, making it easy to configure the system and perform measurements.

The measurement procedure begins with the manual alignment of the shaft within the magnet aperture in correspondence with the mechanical center. Afterward, the magnet is powered and the excitation current is set at the desired level (in the case of an electro-magnet). Once input parameters are set by the user and application is in run mode, the shaft motor is started. The acquisition of the analog and digital signals recording is enabled upon reception of 5 trigger pulses on the reference channel of the encoder, in order to stabilize the shaft rotation speed before saving the acquired signals. A variable number of complete rotations, chosen by the user, usually ten or more, is then saved in a single output file, to allow the averaging of the results to evaluate and suppress random noise components.

6.4 Post-processing software design

As introduced in Sec. 5.3, the absolute signal is used to evaluate the main field component, and the compensated signal is used to evaluate the higher-order harmonics. The absolute voltage is the output of one of the two outermost coils in the array. The compensated voltage, which provides the highest signal level in any field multipole of order $n \leq 2$, is a linear combination of four coil outputs. The proposed system utilizes digital compensation to increase flexibility and correct any small differences between the coils, while also extending the range of possible compensation schemes.

The stored data undergo a post-processing phase, schematically described in Fig. 6.8.

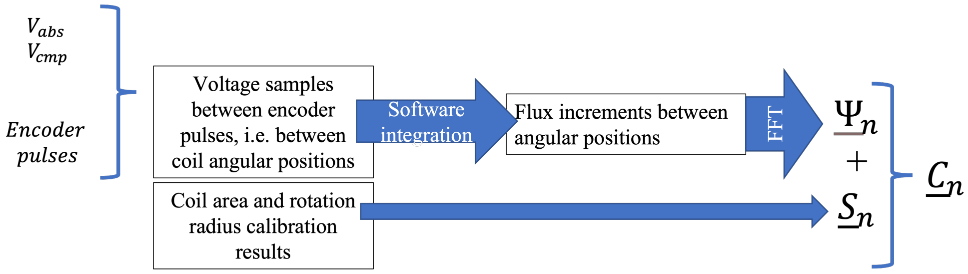

Fig. 6.8 Harmonic Analysis MATLAB script structure

The MATLAB post-processing software includes the following steps [46].

Voltage Integration

The raw voltage signals contain both electrical and mechanical noise components, with the low-frequency noise causing integration drift. To address this issue, the next section focuses on treating the low-frequency noise component. High-frequency noise components are naturally reduced through signal integration to obtain magnetic flux, which is then used to derive magnetic field harmonics. The integration process involves re-parameterizing the signal as a function of angular position, which also eliminates the impact of torsional vibrations. The coil voltages are integrated between consecutive encoder triggers using the trapezoidal rule. However, since the encoder triggers are asynchronous with respect to the ADC time base, the first and last analog samples of each interval are linearly interpolated to ensure proper integration bounds.

Drift Correction

Integration drift is a phenomenon that occurs when a signal is integrated, resulting in the amplification of low-frequency noise components [85]. This causes the integrated voltage signal, which represents the magnetic flux, to have a linear trend in a first-order approximation. To correct for this effect, the remaining integrated flux after a complete shaft rotation is calculated and compensated. Since the flux change over an entire shaft rotation must be zero, any remaining integrated flux can be attributed to drift. If the magnetic field being measured is constant, the output voltage of the five coils is periodic. Due to the low period of the signal (maximum 2 s) and the reasonably stable environment of the acquisition electronics, the voltage offset can be assumed to be constant over a complete revolution. The estimated remaining flux after a complete rotation was a few mV for the absolute signal before correction.

Assessment of the Complex Harmonic Coefficients

The DFTs of the fluxes, which have been integrated and pre-processed, are calculated using the Fast Fourier Transform (FFT) algorithm. The complex coefficients of the magnetic field harmonics are then computed using Eq. 4.17. The values of $\underline{S}_n$ used in this equation are determined from the coil sensitivity coefficients, which are obtained using Eq. 4.15. The calibrated values of the coil area and radius are used in this equation to compute the sensitivity coefficients.

The feed-down phenomenon refers to the generation of spurious field harmonic errors of order $n < m$ when the reference system is translated. In an ideal quadrupole C_2, with a magnetic center coincident with the mechanical center (point O in Figure 4.4a), the magnetic field is zero. However, if the rotating coil is placed off-axis such that the measurement coil frame origin O′ in Figure 4.4b is displaced by Δz from the magnetic center, a dipole component C_1 proportional to the displacement appears. The offset δz can be calculated from the measured harmonics as shown in Eq 6.8, where $\Delta z = \Delta x + i\Delta y$. The measured harmonic coefficients can then be corrected using the expression in Eq. 6.9.

$$\Delta z = -r_0 \frac{C_1}{C_2}, \tag{6.8}$$

$$C_n^{'} = \sum_{k=n}^{\infty} (\frac{(k-1)!}{(n-1)!(k-n)!}) C_k \left(\frac{\Delta z}{r_0}\right)^{k-n}. \tag{6.9}$$

Evaluation of Main Field Module and Phase

The main field module is obtained from the normal and skew components of $C_2^{'}$, as taken from the absolute signal, according to Eq. 6.10, and the main field direction α_2 is obtained from the field phase ϕ_2 as shown in Eq. 6.11.

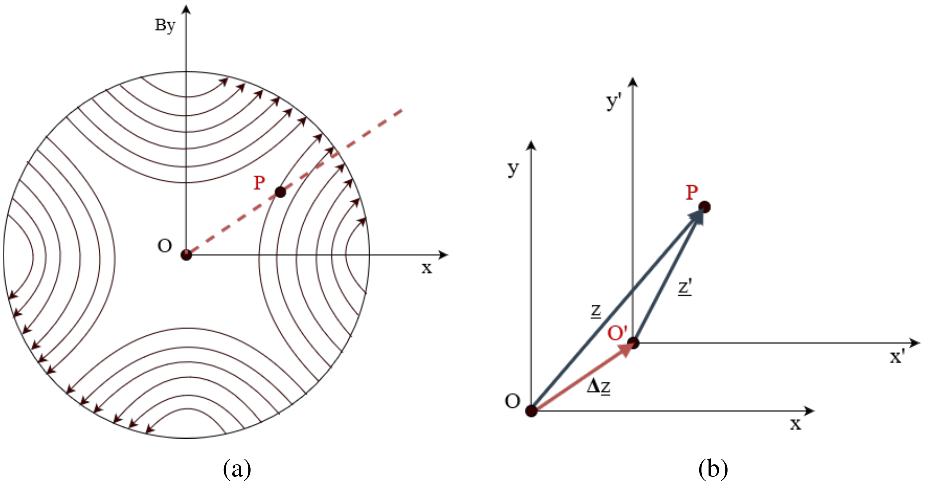

Fig. 6.9 The translation of the reference system in the presence of the feed-down phenomenon. (**a**) Magnetic field lines in a normal quadrupole magnet ($A_2 = 0$). (**b**) The coordinate system with origin in O′ is used for harmonics calculation if the measurement coil rotation axis is displaced by Δz from the magnetic center, marked with O [46].

$$|C_2^{'}| = \sqrt{B_2^{'2} + A_2^{'2}} \tag{6.10}$$

$$\alpha_2 = \frac{\phi_2}{2}. \tag{6.11}$$

Rotation and Normalization

The phase of the harmonic coefficients is based on the position of the encoder index, which is, in principle, arbitrary due to mechanical tolerances. The absolute and compensated harmonic coefficients are rotated such that the measured main field corresponds to the known type of the magnet under test; in our case, this is defined as a normal quadrupole, hence $A_2 = 0$. The measured harmonic coefficients are rotated by the field direction angle $-\alpha_2$ as in Eq. 6.12. The last step of the post-processing is the normalization of the harmonic coefficients with respect to the main field module, according to Eq 6.13.

$$C_n^{''} = B_n^{''} + iA_n{''} = C_n^{'} e^{-in\alpha_2}. \tag{6.12}$$

The last step of the post-processing is the normalization of the harmonic coefficients with respect to the main field module:

$$a_n = 10^4 \frac{{A_n}''}{|C''_2|}, \quad b_n = 10^4 \frac{{B_n}''}{|C''_2|}, \quad c_n = 10^4 \frac{{C_n}''}{|C''_2|}. \tag{6.13}$$

Part III

Experimental results

Chapter 7

Metrological analysis

In this chapter, a metrological analysis, including the electro-mechanical characterization, of the proposed rotating coil system is presented. The importance of calibration and how it affects the accuracy and precision of the measurements is also introduced.

7.1 Magnetic surface calibration

The accuracy of rotating coil magnetometers relies on several factors, with sensitivity factors playing a significant role. Sensitivity factors are primarily dependent on the coil area and rotation radius and these quantities are determined by calibrating against a reference field (for the area) and a field gradient (for the rotation radius). To assess the quality of PCB coil production and detect defects, such as inter-turn short circuits that are challenging to identify through resistance measurements, area calibration was conducted before assembling the magnetometer inside the rotating shaft. On the other hand, the calibration of the rotating radius of each coil on the PCB magnetometer necessitates the final ball bearings to provide the ultimate rotation axis, resulting in the most accurate measurements. Therefore, it should be performed on the fully assembled rotating coil probe.

To calibrate the coil surface, a reference dipole magnet, shown in Fig. 8.1. available at CERN magnetic measurement laboratory, was used. The reference dipole magnetic field strength is 1 T, with a relative spatial uniformity of 200 ppm in the magnetic flux density. The reference field was measured using an NMR magnetometer. The calibration procedure involved flipping the coil inside the reference magnet and integrating the voltage induced by the change in the intercepted flux. The average magnetic field B, measured by NMR along the length of the coil, was used as the reference field value. The voltage, integrated while flipping the coil between time instants t_0 and t_f, was obtained from Faraday's induction, law as in Eq. 7.1. Being $\phi_1 = 0$ and $\phi_2 = \pi$, the magnetic calibrated coil surface A_m was obtained from Eq. 7.2.

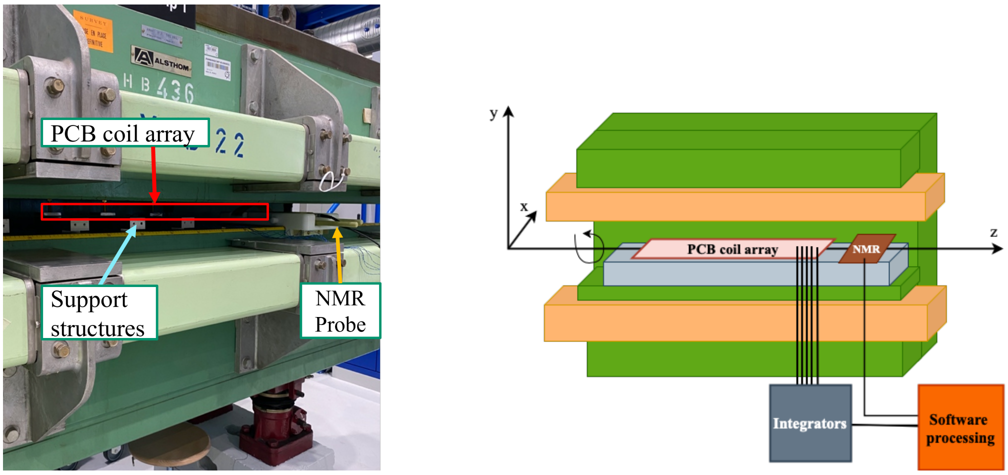

(a) (b)

Fig. 7.1 Magnetic calibration setup: (**a**) Magnetic calibration performed inside a bending reference dipole cycled up to 1 T and (**b**) schematic representation of the magnetic calibration setup. All the calibrations have been performed at the reference magnetic flux density 0.99914 T.

$$\int_{t_0}^{t_f} U(t)\,dt = \int_{t_0}^{t_f} -\frac{d\Phi(t)}{dt} = \Phi(t_0) - \Phi(t_f) = \Delta\Phi(t). \tag{7.1}$$

$$\Delta\Phi(t) = A_m B cos\theta_m - A_m B cos\theta_{m-1} = 2A_m B \tag{7.2}$$

The magnetic area calibration was performed on a batch of 6 PCB arrays. The results are compared to the design coil area A_d and reported in Figure 7.2 only for the selected PCB array to be installed in the rotating shaft, the PCB Array 4.

In Table 7.1 results are reported along with the relative difference $\Delta = \frac{A_d - A_m}{A_d}$. The nominal and calibrated coil areas differ from the design value by approximately 160 ppm RMS, with measurement repeatability as low as 0.6 ppm.

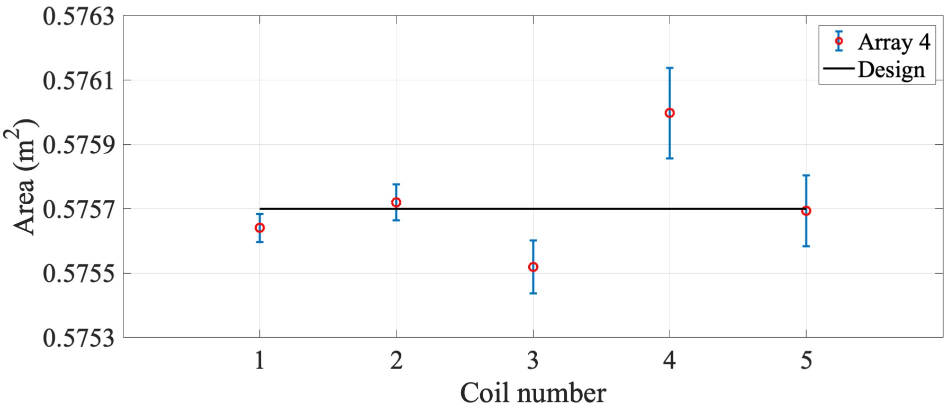

Fig. 7.2 Results for coil surface calibration on PCB Array 4, compared to the area design value.

Table 7.1 Calibration results for coil area in PCB Array 4.

PCB Array 4	Coil A	Coil B	Coil C	Coil D	Coil E
A_d [m^2]	0.57569	0.57569	0.57569	0.57569	0.57569
A_m [m^2]	0.57564	0.57572	0.57552	0.57579	0.57568
Δ [ppm]	86	-52	295	-173	-18

In conclusion, the use of PCB technology in coil production has enabled high control over track positioning, but there are some issues to consider. In Fig. 7.3, it is clear that different coils on different PCB Arrays are missing approximately 0.4 % of their coil area. This is most likely due to a single inter-turn short circuit, which proved difficult to identify even with a four-wire measurement.

The coil surface magnetic calibration was fundamental in discovering the presence of defects in coils production and selecting the only fully working PCB array magnetometer to be installed in the rotating shaft.

7.2 Rotation radius calibration

The coil rotation radii were calibrated directly in the quadrupole magnet to be tested, the BTF7 quadrupole magnet from INFN, which served as a reference. To calibrate the coil radii, knowledge of the field gradient is required. A reference gradient measurement was obtained using an SSW system.

The integrated gradient g over the magnetic length L_m is defined as in Eq. 7.3, where

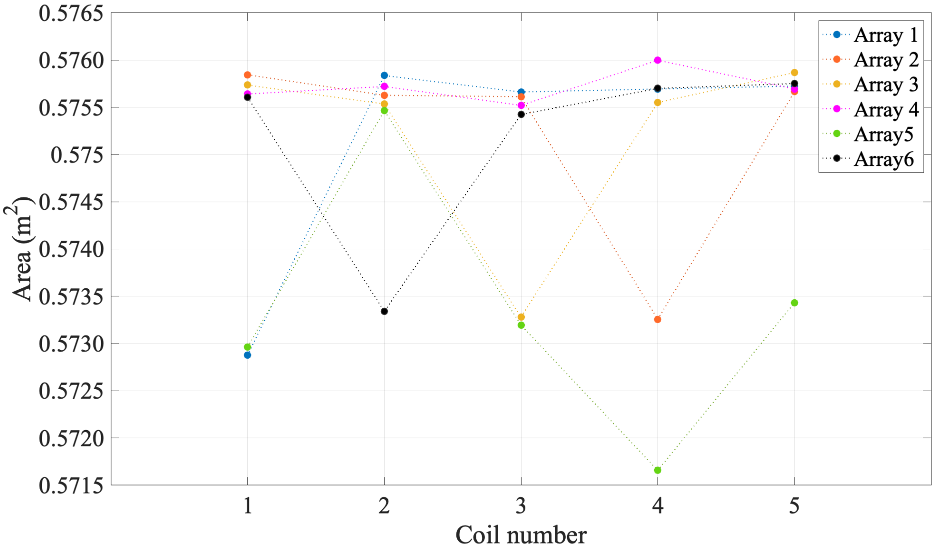

Fig. 7.3 Calibration results in comparison for six different PCB array magnetometers.

G_c is the field gradient measured along the wire displacement, and $G(l)$ is the field gradient as a function of the position. From Eq. 4.15, the sensitivity coefficient $\underline{S}_2$ to the quadrupole component (obtained for $\underline{z}_1 = x_1$ and $\underline{z}_2 = x_2$ in Figure 4.3) is given by Eq. 7.4, where $w = x_2 - x_1$ is the coil width, $r_c = \frac{x_1+x_2}{2}$ is the average radius of the absolute coil winding, and y is the coil's vertical displacement from the PCB array plane.

From Eq. 7.3 and Eq. 7.4 and considering the definition of the gradient as $G = B_2/r_0$, the average coil radius is obtained from expression in Eq. 7.5.

$$g = G_c L_m = \int_{-\infty}^{+\infty} G(l)\, dl \tag{7.3}$$

$$\begin{aligned} S_2 = \frac{NL}{2r_0}[(x_2+iy)^2-(x_1+iy)^2] = \frac{NL}{2r_0}[(x_2^2-x_1^2+i2y(x_2-x_1)] \\ = \frac{NL}{r_0}w(r_c+iy) = \frac{A_c}{r_0}(r_c+iy) \end{aligned} \tag{7.4}$$

.

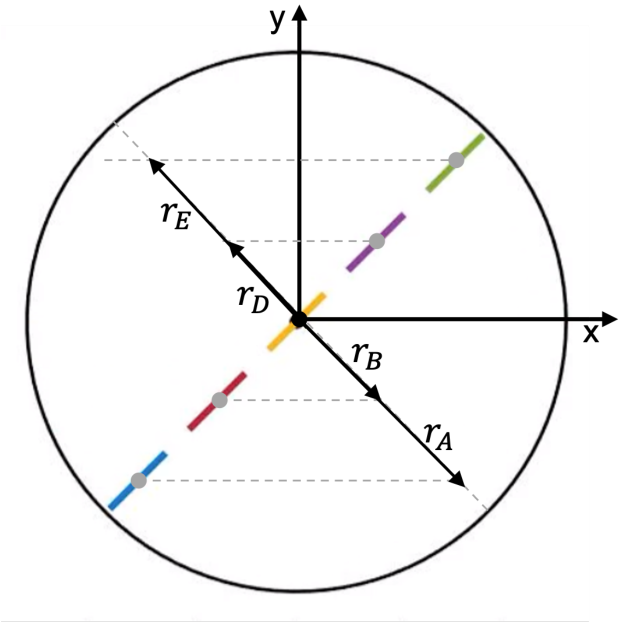

Fig. 7.4 Schematic representation of coil rotation radius in the shaft cross-section.

$$\begin{aligned} r_c &= \mathrm{Re}(\frac{S_2}{Ac} r_0) = \frac{r_0}{A_c} \mathrm{Re}(\frac{\Psi_2}{C_2}) \\ &= \frac{r_0}{A_c} (\frac{\mathrm{Re}(\Psi_2)}{B_2}) = \frac{r_0}{A_c} \frac{\mathrm{Re}(\Psi_2)}{G r_0} = \frac{1}{A_c} \frac{\mathrm{Re}(\Psi_2)}{G} = \frac{L_m}{A_c} \frac{\mathrm{Re}(\Psi_2)}{g} \end{aligned} \tag{7.5}$$

Figure. 7.4 illustrates a schematic representation of the coil rotation radii in the shaft cross-section. Table 7.2 presents the nominal values for the coil rotation radius r_d, the calibrated rotation radius r_c, and the calibrated radius r^* relative to the central coil C, which was used as a reference for each coil on PCB Array 4. The table also shows the difference $\Delta = r_d - r^*$ from the nominal design values, which is in the order of tens of μm.

Table 7.2 Calibration results for PCB Array 4 coil rotation radius [46].

PCB Array 4	Coil A	Coil B	Coil C	Coil D	Coil E
r_d [mm]	9.500	4.750	0	4.750	9.500
r_c [mm]	9.460	4.799	0.028	4.721	9.472
r^* [mm]	9.432	4.772	0	4.750	9.500
Δ [μm]	67.6	21.8	0	0.5	0.0

In conclusion, the calibrated coil radii, denoted as r^* and presented in Table 7.2, are computed with respect to the symmetry axis of the central coil C. These radii exhibit a difference of around 35 μm RMS from the design value, representing a relative error of 0.35% with respect to the outer coil radius. Despite the repeatability of the radius measurement being 0.03%, the poor result can be attributed to Eq.7.5, which combines the errors in both the coil area and the magnetic flux measurements. Additionally, an asymmetry between the calibrated radii on one side of the PCB, specifically for Coils D and E, which are very close to their nominal values, and Coils A and B, which have an error of up to 67 μm, was observed. This asymmetry might be due to a systematic effect in PCB manufacturing, which was investigated further on other PCBs of the same batch.

In conclusion, for achieving a target accuracy of the rotating-coil system measurement in the range of 100 ppm, the nominal values of the geometrical parameters are not sufficient, and a magnetic calibration procedure is indispensable.

7.3 Electro-mechanical characterization

To evaluate the robustness of the system against torsional vibrations, the rotational speed was obtained by calculating timing intervals between encoder pulses at different rotation speed levels, during 100 consecutive rotations. The obtained results are presented in Table 7.3, in terms of mean rotation speed $\overline{\omega}$, standard deviation σ, as well as the RMS and peak-to-peak of their relative percentage difference.

The mechanical characterization allowed us to choose the optimal rotation speed as a trade-off between the coil output voltage amplitude and vibration effects. Results show speed uniformity less than 1.5%, independent of the speed level, and a peak-to-peak variation of less than 10% at 0.25 rev/s and decreasing at around 5% at 0.75 rev/s. The rotation speed was set at 0.75 rev/s, obtaining at the nominal current of 93 A output voltages in the range of 1 $\mathrm{V_{pp}}$. Higher rotation speed values would increase the amplitude of the induced voltages but it can be observed to cause noticeable flexural vibrations and were therefore discarded.

Furthermore, the system's modal vibration components were studied by examining the harmonic components in the speed spectrum, which was generated at a nominal speed of 0.75 rev/s, and illustrated in Figure 7.5. If analyzing the spectrum at the rotation speed of 0.75 rev/s, it exhibits a flat white noise distribution, with the majority of components below the 10^{-3} rev/s level. The fundamental component related to the rotation speed is represented by a low-frequency peak at 0.75 Hz, while the resonance at approximately 90 Hz appears to be associated with the shaft's lowest torsional mode. The higher-frequency torsional components observed in the speed spectrum had no effect on the measurement results.

Table 7.3 Rotation speed analysis results [46].

Parameter	**0.25 [rev/s]**	**0.50 [rev/s]**	**0.75 [rev/s]**	**1 [rev/s]**
$\overline{\omega}$ [rev/s]	0.251	0.514	0.752	1.051
σ [rev/s]	4.973×10^{-3}	6.316×10^{-3}	5.822×10^{-3}	10.413×10^{-3}
RMS ($\frac{\Delta\omega}{\overline{\omega}}$) [%]	1.643	1.437	1.313	5.12
$(\frac{\Delta\omega}{\overline{\omega}})_{pp}$ [%]	8.656	6.818	3.825	10.412

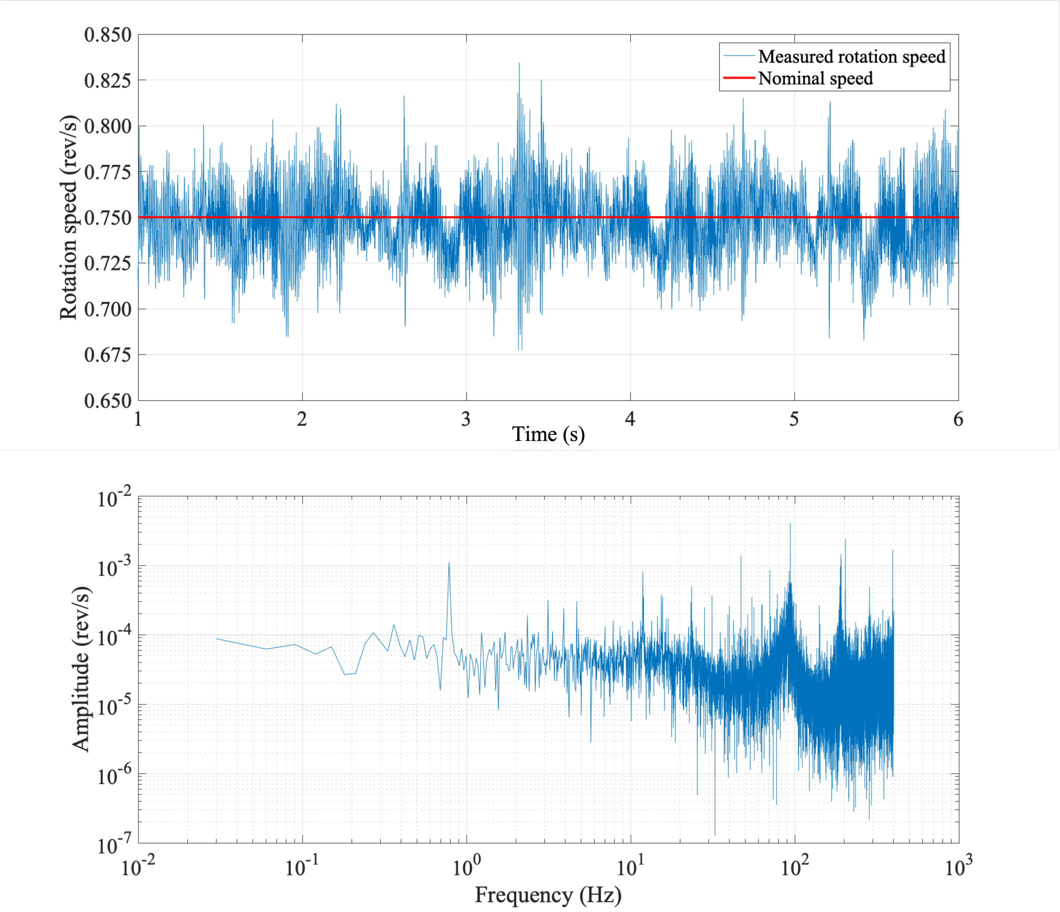

Fig. 7.5 (**a**) The instantaneous rotation speed signal in the time domain. (**b**) The frequency spectrum of instantaneous rotation speed signal at 0.75 rev/s nominal speed [46].

To further assess the mechanical quality of the rotation, a laser tracker was used to obtain a set of points from a retro-reflector mounted at one end of the shaft, as shown in Figure 7.6a, while rotating at the nominal speed of 0.75 rev/s. The obtained points were fitted to a circle, as illustrated in Figure 7.6b, with the center of the circle serving as the rotation axis of the coil shaft, arbitrarily set to the origin of the coordinate system. The radial difference between the measured points and the ideal circle's absolute value is less than 80 μm, as demonstrated in Figure 7.6c, which displays this difference as a function of the rotation angle. The coil signals used for measuring field harmonics can mitigate the effect of this imperfect rotation. The rotation axis exhibits an offset from the geometrical axis of the carbon fiber tube by $\Delta x = -0.522$ mm and $\Delta y = -0.856$ mm, as determined by moving the retro-reflector across the tube's outer surface. However, as the connection heads at the extremities, rather than the tube, define the axis of rotation of the PCB coil array, this offset does not affect the measurement quality.

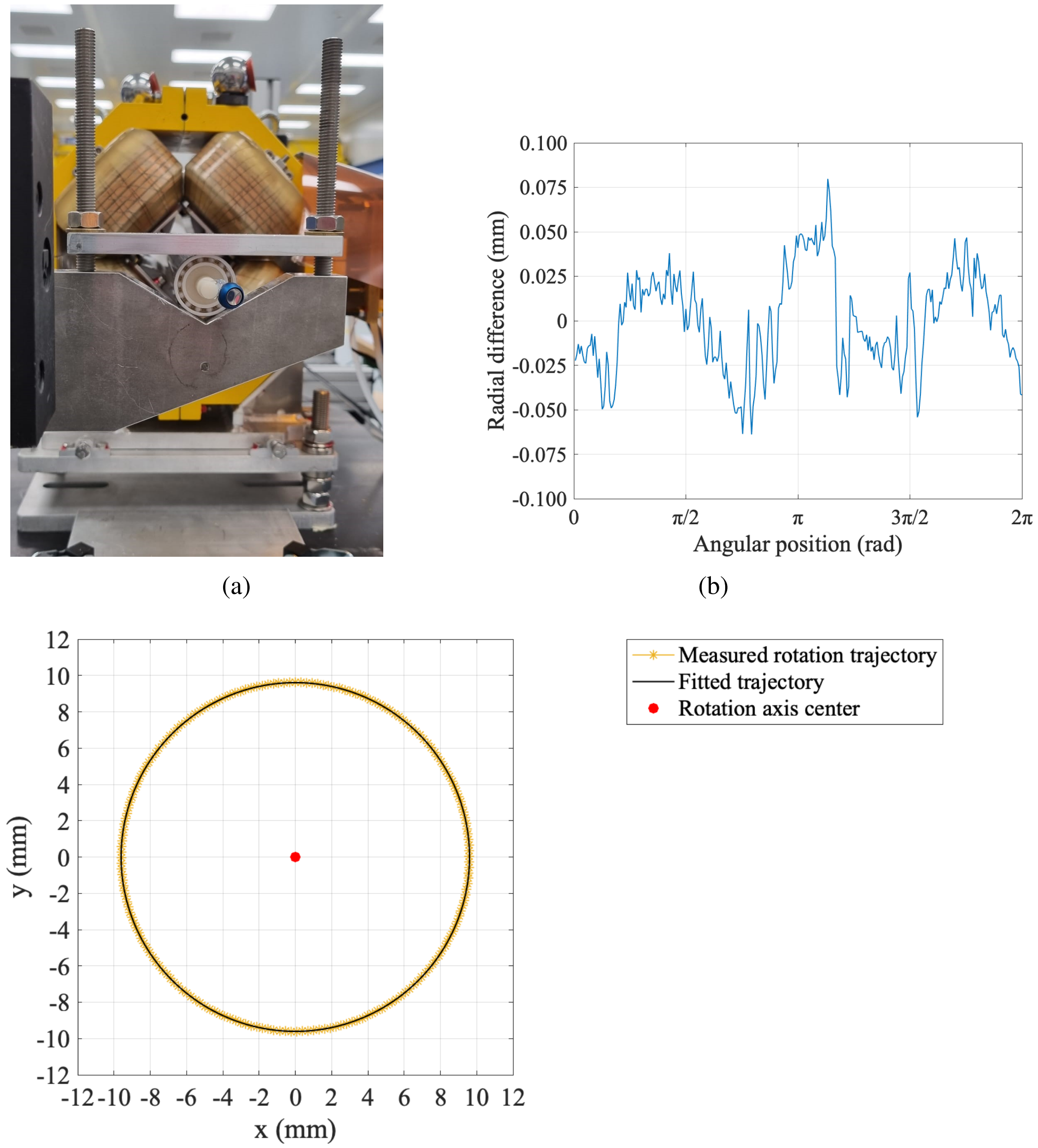

(a) (b)

(c)

Fig. 7.6 (**a**) Retro-reflector positioned at one shaft end for rotation axis localization. (**b**) Laser tracker measurements fit by the ideal circular trajectory. (**c**) Radial fit difference of the fitted circle to the laser tracker measurements. The results were obtained over 25 consecutive turns [46].

Chapter 8

Validation and field characterization

8.1 Study case I: BTF7 normal conducting quadrupole

The features of the BTF 7 quadrupole, tested at CERN and at INFN-LFN laboratories, with the proposed ⌀26 mm rotating-coil system, are summarized in Table 8.1. In Sec. 5.3, the compensation scheme configuration adopted by the proposed rotating-coil measurement system has been introduced. The dominant harmonic term has been measured using the absolute coil $Coil_A$, and the dipole and quadrupole bucked signal have been reconstructed digitally by adopting the linear combination given as $Coil_A - Coil_B - Coil_C + Coil_D$.

Figure 8.1a shows the acquired voltage signals in both the absolute and compensated configurations The Absolute and compensated filtered voltage signals for 5 consecutive rotations (single rotation is between two dotted lines), while Fig. 8.1b demonstrates the advantages of the compensation scheme by displaying a lower accuracy in the measurement of the harmonic coefficient from the absolute signal. The results were obtained at r_0 = 10 mm, and computed over 25 rotations. The ratio of the second-order harmonic coefficient in the absolute and compensated measurements is called the compensation or bucking factor and is around 700.

Table 8.1 Specifications of the BTF7 EuPRAXIA quadrupole prototype tested at CERN.

Parameter	Value
Aperture diameter	⌀45 mm
Reference radius r_0	10 mm
Nominal magnetic field gradient	50 T/m
Nominal current	93 A
Iron yoke length	440 mm
Total field extension (incl. fringe)	600 mm

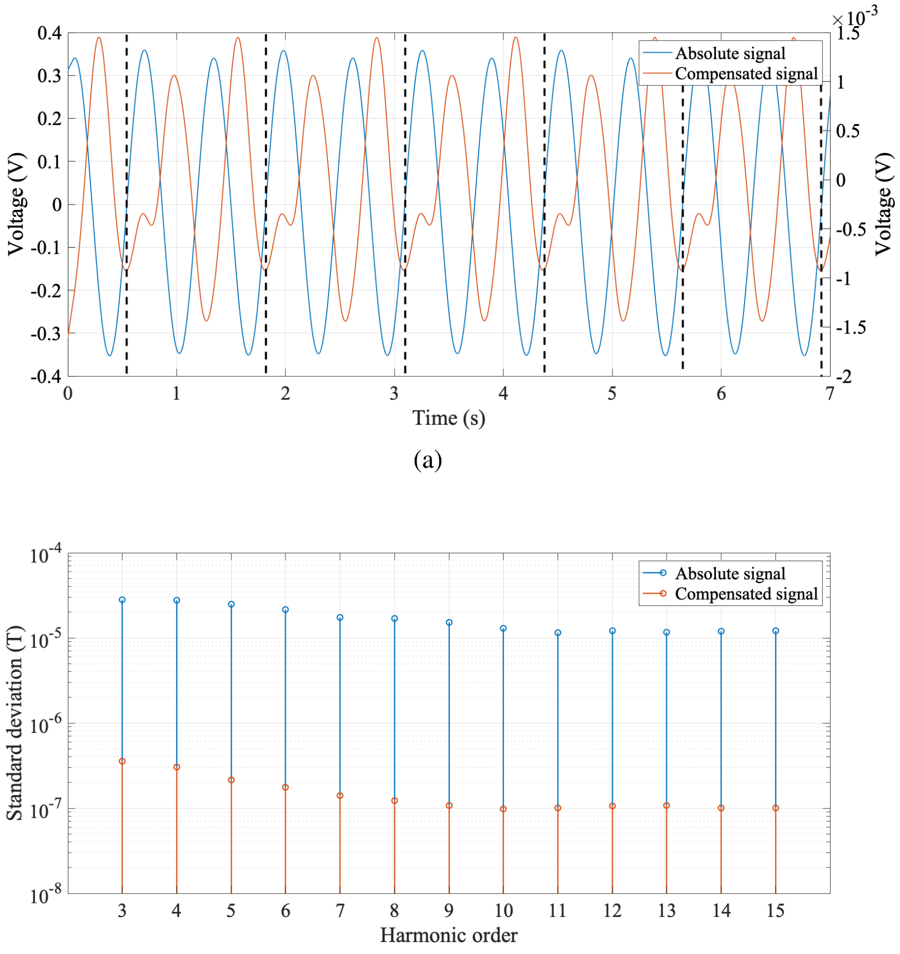

(a)

(b)

Fig. 8.1 Acquired signals analysis from BTF7 measurement. (**a**) Absolute and compensated filtered voltage signals for 5 consecutive rotations (single rotation is between two dotted lines) and (**b**) Standard deviation for higher-order harmonic coefficients C_n, computed from the absolute and compensated signal. The results were obtained at r_0 = 10 mm, and computed over 25 rotations [46].

8.1.1 Magnetic loadline and integrated gradient

The magnet Transfer Function, i.e. the ratio between the field and excitation current, was measured in DC mode on current plateaus from 0 A up to 100 A and compared with the results obtained by an SSW measurement system. The SSW measurement setup is shown in Fig. 8.2a, while the $\varnothing$26 mm rotating-coil system measurement setup is shown in Fig. 8.2b. The Transfer Function is shown in Fig. 8.3 and is in good general agreement with the Single Stretched Wire measurements.

The integrated gradient at the nominal magnet current of 93 A, computed after magnet pre-cycling, is -4.0789 T, i.e., equal (by calibration) to the reference value measured with the SSW, with a repeatability $\sigma = 6.6391\ 10^{-5}$ T.

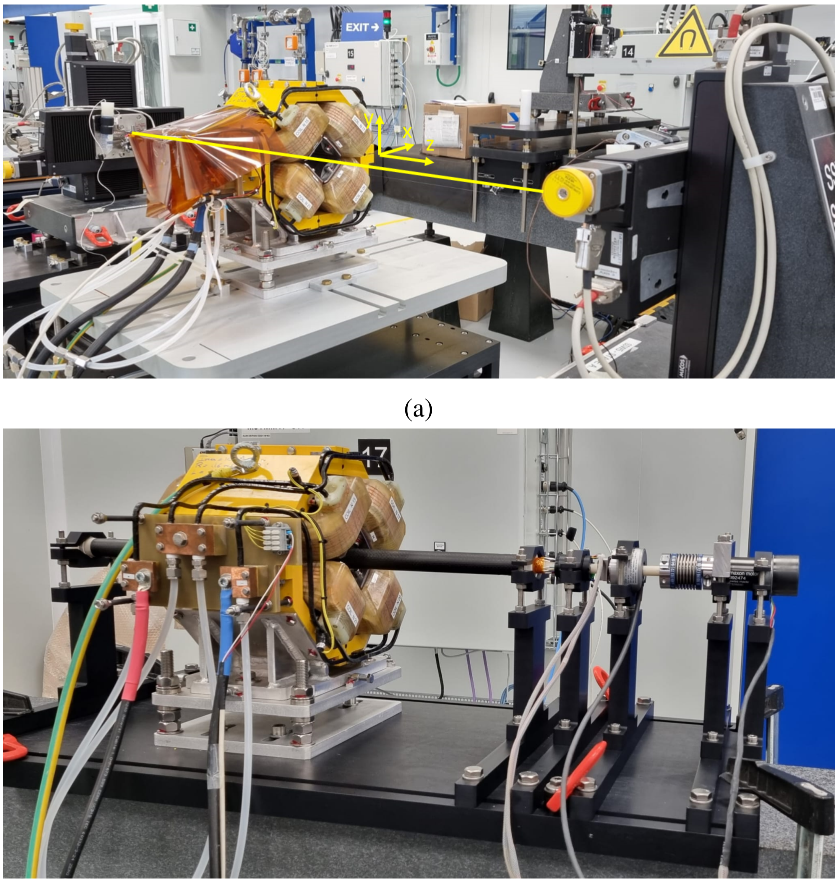

(a)

(b)

Fig. 8.2 BTF7 measurement setup. **(a)** The BTF7 quadrupole magnet SSW measurement setup and **(b)** the $\varnothing$26 mm rotating-coil system installed in the BTF7 quadrupole magnet used as a measurement reference between CERN and INFN laboratories [46].

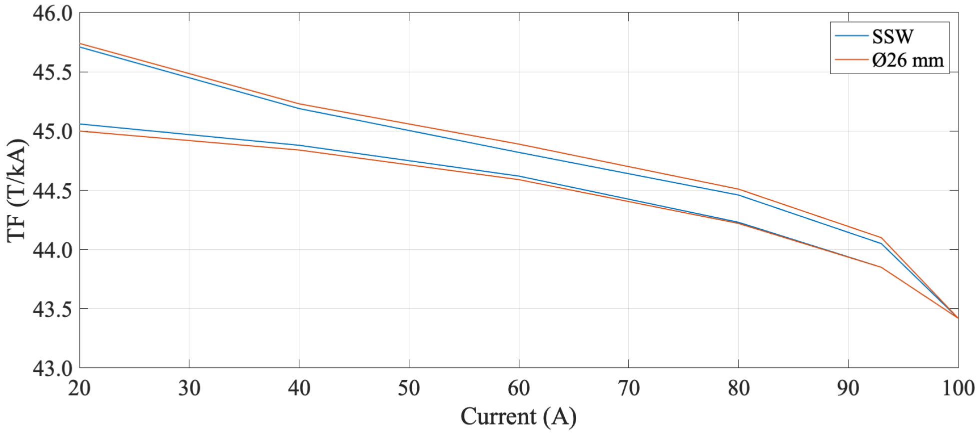

Fig. 8.3 BTF7 transfer function measured in DC mode from 0 to 100 a and back to 0, compared to the result obtained with the Single Stretched Wire system. For each current plateau, the averaged gradient at the magnet center was divided by the corresponding current value. The slope of the curve is due to the saturation of the iron yoke [46].

8.1.2 Comparison with an existing Rotating-Coil System

To cross-check the measured harmonic field components of the quadrupole magnet, a ⌀30 mm rotating-coil probe, already in use at CERN, was employed, along with the ⌀26 mm rotating-coil system.

Measurements were performed adopting two pre-cycling conditions: (i) after degaussing, (ii) pre-cycling the magnet with three cycles between 0 and 100 A. The ⌀30 mm rotating-coil measurement system includes a fast digital integrator [57] for voltage integration and a software application to control the hardware components and for the acquisition and post-processing of data.

The field multipole measurement results obtained from the quadrupole compensation scheme are reported in Figure 8.4 and compared to the results obtained from the ⌀30 mm system and the SSW system. Higher-order harmonics computed over 100 repetitions and measurement repeatability are reported in Table 8.2, compared to measurement results obtained with the ⌀30 mm rotating-coil system. The measurement repeatability was tested at different rotation speed values and the results reported in Figure 8.5 show the same pattern for the standard deviations. The relatively high values of harmonics c_3 and c_4 are related to the difficulties in respecting the mechanical tolerances during magnet assembly. The results highlight the effectiveness of digital bucking of the dipole and quadruple field components in reducing the standard deviation of higher-order multipoles by almost two orders of magnitude, down to well below 3 μT, i.e., around 1 ppm.

Table 8.2 Comparison of measurement repeatability for higher-order multipoles c_n at r_0 = 10 mm and nominal current 93 A measured with both rotating over 100 rotations, at the nominal rotation speed of 0.75 rev/s [46].

Harmonic Order	**⌀26 mm c_n [units]**	**⌀26 mm σ [units]**	**⌀30 mm c_n [units]**	**⌀30 mm σ [units]**
c_3	8.75	3.03×10^{-2}	8.79	2.03×10^{-2}
c_4	3.04	3.88×10^{-2}	3.88	2.03×10^{-2}
c_5	0.98	3.32×10^{-2}	0.63	4.31×10^{-2}
c_6	1.10	2.78×10^{-2}	0.93	4.64×10^{-2}
c_7	0.06	2.18×10^{-2}	0.01	5.2×10^{-2}
c_8	0.03	1.91×10^{-2}	0.05	1.06×10^{-2}
c_9	0.02	1.67×10^{-2}	0.04	6.70×10^{-2}
c_{10}	0.01	1.55×10^{-2}	0.02	9.59×10^{-2}
c_{12}	0.01	1.53×10^{-2}	0.04	1.57×10^{-2}
c_{13}	0.01	1.47×10^{-2}	0.02	3.25×10^{-2}
c_{14}	0.01	1.45×10^{-2}	0.01	2.53×10^{-2}
c_{15}	0.01	1.43×10^{-2}	0.01	2.42×10^{-2}

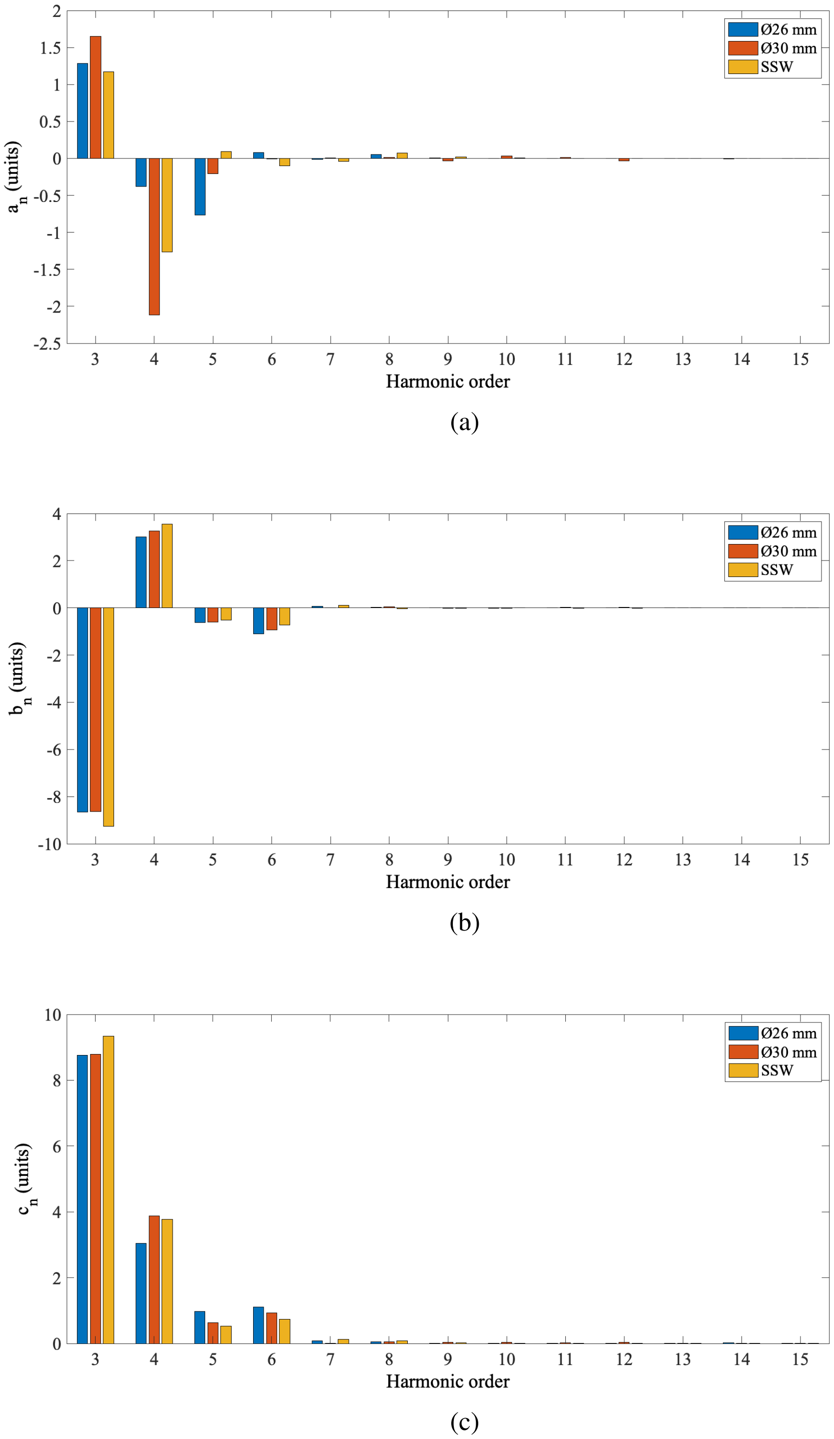

Fig. 8.4 BTF 7 harmonic analysis results. (**a**) Higher-order normalized skew coefficients a_n. (**b**) Higher-order normalized normal coefficients b_n. (**c**)Higher-order normalized harmonic coefficients c_n. Higher-order coefficients are expressed at r_0 = 10 mm and nominal current 93 A and measured with both rotating-coil systems and SSW system, over 100 rotations, at the nominal rotation speed of 0.75 rev/s [46].

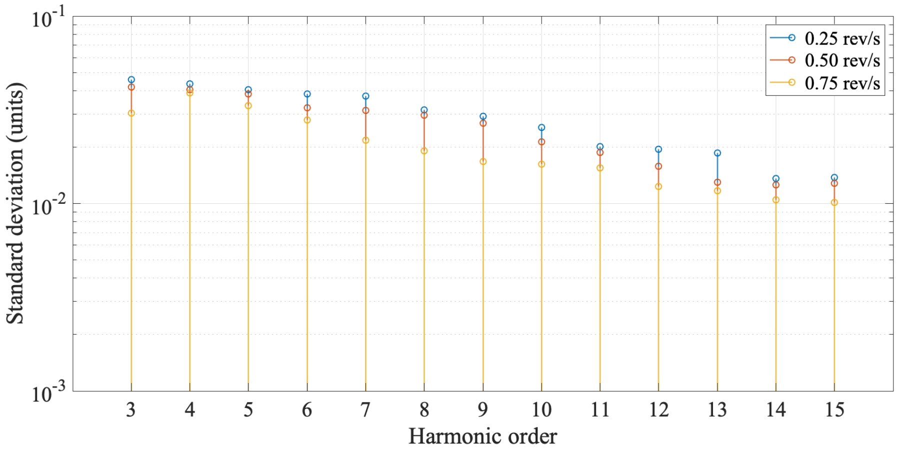

Fig. 8.5 Comparison of measurement repeatability for higher-order multipoles c_n at r_0 = 10 mm and nominal current 93 A for different rotation speed values [46].

8.1.3 Measurement reproducibility analysis

Magnetic measurements performed using rotating coil systems may introduce potential sources of variability due to factors like coil calibration, positioning, and environmental conditions. To assess the reliability of the measurement process and ensure consistent and replicable results, studies focused on measuring reproducibility have been conducted, investigating the level of agreement, consistency, or variability between repeated measurements performed in two different laboratories.
In particular, the same ⌀26 mm rotating coil system has been used to measure the same BTF7 quadrupole magnet in two different locations, i.e. at CERN magnetic measurement laboratory, as described in previous sections, and at the INFN-LFN laboratory of Frascati.

The analysis utilize a Bland-Altman plot, considered a valuable tool for the visual assessment of the agreement and consistency between measurement results. The measurements were performed following a standardized protocol to ensure consistency across the experiments. The measurement protocol entailed powering the magnet at current level of 93 A, following the prescribed degaussing and pre-cycling phases outlined in Sec. 8.1.2. Additionally, data collection took place during 30 shaft rotations, ensuring a paired measurement approach where each acquired sample had a corresponding measurement from both laboratories. The rotation speed was set at 0.75 rev/s.

In a general form, given two sets of N data, obtained from the two laboratories, denoted as x_i and y_i for i=1 to N, the Bland-Altman analysis involves two primary steps. Firstly, the set of data $D = d_1, ..., d_N$ is constructed, representing the differences between the paired measurements, calculated as $d_i = x_i - y_i$ for i=1 to N. Secondly, the set $M = \mu_1, ..., \mu_N$ of average values is derived, representing the mean of each pair of measurements, denoted as $\mu_i = \mu(x_i, y_i)$ for i=1 to N.

This approach facilitated a comprehensive evaluation of the agreement and reproducibility of the measurements obtained from the two laboratories. In particular, the magnetic field parameters object of the reproducibility study were the main field component B_2 and the normalized higher-order field components c_3, c_4, c_5, and c_6. The Bland-Altman plots were obtained by plotting the differences D between the two sets of measurements on the y-axis, against their average M on the x-axis. The plots also include reference lines to indicate the mean difference $d^* = \mu(D)$ and the upper and lower limits of the confidence interval, used to assess the statistical significance of the observed agreement, calculated as $d^* \pm 1.96\sigma$, where σ is the standard deviation of the differences D.

The plot obtained for the main field components is shown in Fig. 8.6, while for the higher-order field components plots are shown in Figs. 8.7a to 8.7d.

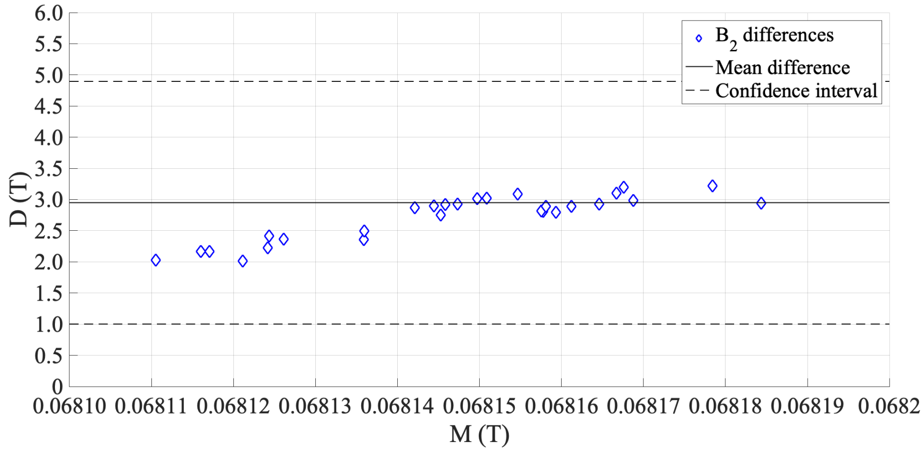

Fig. 8.6 Bland-Altman plot of reproducibility in the assessments of BTF7 main filed component.

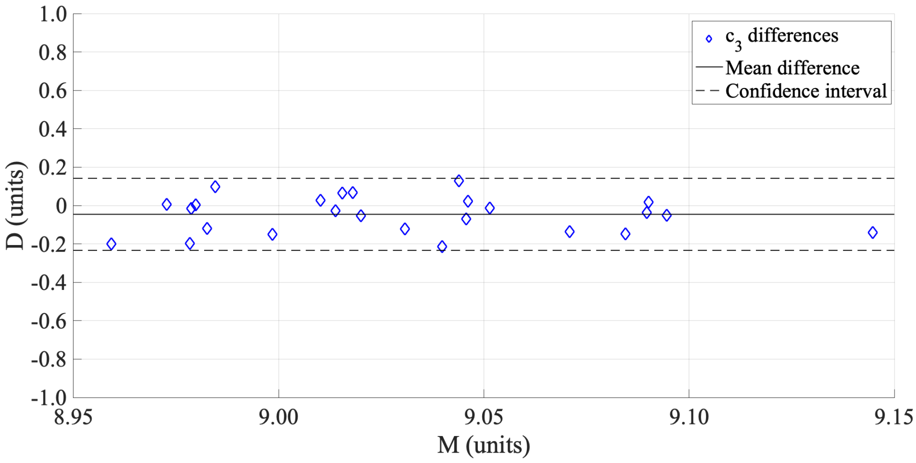

(a)

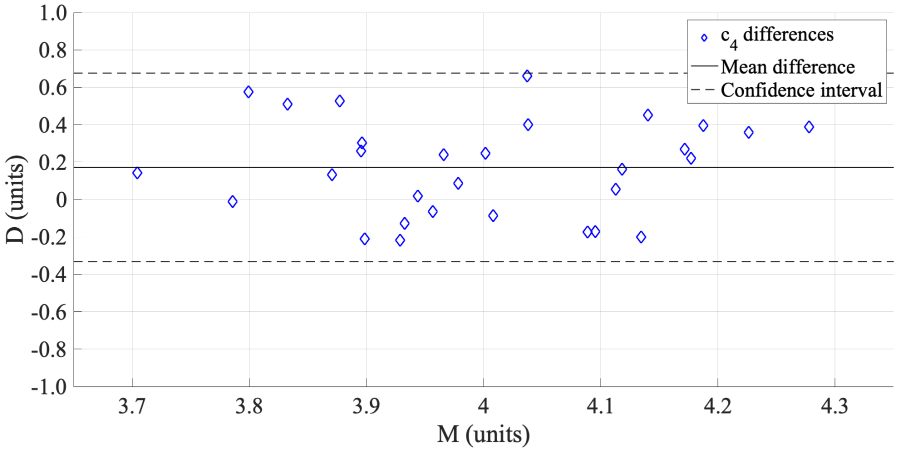

(b)

Fig. 8.7 Bland-Altman plot of reproducibility in the assessments of BTF7 higher-order field components. (**a**) reproducibility analysis for c_3 field component, (**b**) reproducibility analysis for c_4 field component, (**c**) reproducibility analysis for c_5 field component and (**d**) reproducibility analysis for c_6 field component.

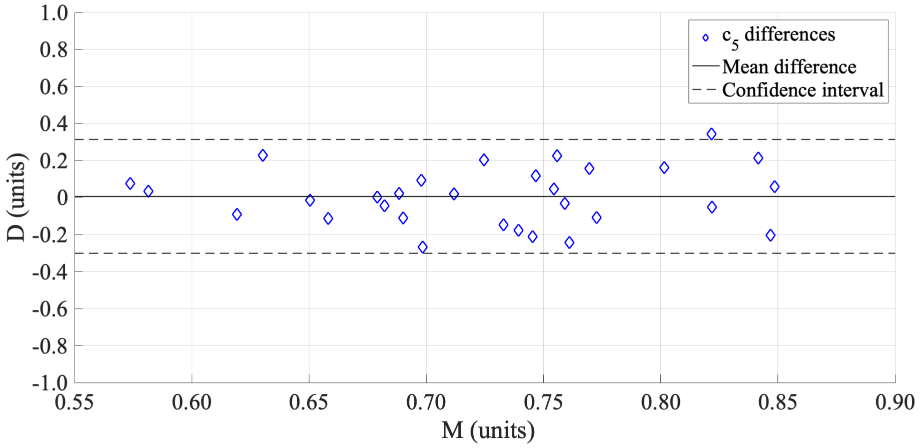

(c)

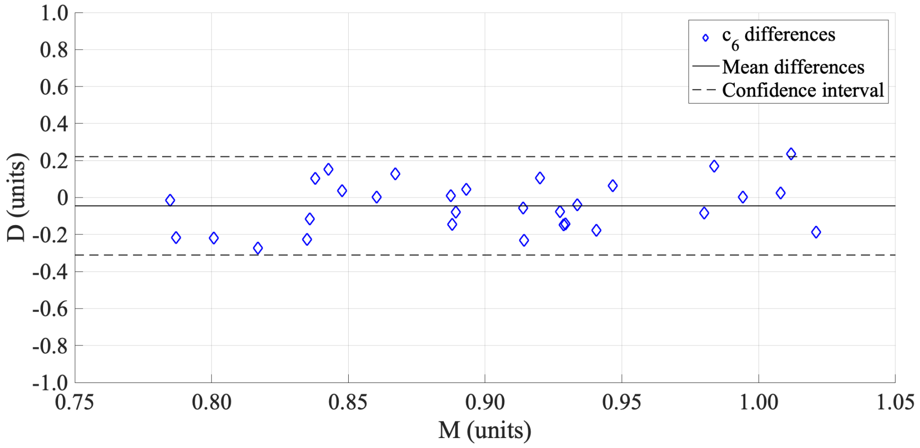

(d)

Fig. 8.7 Bland-Altman plot of reproducibility in assessments of average higher-order field components. (**a**) reproducibility analysis for c_3 field component, (**b**) reproducibility analysis for c_4 field component, (**c**) reproducibility analysis for c_5 field component and (**d**) reproducibility analysis for c_6 field component (cont.).

Examining the distribution of the points on the scatter plots, it is possible to conclude that no significant systematic errors or biases are present. The data points appear to be randomly scattered around the mean difference line, indicating a lack of any consistent directional deviations. This suggests that both laboratories are producing measurements that are in good agreement with each other.
Almost the totality of the measured variables falls within the confidence interval range, indicating that the differences between the measurements are statistically consistent and not significantly different from zero. Plots provide evidence of the reproducibility and reliability of the measurement results, as the measured values consistently align within an acceptable range of variation. Considering the practical implications of the proposed measurement system, results indicate that the measurements from both laboratories are comparable and can be reliably used for further analysis performed independently by both laboratories.

8.2 Study case II: Linac4 permanent magnet

The performances of the $\varnothing 26$ mm rotating coil system were tested also on the permanent magnet Linac4. The features of the tested quadrupole are summarized in Table 8.3. The magnet was previously measured with the SSW system, shown in Fig. 8.8. The measurement setup for the $\varnothing 26$ mm rotating coil system is visible in Fig. 8.9.

In Figure 8.10a, the voltage signals obtained in both absolute and compensated configurations are presented, while Figure 8.10b illustrates the advantages of the compensation scheme by showing a significant improvement in the accuracy of the measurement of the harmonic coefficient when using the compensated signal. The digital bucking achieved a factor of over 1000, leading to a substantial reduction in the standard deviation of higher-order multipoles by almost two orders of magnitude, resulting in a value of less than 3 μT or around 1 ppm. These findings underscore the effectiveness of digitally bucking the dipole and quadruple field components.

Table 8.3 Specifications of the Linac4 permanent quadrupole magnet at CERN.

Parameter	Value
Aperture diameter	$\varnothing 45$ mm
Reference radius r_0	10 mm
Nominal magnetic field gradient	16.7 T/m
Iron yoke length	100 mm
Total field extension (incl. fringe)	300 mm

8.2.1 Harmonic analysis

The field multipole measurement results, obtained from the quadrupole compensation scheme, and measurement repeatability are reported in Table 8.4, compared to measurement results obtained with the SSW system results. Higher-order harmonics computed over 100 repetitions are also shown in Figure 8.11, compared to the results obtained from the SSW system. Also in this case, the 26 mm rotating coil system has been successfully used to detect the presence of relatively high values of harmonics c_3 and c_4, related to the difficulties in respecting the mechanical tolerances during magnet assembly.

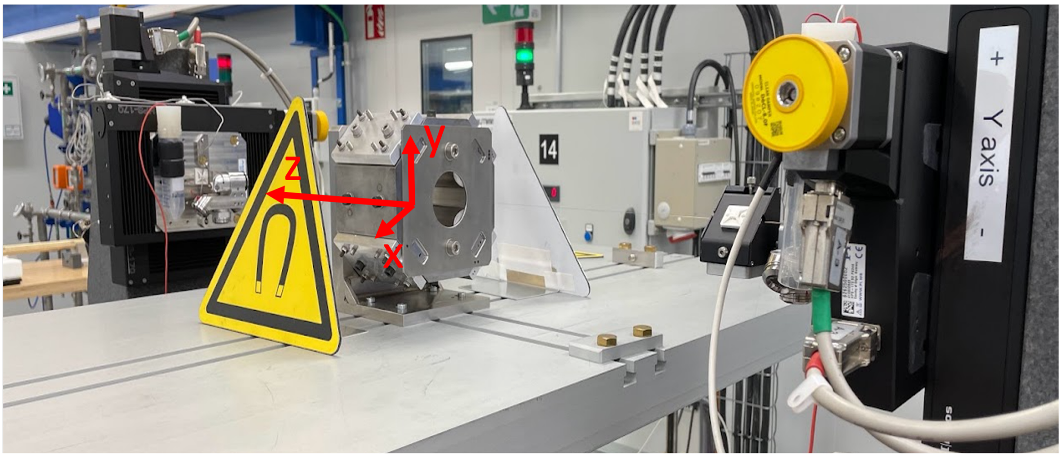

Fig. 8.8 Linac4 SSW measurement setup.

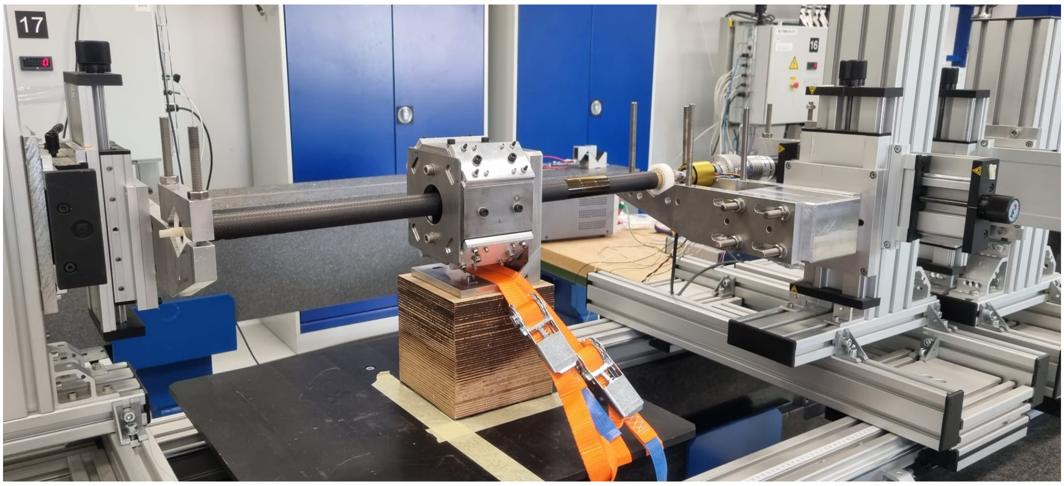

Fig. 8.9 Linac4 ⌀26 mm rotating coil system measurement setup.

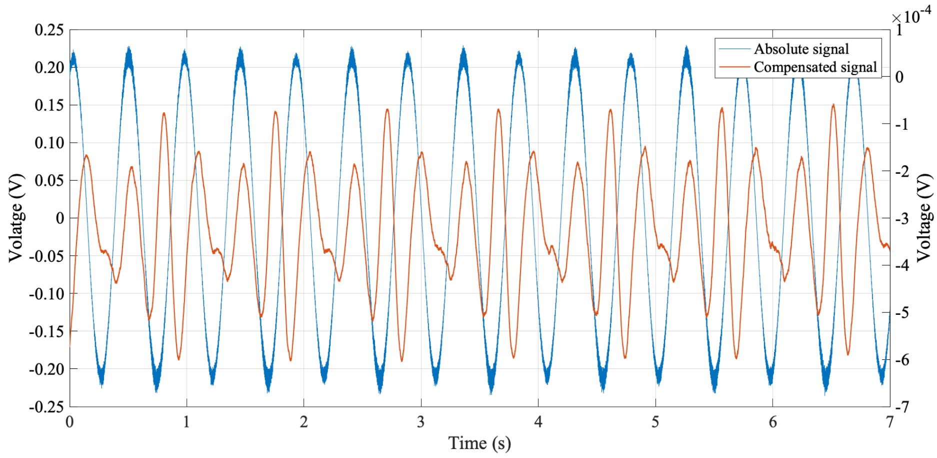

(a)

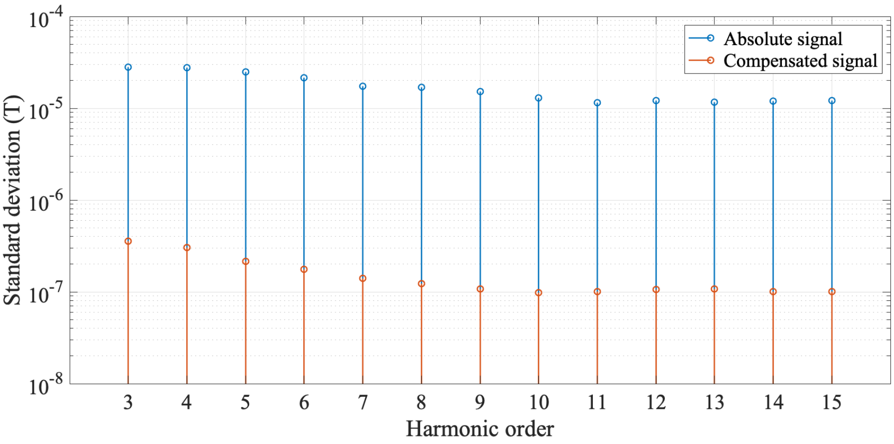

(b)

Fig. 8.10 Acquired signals analysis from Linac4 measurement.(**a**) Absolute and compensated filtered voltage signals for 5 consecutive rotations. (**b**) Standard deviation for higher-order harmonic coefficients C_n, computed from the absolute and compensated signal. The results were obtained at r_0 = 10 mm and computed over 25 rotations.

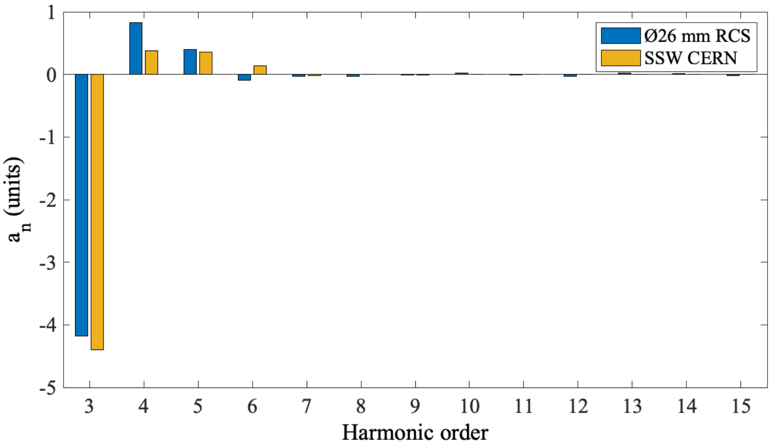

(a)

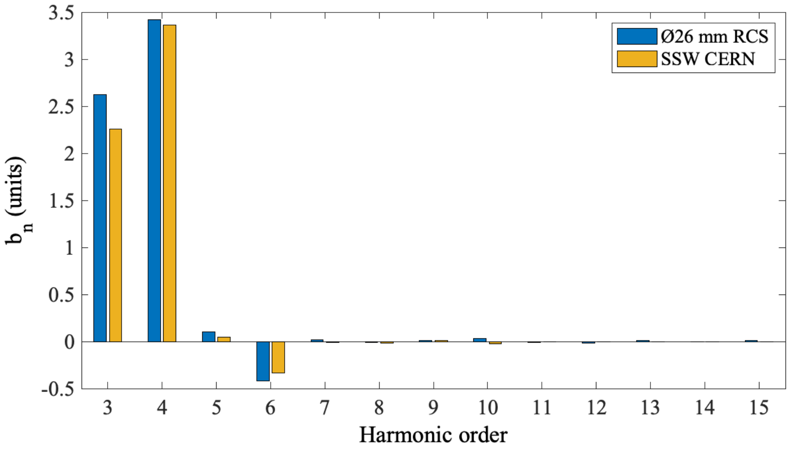

(b)

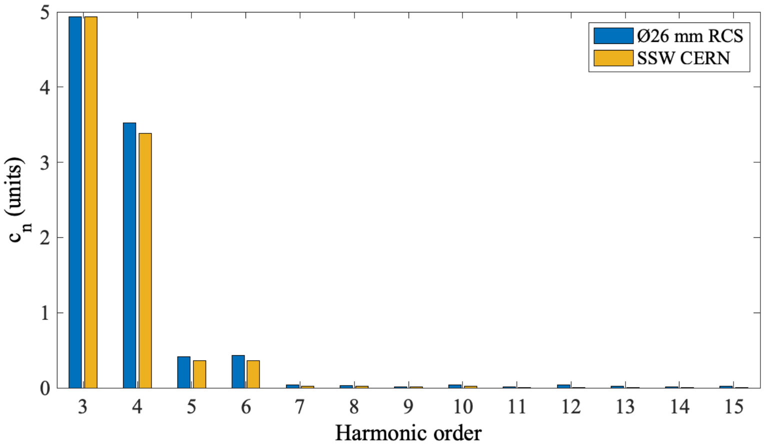

(c)

Fig. 8.11 Linac4 harmonic analysis results, compared to SSW measurement results. (**a**) Higher-order normalized skew coefficients a_n. (**b**) Higher-order normalized normal coefficients b_n. (**c**) Higher-order normalized harmonic coefficients c_n. Higher-order coefficients are expressed at r_0 = 10 mm over 100 rotations, at the nominal rotation speed of 0.75 rev/s.

Table 8.4 Linac4 measurement repeatability for higher-order multipoles c_n at $r_0 = 10$ mm, measured with ⌀26 mm and SSW systems over 100 rotations, at the nominal rotation speed of 0.75 rev/s.

Harmonic Order	**⌀26 mm c_n [units]**	**⌀26 mm σ [units]**	**SSW c_n [units]**	**SSW σ [units]**
c_3	4.93	6.78×10^{-1}	4.94	7.37×10^{-1}
c_4	3.52	7.87×10^{-1}	3.38	1.96×10^{-1}
c_5	0.42	8.50×10^{-2}	0.36	6.40×10^{-2}
c_6	0.43	5.81×10^{-2}	0.36	4.78×10^{-2}
c_7	0.04	9.71×10^{-3}	0.02	2.12×10^{-2}
c_8	0.03	9.98×10^{-3}	0.01	9.90×10^{-3}
c_9	0.01	8.11×10^{-3}	0.01	7.99×10^{-3}
c_{10}	0.04	7.63×10^{-3}	0.01	3.27×10^{-3}
c_{12}	0.01	9.57×10^{-3}	0.01	1.43×10^{-3}
c_{13}	0.01	9.98×10^{-3}	0.01	8.54×10^{-3}
c_{14}	0.02	1.52×10^{-3}	0.01	4.76×10^{-3}
c_{15}	0.01	3.43×10^{-3}	0.01	2.42×10^{-4}

Conclusion and Outlook

This thesis describes the design and development of a novel small-radius rotating-coil measurement system, required to assess the field quality of small-bore quadrupole magnets, with a diameter of 30 mm or greater, in the context of the EuPRAXIA project. The EuPRAXIA project investigates the realization of the next generation of more compact and cost-efficient plasma-based accelerators, for a wide range of scientific applications.

The need for high acceleration gradients over short distances is essential to realize compact plasma accelerator facilities. To satisfy this requirement, small-bore permanent quadrupole magnets have been introduced by the Eupraxia design in the beam-line layout. Plasma-based accelerators are able to produce high-energy particle beams, despite often suffering from poor beam quality, due to large energy spread and high emittance.

Characterization of accelerator magnets magnetic field is crucial to verify the magnet design met all specifications, as mandated by beam optics requirements. Moreover, accurate magnetic measurements allow the calibration of beam diagnostic tools, such as beam position monitors and beam profile monitors, and the measurements results are fundamental for the optimization of magnet design and performances.

The proposed ⌀26 mm rotating coil measurement system, utilizing the PCB technology, offers a solution to address the challenges associated with accurate field characterization of small-bore quadrupole magnets. The PCB-based magnetometer, i.e. an array of nominally identical radial coils, is characterized by a narrow width of 25 mm, if compared to its length of 600 mm, and an unusual turns density, given by 256 turns over 32 layers. The proposed PCB design was implemented only extremely optimizing the production. In fact, despite the precision of tracks location on the PCB was estimated to reach a remarkable value of approximately 2μm, being the foundation for the successfully high bucking ratio between 700 and 1000, some manufacturing process concerns emerged. This emphasized the significance of magnetic calibrating in high-accuracy applications.

The results obtained from the mechanical characterization essentially validated the innovative mechanical design, based on inserting the PCB array magnetometer directly in a commercially available carbon fiber tube, by means of 3D-printed plastic inserts. Despite the low rigidity of the Accura 25 ® or Bluestone ® used for the inserts, and the need to retouch them slightly on the lathe, the quality of the rotation was high, with torsional vibrations peaking at the safely high-frequency of 90 Hz and within 1.5% RMS in amplitude, at 0.75 rev/s rotational speed.

The feasibility of using a small-radius PCB-based magnetometer for high-precision magnetic field measurement was demonstrated through field characterization of permanent and resistive quadrupole magnets with a bore diameter of 45 mm. Comparison with other measurement instruments, such as a SSW system and an old prototype of rotating coil systmem in use at CERN, proved that the proposed small-radius rotating coil system can achieve absolute accuracy of the main integrated gradient of approximately 50 ppm, with a repeatability of 10 ppm, while the accuracy of high-order compensated harmonics is approximately 100 ppm with a repeatability of 10 ppm. These performances meet the requirements for the measurement of the EuPRAXIA magnets.

Moreover, the results obtained from the Bland-Altman plots analysis provided reassurance regarding the reliability and agreement of the measurement results obtained at CERN and INFN-LFN laboratories. The absence of significant systematic errors, the high level of agreement, and the consistent alignment within the confidence interval range contributed to assess the robustness and validity of the experimental results, confirming confidence in their accuracy and reproducibility.

Resorting to low-cost, commercially available hardware components and 3D-printed parts was key to ensuring this design's wide applicability and fast and cost-effective modifications.

Overall, the experimental results shown the proposed $\varnothing$26 mm rotating coil system was capable of measuring magnetic fields with a high degree of accuracy, even in the presence of noise and interference. This makes it a valuable tool for the characterization and calibration of small-bore quadrupoles, which are fundamental magnetic components, especially in compact plasma-based accelerator systems.

For future development, a review of the PCB magnetometer design has been initiated, encompassing several improvements. These include the introduction of teardrop-shaped wire soldering pads, the integration of pads on internal layers for a 4-point resistance measurement, enabling accurate detection of short circuits between layers. Furthermore, a shift from FR4 to 50μm thick Kapton as the PCB base material, with 5μm thick copper traces on each side, is proposed to enhance PCB yield.

In addition to these design enhancements, suggestions have been made for further improvements and future research directions to enhance the performance of the proposed rotating coil system, which is intended for installation at the INFN-LFN laboratory in Frascati (Italy). Modifications to the shaft support are planned to facilitate horizontal displacement of the instrument within the magnet bore, thereby improving the accuracy of the in-situ radius calibration procedure outlined in Sec. 7.2. The final version of the rotating coil system will be installed at CERN and INFN-LFN to complete the measurement of the magnetic axis offset relative to the magnet's fiducial reference systems. The incorporation of suitable, reproducible optical targets into the proposed layout is foreseen by the actual design.

In conclusion, the proposed rotating coil system represents a promising tool for achieving accurate and reliable measurements in the specific context of EuPRAXIA quadrupole magnets field characterization. Further refinement and optimization of the design are expected to yield additional benefits, significantly supporting advancements in the design of PCB-based rotating-coil magnetic measurement systems for small-bore diameter magnets characterization.

References

[1] R. W. Assmann, M. K. Weikum, T. Akhter, D. Alesini, A. S. Alexandrova, M. P. Anania, N. E. Andreev, I. Andriyash, M. Artioli, A. Aschikhin, T. Audet, A. Bacci, I. F. Barna, S. Bartocci, A. Bayramian, A. Beaton, A. Beck, M. Bellaveglia, A. Beluze, A. Bernhard, A. Biagioni, S. Bielawski, F. G. Bisesto, A. Bonatto, L. Boulton, F. Brandi, R. Brinkmann, F. Briquez, F. Brottier, E. Bründermann, M. Büscher, B. Buonomo, M. H. Bussmann, G. Bussolino, P. Campana, S. Cantarella, K. Cassou, A. Chancé, M. Chen, E. Chiadroni, A. Cianchi, F. Cioeta, J. A. Clarke, J. M. Cole, G. Costa, M. -e. Couprie, J. Cowley, M. Croia, Y. Li, and G. Xia. Eupraxia conceptual design report. *The European Physical Journal. Special Topics*, 229(24):3675–4284, 2020.

[2] Assmann R. W. et al. Eupraxia conceptual design report. *The European Physical Journal Special Topics*, 229:3675–4284, 12 2020.

[3] S Arjmand, D Alesini, MP Anania, A Biagioni, E Chiadroni, A Cianchi, D Di Giovenale, G Di Pirro, M Ferrario, V Lollo, et al. Characterization of plasma sources for plasma-based accelerators. *Journal of Instrumentation*, 15(09):C09055, 2020.

[4] R Pompili, MP Anania, M Bellaveglia, A Biagioni, S Bini, F Bisesto, E Brentegani, G Castorina, E Chiadroni, A Cianchi, et al. Experimental characterization of active plasma lensing for electron beams. *Applied Physics Letters*, 110(10):104101, 2017.

[5] A Vannozzi, D Alesini, C Sanelli, and C Vaccarezza. New tunable high gradient permanent magnet quadrupole for plasma wake field acceleration at sparc _lab. In *Journal of Physics: Conference Series*, volume 1596, page 012009. IOP Publishing, 2020.

[6] N Smirnov, L Bottura, M Calvi, G Deferne, J DiMarco, N Sammut, and S Sanfilippo. Focusing strength measurements of the main quadrupoles for the lhc. *IEEE Transactions on applied superconductivity*, 16(2):261–264, 2006.

[7] Pasquale Arpaia, Carlo Petrone, Stephan Russenschuck, and Louis Walckiers. Vibrating-wire measurement method for centering and alignment of solenoids. *Journal of Instrumentation*, 8:11006, 2013.

[8] J. DiMarco, G. Chlachidze, A. Makulski, D. Orris, M. Tartaglia, J. C. Tompkins, G. V. Velev, and X. Wang. Application of pcb and fdm technologies to magnetic measurement probe system development. *Submitted to IEEE Trans.Appl.Supercond.*, 10 2012.

[9] Stephan Russenschuck. *Field computation for accelerator magnets: Analytical and numerical methods for electromagnetic design and optimization*. Wiley-VCH, Weinheim, 2010.

[10] Ernest O. Lawrence and M. Stanley Livingston. The production of high speed light ions without the use of high voltages. *Phys. Rev.*, 40:19–35, Apr 1932.

[11] Albert De Roeck, John Ellis, Christophe Grojean, Sven Heinemeyer, Karl Jakobs, Georg Weiglein, James Wells, G Azuelos, S Dawson, B Gripaios, et al. From the lhc to future colliders: Cern theory institute summary report. *The European Physical Journal C*, 66:525–583, 2010.

[12] K. Oide, M. Aiba, S. Aumon, M. Benedikt, A. Blondel, A. Bogomyagkov, M. Boscolo, H. Burkhardt, Y. Cai, A. Doblhammer, B. Haerer, B. Holzer, J. M. Jowett, I. Koop, M. Koratzinos, E. Levichev, L. Medina, K. Ohmi, Y. Papaphilippou, P. Piminov, D. Shatilov, S. Sinyatkin, M. Sullivan, J. Wenninger, U. Wienands, D. Zhou, and F. Zimmermann. Design of beam optics for the future circular collider e^+e^- collider rings. *Phys. Rev. Accel. Beams*, 19:111005, Nov 2016.

[13] Philip Bambade, Ties Behnke, Mikael Berggren, Ivanka Bozovic-Jelisavcic, Philip Burrows, Massimo Caccia, Paul Colas, Gerald Eigen, Lyn Evans, Angeles Faus-Golfe, Brian Foster, Juan Fuster, Frank Gaede, Christophe Grojean, Marek Idzik, Andrea Jeremie, Tadeusz Lesiak, Aharon Levy, Benno List, Jenny List, Joachim Mnich, Olivier Napoly, Carlo Pagani, Roman Poeschl, Francois Richard, Aidan Robson, Thomas Schoerner-Sadenius, Marcel Stanitzki, Steinar Stapnes, Maksym Titov, Marcel Vos, Nicholas Walker, Hans Weise, and Marc Winter. The international linear collider. a european perspective, 2019.

[14] C. Glide-Hurst, M. Bellon, R. Foster, C. Altunbas, M. Speiser, M. Altman, D. Westerly, N. Wen, B. Zhao, M. Miften, I. J. Chetty, and T. Solberg. Commissioning of the varian truebeam linear accelerator: A multi-institutional study. *Medical Physics*, 40(3):031719, 2013.

[15] B W Raaymakers and all. First patients treated with a 1.5 t mri-linac: clinical proof of concept of a high-precision, high-field mri guided radiotherapy treatment. *Physics in Medicine and Biology*, 62(23):L41, nov 2017.

[16] M. P. Minitti, J. M. Budarz, A. Kirrander, J. S. Robinson, D. Ratner, T. J. Lane, D. Zhu, J. M. Glownia, M. Kozina, H. T. Lemke, M. Sikorski, Y. Feng, S. Nelson, K. Saita, B. Stankus, T. Northey, J. B. Hastings, and P. M. Weber. Imaging molecular motion: Femtosecond x-ray scattering of an electrocyclic chemical reaction. *Phys. Rev. Lett.*, 114:255501, Jun 2015.

[17] Wojciech Błachucki, Anna Wach, Joanna Czapla-Masztafiak, Mickaël Delcey, Christopher Arrell, Rafał Fanselow, Pavle Juranić, Marcus Lundberg, Christopher Milne, Jacinto Sá, and Jakub Szlachetko. Approaching the attosecond frontier of dynamics in matter with the concept of x-ray chronoscopy. *Applied Sciences*, 12(3), 2022.

[18] Peter Williams. A route to greener big science. *Nature Physics*, pages 1,2, 2023.

[19] I Agapov, M Benedikt, A Blondel, M Boscolo, O Brunner, M Chamizo Llatas, T Charles, D Denisov, W Fischer, E Gianfelice-Wendt, et al. Future circular lepton collider fcc-ee: Overview and status. *arXiv preprint arXiv:2203.08310*, 2022.

[20] M Harrison, T Ludlam, and S Ozaki. Rhic project overview. *Nuclear Instruments and Methods in Physics Research Section A: Accelerators, Spectrometers, Detectors and Associated Equipment*, 499(2-3):235–244, 2003.

[21] R Maier. Cooler synchrotron cosy—performance and perspectives. *Nuclear Instruments and Methods in Physics Research Section A: Accelerators, Spectrometers, Detectors and Associated Equipment*, 390(1-2):1–8, 1997.

[22] S Surzhikov and J Shang. Normal glow discharge in axial magnetic field. *Plasma Sources Science and Technology*, 23(5):054017, 2014.

[23] Theodoros Argyropoulos, Nuria Catalan-Lasheras, Alexej Grudiev, Gerard Mcmonagle, Enrique Rodriguez-Castro, Igor Syrachev, Rolf Wegner, Ben Woolley, Walter Wuensch, Hao Zha, et al. Design, fabrication, and high-gradient testing of an x-band, traveling-wave accelerating structure milled from copper halves. *Physical Review Accelerators and Beams*, 21(6):061001, 2018.

[24] Massimo Dal Forno, Valery Dolgashev, Gordon Bowden, Christine Clarke, Mark Hogan, Doug McCormick, Alexander Novokhatski, Bruno Spataro, Stephen Weathersby, and Sami G. Tantawi. rf breakdown tests of mm-wave metallic accelerating structures. *Phys. Rev. Accel. Beams*, 19:011301, Jan 2016.

[25] AD Cahill, JB Rosenzweig, Valery A Dolgashev, Sami G Tantawi, and Stephen Weathersby. High gradient experiments with x-band cryogenic copper accelerating cavities. *Physical Review Accelerators and Beams*, 21(10):102002, 2018.

[26] A Abada, M Abbrescia, SS AbdusSalam, I Abdyukhanov, J Abelleira Fernandez, A Abramov, M Aburaia, AO Acar, PR Adzic, P Agrawal, et al. Fcc-hh: The hadron collider-future circular collider conceptual design report volume 3 p. 755. *European Physical Journal-Special Topics*, 228(4), 2019.

[27] Shinichiro Michizono. The international linear collider. *Nature Reviews Physics*, 1(4):244–245, 2019.

[28] Steinar Stapnes. The compact linear collider. *Nature Reviews Physics*, 1(4):235–237, 2019.

[29] Tetsuo Abe, Tatsuya Kageyama, Hiroshi Sakai, Yasunao Takeuchi, and Kazuo Yoshino. Breakdown study based on direct in situ observation of inner surfaces of an rf accelerating cavity during a high-gradient test. *Physical Review Accelerators and Beams*, 19(10):102001, 2016.

[30] Xiaowei Wu, Jiaru Shi, Huaibi Chen, Jiahang Shao, Tetsuo Abe, Toshiyasu Higo, Shuji Matsumoto, and Walter Wuensch. High-gradient breakdown studies of an x-band compact linear collider prototype structure. *Phys. Rev. Accel. Beams*, 20:052001, May 2017.

[31] CGR Geddes, Cs Toth, J Van Tilborg, E Esarey, CB Schroeder, D Bruhwiler, C Nieter, J Cary, and WP Leemans. High-quality electron beams from a laser wakefield accelerator using plasma-channel guiding. *Nature*, 431(7008):538–541, 2004.

[32] Wim P Leemans, Bob Nagler, Anthony J Gonsalves, Cs Tóth, Kei Nakamura, Cameron GR Geddes, ESCB Esarey, CB Schroeder, and SM Hooker. Gev electron beams from a centimetre-scale accelerator. *Nature physics*, 2(10):696–699, 2006.

[33] Jérôme Faure, Clément Rechatin, A Norlin, Agustin Lifschitz, Y Glinec, and Victor Malka. Controlled injection and acceleration of electrons in plasma wakefields by colliding laser pulses. *Nature*, 444(7120):737–739, 2006.

[34] W Lu, C Huang, MM Zhou, WB Mori, and T Katsouleas. Limits of linear plasma wakefield theory for electron or positron beams. *Physics of plasmas*, 12(6):063101, 2005.

[35] I. Blumenfeld, C. E. Clayton, F. J. Decker, M. J. Hogan, C. Huang, R. Ischebeck, R. H. Iverson, C. Joshi, T. Katsouleas, N. Kirby, W. Lu, K. A. Marsh, W. B. Mori, P. Muggli, E. Oz, R. H. Siemann, D. R. Walz, and M. Zhou. Scaling of the longitudinal electric field and transformer ratio in a nonlinear plasma wakefield accelerator. *Phys. Rev. ST Accel. Beams*, 13:111301, Nov 2010.

[36] W. Lu, C. Huang, M. Zhou, W. B. Mori, and T. Katsouleas. Nonlinear theory for relativistic plasma wakefields in the blowout regime. *Phys. Rev. Lett.*, 96:165002, Apr 2006.

[37] JB Rosenzweig, G Andonian, M Ferrario, P Muggli, O Williams, V Yakimenko, and K Xuan. Plasma wakefields in the quasi-nonlinear regime. In *AIP Conference Proceedings*, volume 1299, pages 500–504. American Institute of Physics, 2010.

[38] R Pompili, MP Anania, E Chiadroni, A Cianchi, M Ferrario, V Lollo, A Notargiacomo, L Picardi, C Ronsivalle, JB Rosenzweig, et al. Compact and tunable focusing device for plasma wakefield acceleration. *Review of Scientific Instruments*, 89(3):033302, 2018.

[39] Kimberley Nichols, Bruce Carlsten, and Edl Schamiloglu. Analysis of quadrupole focusing lattices for electron beam transport in traveling-wave tubes. *IEEE Transactions on Electron Devices*, 61(6):1865–1870, 2014.

[40] S. Becker, M. Bussmann, S. Raith, M. Fuchs, R. Weingartner, P. Kunz, W. Lauth, U. Schramm, M. El Ghazaly, F. Grüner, H. Backe, and D. Habs. Characterization and tuning of ultrahigh gradient permanent magnet quadrupoles. *Phys. Rev. ST Accel. Beams*, 12:102801, Oct 2009.

[41] The CLIC, TK Charles, PJ Giansiracusa, TG Lucas, RP Rassool, M Volpi, C Balazs, K Afanaciev, V Makarenko, A Patapenka, et al. The compact linear collider (clic)-2018 summary report. *arXiv preprint arXiv:1812.06018*, 2018.

[42] J. K. Lim, P. Frigola, G. Travish, J. B. Rosenzweig, S. G. Anderson, W. J. Brown, J. S. Jacob, C. L. Robbins, and A. M. Tremaine. Adjustable, short focal length permanent-magnet quadrupole based electron beam final focus system. *Phys. Rev. ST Accel. Beams*, 8:072401, Jul 2005.

[43] J Van Tilborg, Sven Steinke, CGR Geddes, NH Matlis, BH Shaw, AJ Gonsalves, JV Huijts, Kei Nakamura, Joost Daniels, CB Schroeder, et al. Active plasma lensing for relativistic laser-plasma-accelerated electron beams. *Physical review letters*, 115(18):184802, 2015.

[44] A Marocchino, MP Anania, M Bellaveglia, A Biagioni, S Bini, F Bisesto, E Brentegani, E Chiadroni, A Cianchi, M Croia, et al. Experimental characterization of the effects induced by passive plasma lens on high brightness electron bunches. *Applied Physics Letters*, 111(18):184101, 2017.

[45] Steven M Lund and Klaus Halbach. Iron-free permanent magnet systems for charged particle beam optics. *Fusion engineering and design*, 32:401–415, 1996.

[46] Anna Lauria, Pasquale Arpaia, Marco Buzio, Antonio Gilardi, Marco Parvis, Mariano Pentella, Lucia Sabbatini, Enzo Simoni, and Alessandro Vannozzi. Rotating-coil measurement system for small-bore-diameter magnet characterization. *Sensors*, 22(21):8359, 2022.

[47] METROLAB Instruments SA. Pt 2025 nmr teslameter, probes type 1062.

[48] David Tong. Lectures on the quantum hall effect, 2016.

[49] Ying-Shun Zhu, Mei Yang, Zhuo Zhang, Wan Chen, Bao-Gui Yin, Cai-Tu Shi, and Wen Kang. Design and end chamfer simulation of pefp beam line curved dipole magnets. *Chinese Physics C*, 35(7):684, 2011.

[50] Erina Hirose, Kaguhiro H Tanaka, Toshihiro Takahashi, Yutaka Sato, Keigo Agari, Masaharu Ieiri, Yohji Kato, Michifumi Minakawa, Hiroyuki Noumi, Y Suzuki, et al. A new 3-axis magnetic field measurement system based on hall elements. *IEEE transactions on applied superconductivity*, 14(2):1814–1817, 2004.

[51] T Ishikawa, H Fujimura, R Hashimoto, T Ishida, J Kasagi, T Kinoshita, S Kuwasaki, F Miyahara, A Miyamoto, K Mochizuki, et al. The second gev tagged photon beamline at elph. *Nuclear Instruments and Methods in Physics Research Section A: Accelerators, Spectrometers, Detectors and Associated Equipment*, 622(1):1–10, 2010.

[52] David Collomb, Penglei Li, and Simon Bending. Frontiers of graphene-based hall-effect sensors. *Journal of Physics: Condensed Matter*, 33(24):243002, 2021.

[53] Khalil R Rostami and Ivan P Nikitin. High-sensitivity two-stage hall magnetometer with enhanced linearity and spatial resolution. *Measurement*, 153:107423, 2020.

[54] Dino Zangrando and Richard P Walker. A stretched wire system for accurate integrated magnetic field measurements in insertion devices. *Nuclear Instruments and Methods in Physics Research Section A: Accelerators, Spectrometers, Detectors and Associated Equipment*, 376(2):275–282, 1996.

[55] Wang Hongfei, Zhang Jidong, and Zhou Qiaogen. A stretch-wire system for accurate integrated magnetic field measurements in undulators. *Nuclear Techniques*, 32, 2009.

[56] Carlo Petrone. *Wire methods for measuring field harmonics, gradients and magnetic axes in accelerator magnets*. PhD thesis, Sannio U., 2013.

[57] P. Arpaia, A. Masi, and G. Spiezia. Digital Integrator for Fast Accurate Measurement of Magnetic Flux by Rotating Coils. *IEEE Trans. Instrum. Meas.*, 56:216–220. 6 p, Aug 2007.

[58] Louis Walckiers. Magnetic measurement with coils and wires. *arXiv: Accelerator Physics*, 2011.

[59] P Arpaia, M Buzio, J Garcia Perez, C Petrone, S Russenschuck, and L Walckiers. Measuring field multipoles in accelerator magnets with small-apertures by an oscillating wire moved on a circular trajectory. *Journal of Instrumentation*, 7(05):P05003, 2012.

[60] G Golluccio, A Beaumont, M Buzio, O Dunkel, M Stockner, and T Zickler. Pcb coil array for measuring curved accelerator dipoles: two case studies on the medaustron accelerator. *proceedings of IMEKO 2014*, 2014.

[61] Marco Buzio, Peter Galbraith, Juan Garcia Perez, Emanuele Laface, and Stefano Pauletta. A device to measure magnetic and mechanical axis of superconducting magnets for the large hadron collider at cern. In *2006 IEEE Instrumentation and Measurement Technology Conference Proceedings*, pages 759–764. IEEE, 2006.

[62] J. Garcia Perez, J. Billan, M. Buzio, P. Galbraith, D. Giloteaux, and V. Remondino. Performance of the room temperature systems for magnetic field measurements of the LHC superconducting magnets. *IEEE Trans. Appl. Supercond.*, 16(2):269–272, 2006.

[63] N. Smirnov, L. Bottura, F. Chiusano, O. Dunkel, P. Legrand, S. Schloss, P. Schnizer, and P. Sievers. A system for series magnetic measurements of the lhc main quadrupoles. *IEEE Transactions on Applied Superconductivity*, 12(1):1688–1692, 2002.

[64] Warren C Young, Richard G Budynas, and Ali M Sadegh. *Roark's formulas for stress and strain; 8th ed.* McGraw Hill, New York, NY, 2012.

[65] Stefano Sorti, Carlo Petrone, Stephan Russenschuck, and Francesco Braghin. A magneto-mechanical model for rotating-coil magnetometers. *Nuclear Instruments and Methods in Physics Research Section A: Accelerators, Spectrometers, Detectors and Associated Equipment*, 2020.

[66] Hans Braun, Marco Buzio, Roland Deckardt, Olaf Dunkel, Roland Felder, Lucio Fiscarelli, Romain Ganter, Samira Kasaei, Florian Löhl, Stephane Sanfilippo, Giordana Severino, Vjeran Vrankovic, and Louis Walckiers. Small-Diameter Rotating Coils For Field Quality Measurements in Quadrupole Magnets. 2016.

[67] P Arpaia, M Buzio, R De Oliveira, J DiMarco, and G Severino. A high-precision miniaturized rotating coil transducer for magnetic measurements. A high-precision miniaturized rotating coil transducer for magnetic measurements. *Sens. Actuators A*, 274:37–49. 13 p, 2018.

[68] Piotr Rogacki, Lucio Fiscarelli, Stephan Russenschuck, and Kay Hameyer. Development of a rotating-coil scanner for superconducting accelerator magnets. *J. Sensors Sensor Syst.*, 9:99–107. 9 p, 2020.

[69] Pasquale Arpaia, Gianni Caiafa, and Stephan Russenschuck. A rotating-coil magnetometer for scanning transversal field harmonics in accelerator magnets. *Scientific reports*, 9(1):1–11, 2019.

[70] Stephan Russenschuck. *Field computation for accelerator magnets: analytical and numerical methods for electromagnetic design and optimization.* Wiley, Weinheim, 2010.

[71] L. Fiscarelli et al. Magnetic Measurements and Analysis of the First 11-T Nb3Sn Dipole Models Developed at CERN for HL-LHC. *IEEE Trans. Appl. Supercond.*, 26(4), 2016.

[72] Olivier Contel, Paul Leroy, Alain Roux, Christophe Coillot, Dominique Alison, A. Bouabdellah, Laurent Mirioni, L. Meslier, A. Galic, Marie-Cecile Vassal, Roy Torbert, J. Needell, Don Rau, Ivan Dors, R. Ergun, James Westfall, D. Summers, J. Wallace, Werner Magnes, and B. Porte. The search-coil magnetometer for mms. *Space Science Reviews*, 199:1–26, 09 2014.

[73] Slawomir Tumanski. Induction coil sensors—a review. *Measurement Science and Technology*, 18(3):R31–R46, jan 2007.

[74] M. Buzio. Fabrication and calibration of search coils, 2011.

[75] Karolina Kokurewicz, Enrico Brunetti, Alessandro Curcio, Davide Gamba, Luca Garolfi, Antonio Gilardi, Eugenio Senes, Kyrre Ness Sjobak, Wilfrid Farabolini, Roberto Corsini, et al. An experimental study of focused very high energy electron beams for radiotherapy. *Communications Physics*, 4(1):1–7, 2021.

[76] Daniela Poppinga, Rafael Kranzer, Wilfrid Farabolini, Antonio Gilardi, Roberto Corsini, Vanessa Wyrwoll, Hui Khee Looe, Björn Delfs, Lukas Gabrisch, and Björn Poppe. Vhee beam dosimetry at cern linear electron accelerator for research under ultra-high dose rate conditions. *Biomedical Physics & Engineering Express*, 7(1):015012, 2020.

[77] Francesco Romano, Anna Subiel, M McManus, ND Lee, Hugo Palmans, R Thomas, Sean McCallum, Giuliana Milluzzo, Marco Borghesi, Aodhan McIlvenny, et al. Challenges in dosimetry of particle beams with ultra-high pulse dose rates. In *Journal of Physics: Conference Series*, volume 1662, page 012028. IOP Publishing, 2020.

[78] Pasquale Arpaia, Roberto Corsini, Antonio Gilardi, Andrea Mostacci, Luca Sabato, and Kyrre N Sjobak. Enhancing particle bunch-length measurements based on radio frequency deflector by the use of focusing elements. *Scientific RepoRtS*, 10(1):1–12, 2020.

[79] L. Deniau. Coils calibration correction factor for rectangular windings, mta-in-98-026, 2011.

[80] L Bottura, M Buzio, P Schnizer, and N Smirnov. A tool for simulating rotating coil magnetometers. *IEEE transactions on applied superconductivity*, 12(1):1680–1683, 2002.

[81] Piotr Rogacki. *A contribution to the development and characterization of rotating-coil magnetometers*. Shaker Verlag, 2022.

[82] National Instruments. *NI 6366 X Series Data Acquisition 2 MS/s/ch, 8 AI, 24 DIO, 2 AO Device Specifications*, 2016.

[83] Maxon. *EC 45 flat with integrated electronics Operating Manual*, 2020.

[84] Baumer. *Incremental encoder OptoPulse EIL580P-T Datasheet*, 2020.

[85] Pasquale Arpaia, Marco Buzio, Vincenzo Di Capua, Sabrina Grassini, Marco Parvis, and Mariano Pentella. Drift-free integration in inductive magnetic field measurements achieved by kalman filtering. *Sensors*, 22(1):182, 2021.